

Design and Stiffness Analysis of a 5-axis Gantry-Tau Milling Machine

Jan Fredrik Røsjordet

Supervisor

Geir Hovland

Torgny Brogårdh

This master's thesis is carried out as a part of the education at the University of Agder and is therefore approved as a part of this education. However, this does not imply that the University answers for the methods that are used or the conclusions that are drawn.

University of Agder, 2018
Faculty of Engineering and Science
Department of Engineering Sciences

Abstract

The Gantry-Tau is a Parallel Kinematic Machine (PKM) structure that possesses many advantages as a milling machine, where it has a low moving mass, high stiffness and a large workspace to footprint ratio. This thesis presents a new milling machine design based on this structure, as a continuation of a formerly constructed prototype, see [1]. This includes selection of new actuators for the linear drives as well as the development of a new tool platform and two joint concepts. A short workspace analysis is presented on the proposed design, which includes calculation of valid workspace and an analysis on the required joint mobility with "optimal" joint mounting positions. The machine stiffness in the entire workspace, with only links considered, is presented and stiffness including the tool platform and gantry carriages is presented at five positions. A short analysis on machine stiffness with 5-axis motion with tool rotation up to 25 degrees is also presented.

The proposed design of the machine is capable of reaching the demands of the milling application, where it can handle feed forces above 1000N and move at linear speeds above 0.5m/s and rotational speeds above 1.5rad/s.

Simulations showed that the two joint concepts, a ball joint and Cardan joint design, have stiffness in excess of 144 N/ μ m and 152 N/ μ m, at a weight of 2.1kg and 3.5kg. With these, the obtained workplace stiffness is above 3.16N/ μ m, 4.42N/ μ m and 4.05 N/ μ m in x,y and z-direction with 3-axis motion and only considering link stiffness, which is >255% of the old design.

The new platform design increased the lowest recorded stiffness from 0.49N/ μ m to 83N/ μ m, with a weight increase from 6.5kg to 16.6kg. Including tool platform and gantry drives, the workspace stiffness is reduced by 11-21% within the 5-axis workspace.

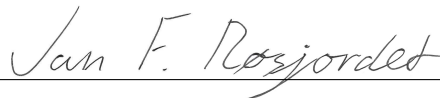
The design was modelled with the use of *SolidWorks* (CAD software), and the stiffness was evaluated with *Abaqus* (FEM software). Kinematics and machine stiffness calculations were performed with *Matlab*.

Acknowledgement

This project marks an end to the master's programme in Mechatronics at the University of Agder. It has been a valuable experience where a great deal of knowledge has been obtained from a vast number of topics, all thanks to knowledgeable teachers. For that, the author would like to thank the university for the opportunity to take the degree.

The author would like to thank both supervisors, Geir Hovland and Torgny Brogårdh for their invaluable help and guidance with the project. The author would also like to thank Jan Henriksen for his much-appreciated help with the FEM simulations.

GRIMSTAD, MAY 25, 2018



Jan Fredrik Røsjordet

Contents

Abstract	i
Acknowledgement	ii
Contents	vi
Introduction	2
1 Literature Study	3
1.1 Applications	3
1.1.1 Milling	3
1.1.2 Friction Welding	4
1.1.3 Drilling and Riveting	5
1.1.4 Pick and Place	5
1.2 Linear Actuator	5
1.2.1 Screw Actuator	6
1.2.2 Linear Motor	8
1.2.3 Rack and Pinion	9
1.2.4 Belt Drive	10
1.3 Joint	11
1.3.1 Spherical Joint	11
1.3.2 Cardan Joint	13
1.4 Bearing	14
1.4.1 Needle Bearing	14
1.4.2 Plain Bearing	15
1.4.3 Spherical Plain Bearings	15

1.5	Linear Bearing	16
1.5.1	Rolling Element Bearing	16
1.5.2	Plain Bearing	16
2	Kinematics	17
2.1	Kinematic Parameters	17
2.2	Numeric 5-axis Inverse Kinematics	18
2.3	Inverse Robot Jacobian	20
2.4	Workspace Analysis	20
2.5	Joint Rotation	22
3	Joint Design	25
3.1	Material	25
3.2	Bearing Stiffness	26
3.2.1	Plain Bearing	26
3.2.2	Spherical Plain Bearing	28
3.2.3	Needle and Roller Bearing	29
3.2.4	Application Example	30
3.3	Ball Joint	32
3.3.1	Link Adapter	33
3.3.2	Joint Cap	33
3.4	Cardan Joint	34
3.4.1	Link Adapter	35
4	Joint Stiffness	36
4.1	Ball Joint	36
4.1.1	Link Adapter	37
4.1.2	Joint With Rotation	38
4.1.3	Compression Stiffness	39
4.1.4	Ball Polymer Liner	40

4.2	Cardan Joint	41
5	Machine Design	43
5.1	Actuator Requirements	44
5.1.1	TCP Forces	44
5.1.2	TCP Speeds	46
5.1.3	TCP to Actuator Force	46
5.1.4	TCP to Actuator Speed	48
5.1.5	Summary	49
5.2	Link Actuator	49
5.2.1	Stiffness	50
5.2.2	Speed	51
5.2.3	Force	51
5.2.4	Summary	52
5.3	Gantry actuator	53
5.3.1	Backlash	54
5.3.2	Stiffness	54
5.3.3	Speed	55
5.3.4	Force and Acceleration	55
5.3.5	Natural Frequency	56
5.3.6	Summary	57
5.4	Gantry Carriage	58
5.5	Passive Link	59
5.6	Tool Platform	60
5.6.1	Spindle	61
6	Machine Stiffness	63
6.1	Only Considering Link Stiffness	63
6.2	Tool Platform	66

6.3 Gantry Carriage	67
6.4 Platform, Carriage and Link	68
6.5 5-Axis	69
7 Discussion	70
8 Conclusion	75
Bibliography	77
List of Figures	83
List of Tables	85
Appendices	86
A Inverse Robot Jacobian	87
B PKM Machining Centres	90
C Ball Joint Dimensions	92
D Cardan Joint Dimensions	96
E Tool Platform Dimensions	100

Introduction

The Gantry-Tau is a Parallel Kinematic Machine (PKM) invented at ABB Robotics along with other members of the Tau family of robots, see [2]. The Tau family is characterised by their leg clusters of three, two and one, where the Gantry-Tau is the linear version. It has 3 degrees of freedom (d.o.f) as a PKM, but with the addition of two telescopic links within the two clusters of three and two, rotation of the tool is possible, which makes the robot suitable for 5-axis machining. The first prototype of the robot was built at the University of Queensland and was followed by the construction of the prototype currently situated at the University of Agder (UIA), see [1].

Problem Description

The current prototype did not reach the desired workspace stiffness. The leading cause of this was identified to be the low stiffness of the links, primarily determined by the joints. The stiffness of the machine was also further reduced by the compliance of the platform. The robot also uses ball screw actuators on both the telescopic links and the gantry carriages, which are characterised by a low rigidity and poor expandability.

Objective

The goal of the project is to improve the current design of the Gantry-Tau robot situated at UIA, see Figure 1. The main focus is to improve the stiffness of the this, such that it is applicable to 5-axis machining. It is intended for low volume and medium quality prototyping of steel and aluminium parts, where accuracy of $100\mu m$, or better, is required. To achieve this, it is desirable to reach a stiffness of $> 10N/\mu m$ in the usable workspace.

A state of the art study is then to be performed such as to find new linear actuators for the robot. Through state of the art study and a design process, new joints for the robot is to be proposed. A new tool platform is also to be designed, as the old design is inadequate. A high stiffness is desirable, but the components must also not limit the dynamic performance of the machine. Selected actuators must also be able to reach the speed and force requirement of the milling application.

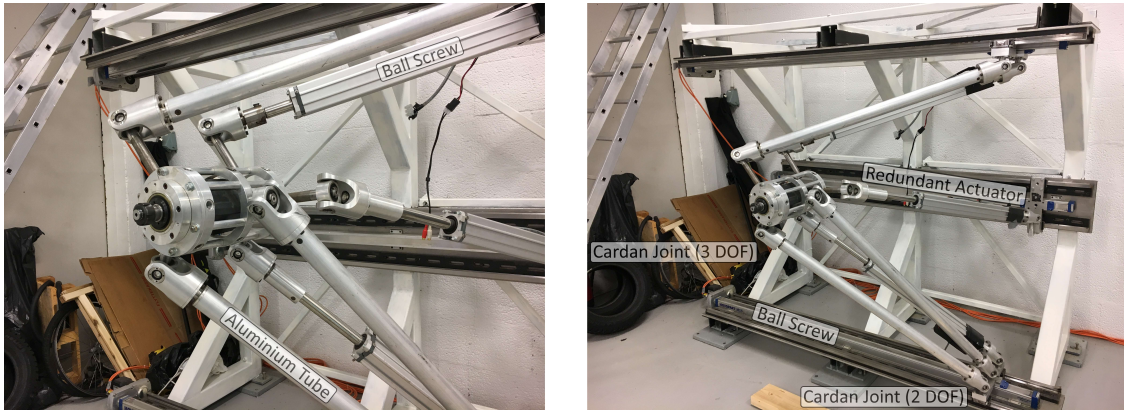


Figure 1: Current prototype situated at UiA

Limitations

While PKM's have many advantages over Serial Kinematic Machines (SKM), most often these are not as versatile. Because of its many possible configuration, the design of a PKM therefore more often involves more steps and iterations. The general design optimisation process of a PKM is described well in [2], where it is divided into the four following steps.

1. Analyze the application requirements and select the optimal concepts with respect to kinematic requirements.
2. Optimize the parallel kinematic structures to find a globally optimal structure.
3. Optimize the rigid body performance.
4. Optimize the elasticity performance.

Points 1. and 2. are not considered in this thesis, as multiple papers of the Gantry-Tau structure has been made on the subject such as [3] and [4]. Point 3 is considered in the design process, but no extensive analysis is made on the subject. This thesis is therefore limited to the last point, where the current robot configuration is treated as optimal, and a structural design of the robot is proposed with the primary focus on elasticity performance.

Chapter Outline

The first chapter of this thesis presents the literature study performed on state of the art components that was relevant to the robot. Other possible applications for the robot and the requirements it poses is also presented. The second chapter presents the kinematics where the calculated workspace is shown. Here it is also investigated the mobility requirements that the robot poses on the joints. The third and fourth chapter then presents the two joints that were developed for the robot, where the calculated stiffness of is presented. The fifth chapter presents the design of the robot as a milling machine, which involves the design of a new tool platform and selection of actuators. The sixth and final chapter then presents the workspace stiffness that was achieved with the proposed design.

1 Literature Study

Presented in this chapter is the literature study that was conducted on other possible applications and state of the art components relevant to the construction of the robot. The primary focus of the robot is the milling process, but other potential applications are also presented in this chapter. Different solutions for the linear actuators in both the telescopic links and the carriage are then presented. In relation to the joint design presented in Chapter 3, various joints and bearing types are presented along with their strengths and weaknesses. Lastly, different types of linear bearing types which can be used for guiding the gantry carriages are presented.

As a part of the literature study, other other existing and discontinued PKM machining centres was also studied to get a better understanding of the performances that a PKM structure can bring to the field. It is not shown in this chapter, but is attached to Appendix B.

1.1 Applications

First presented in this section is the milling application, as it is the main focus of this thesis. However, the Gantry-Tau structure can suite other applications such as friction stir welding (FSW), drilling and riveting, as well as pick and place applications, of which much of the study presented in this chapter also applies to. Also presented is, therefore, a short description of these applications and the characteristics of the requirements that such an application would pose.

1.1.1 Milling

Milling is the process of removing material with the use of a rotating cutter, powered by an electric motor known as the spindle. This spindle must be supported and guided through the workpiece at a predefined path with as little deviation as possible, such that the cut is as accurate as possible. Forces are inflicted on the tool from the forces that are required by the cutting edge of the tool to shear the material. This shear force relates to the strength of the material commonly described by a parameter known as the specific cutting force. The magnitude of the path deviation due to these disturbance forces relates to the stiffness of the machine of which supports the spindle and the fixture that holds the workpiece. For such a milling machine to have the highest possible accuracy, is therefore desirable to have the highest possible stiffness.

Since the disturbance force ceases when the cutting edge of the tool shears the material, it is not a constant force where it varies with the instantaneous angle of the tool. This disturbance force will, therefore, excite the machine with the frequency of which the cutter hits the material. The machine must therefore not only be stiff but have a high enough mechanical bandwidth, such that it can maintain high material removal rates without causing problems like regenerative and modal chattering.

Different materials also require different cutting speeds, which mostly relates to the surface finish of the finished cut, but also affects the cutting force. The cutting speed is commonly referred to as "speeds" and the linear speed at which the tool moves in reference to the workpiece is referred to as "feed speed". These parameters are related by the linear feed distance for each instance of cutting action, referred to as "feed pr. tooth", and the rotational speed of which the spindle rotates.

With the advancement of high-performance machines, higher cutting speeds have been made possible, where the process is commonly known as High Speed Machining (HSM). This method is dictated by multiple low depth cuts, with cutting speeds 5-10 times higher than with regular machining. HSM methods also typically introduce smaller forces on the cutting tool, where the cutting forces reduce with increased cutting speeds (if power is kept constant). By increasing the cutting speed, the feed speed requirement also increases, as the tool requires a minimum feed pr. tooth. To reach these high cutting speeds with small diameter tools, high speed requirements are also posed on the spindles. It is then proposed in, [5], that for a HSM capable machine, it is recommended to have spindle speeds ≤ 40000 rpm, spindle power > 22 kW, feed rate 40-60 m/min and transverse speeds < 90 m/min.

It is seen here, that units with machining applications are typically given in units such as m/min and mm/min . In this thesis, these are used in occasions where values are initially given by these units from their sources, or where it is used to compare values from such a source. However, all calculations in this report are based on SI units if not otherwise specified. Common terms in machining applications are feeds and speeds, which is also used throughout this thesis. The feed speed of the tool is the linear speed that the tool moves along the workpiece and speeds refer to the speed at which the tool cuts the material. These parameters are determined by the operator of the machine, based on different factors such as workpiece material, end mill size, work type and more.

1.1.2 Friction Welding

Friction welding is the technique of joining two materials through the excitement of the material with friction. There are three types of friction welding techniques, which is Linear Friction Welding (LFW), Rotary Friction Welding (RFW) and Friction Stir Welding (FSW).

Friction Stir Welding (FSW) differs from the other techniques in that it introduces a third interface, the tool, which must be guided by a robot along the edges of the two parts of the workpiece.[6]. To do this, the robot must exert large forces on the tool, where axial forces, or thrust forces, are dominant. The magnitude of this force depends on the material being welded, but an example of the loads are presented in [7]. For 6061 Aluminium, the tool forces are expected to be 12.5kN downwards (axial/thrust), 1.33kN along the weld direction (direction of movement) and 135N in a transverse direction to the weld direction.

Accuracy requirements with friction stir welding are not as high as with milling since the accuracy of the joining is mostly determined by the fixture that temporarily holds the two parts together. The TCP is therefore allowed to deviate up to 1 mm along the surface of the workpiece. Deviation perpendicular to the workpiece does not have any particular requirements. While accuracy requirement is not significant, the tool is subjected to large forces, and the machine, therefore, has to be very stiff to meet these requirements. As this process is generally characterised as slow, the rigidity of the components is more critical than their weight.

1.1.3 Drilling and Riveting

Another application of the robot, is drilling and riveting of an aeroplane, helicopter or rocket fuselage. The workload in this application is largely dominated by the axial force along the drill direction also referred to as the thrust force. As with machining in general, both the tool and material largely determine this load.

The accuracy required by this application is mainly with the positioning of the drill bit in reference to the surface of the workpiece. It is also desirable for the robot to be lightweight, such that it can move quickly between different drilling and riveting applications to minimise cycle time.

1.1.4 Pick and Place

Packaging products on a production line is a very repetitive task which can be efficiently automated with robots. The main goal of this application is to reduce production time, which creates a constant desire for faster and more efficient robots. It is mentioned in [8], that the speed of the robot is often limited by the heating of the motors, which is especially apparent for serial robots with high inertia. Therefore, the low inertia PKM robots have many advantages over other robot structures in this field.

For fast moving small load pick and place robots, it is generally only required to have 3 or 4 d.o.f, where with 4 d.o.f it is desirable to have a continuous rotation of the head. This makes PKM's such as the Delta structure, invented by Raymond Clavel in 1990, suitable, where robots such as the *Flexpicker* from *ABB* have been widely adopted to numerous packaging lines. In large load pick and place applications, such as packing products on pallets, serial robots are still attractive. This is due to their large versatility and large reachable workspace compared to their footprint, as well as the low accuracy requirement of the process.

1.2 Linear Actuator

All the actuators of the Gantry-Tau structure are linear motion actuators. The primary actuators are gantry based actuators, which is dictated by long stroke lengths that should be expandable without compromising its performance. With the 5-axis structure used in this thesis, two telescopic links are also needed. These dictate rotation of the tool and are therefore less affected by scaling of the machine. Both telescopic link actuators and the gantry-based actuators are presented in this section since some of the principles apply to both.

1.2.1 Screw Actuator

Screw actuators have seen use in many applications in both Cartesian stacked axis CNCs as well as parallel robots, and is generally conceived as the most common solution in high accuracy applications. Presented in this section are three screw actuator principles, which is the lead nut, ball screw, and roller screw.

Lead Nut: The lead nut, also referred to as the acme screw, is just a simple nut which is threaded with the opposite thread of the rod, which then creates linear motion in the same manner that a regular screw and nut does. Since this method relies on the sliding action, high friction forces occur, and the technique is associated with high mechanical losses with efficiency below 50% [9]. Lead nut actuators are therefore often not capable of running at full duty cycles, and are typically limited to 60% duty cycle.

A common nut material is brass, which, together with the high contact area, obtains a high degree of stiffness. However, the accuracy of this is limited because of backlash between the threads, which depend on the accuracy of manufacturing. This can be eliminated by using two nuts connected with a preload spring, such that the threads are under a constant load. However, this increases friction forces within the drive nut, which decreases the already low efficiency.

With the use of polymer nuts, this friction can be reduced. These are also more compliant than the conventional brass nut and can therefore allow for a tighter fit, without the risk of seizing with the screw. However, by the same principle, these are not as stiff.

Ball Screw: The ball screw, is the most common method for linear screw actuators in high precision applications. It has seen extensive use in both commercial CNCs and parallel robots, where it is also used on all axes of the current prototype.

The ball screw assembly consists of a housing with a groove that has an equal helix as the screw. In between the grooves of these, ball elements are situated, where these retain axial motion in the same way that a deep groove ball bearing does. Because of the helical thread, axial motion is generated when these two rotate in the opposite direction. When the balls reach the end of the nut, these are recirculated back to the opposite side of the nut in an external groove. Hence it is also referred to as a recirculating ball screw.

Since the interface consists of rolling elements, the friction forces are much lower than the solid nut. It is therefore common for these to have a high efficiency of 95% or better which means that these are capable of 100% duty cycles. However, as with regular ball bearings, the contact condition is defined as point contact, and the stiffness is therefore not as high as the solid nut. This contact condition is nonlinear, where the contact area increases with the load as the balls deform elastically. Therefore, by preloading the ball elements, the stiffness of the screw increases. Preload can also be used to eliminate backlash, like the solid nut, but the friction forces are in this case much less affected.

Roller Screw: The roller screw actuators are the latest technology in linear screw actuator design. This uses threaded/grooved rollers instead of balls which allow more contact points for a given length. There are two subtypes of this, which is the planetary roller screw and the recirculating roller screw.

The planetary roller screws has rollers that arranged around the screw like planets of a planetary gear. These can either be arranged around a screw with external threads but can also be used with internal threads which are referred to as inverted planetary rollers screw. While the inverted planetary screw takes up less space, it requires a screw with internal threads which is more difficult to form accurately. The axial forces are retained by the engaging threads of the screw and the rollers. The rollers are prevented from rotating by gears on the end which engage in a sun gear that synchronises the rotation of all the rollers.

Unlike planetary roller screws, the rollers in the recirculating roller screw are not threaded but circumferential grooved. To generate axial motion, the roller, therefore, moves axially within the nut instead. After one cycle, usually one rotation around the screw, one of the rollers are moved out of the thread and advanced with a distance equal to the lead of the screw. This technique allows for smaller leads, and therefore a high reduction ratio of the screw can be achieved. By the same principle, this also allows for more contact points for a given length of nut and thus a higher stiffness [10]. Because of the recirculating motion, this technique does not offer the same speed and acceleration capabilities as the planetary variant.

There are higher friction losses within roller screw assembly then ball screws, which means these only have an efficiency of up to 90% compared to the 98% of the ball screw. While the stiffness also increases with preload, the efficiency reduces to the point were 100% duty cycle might not be practical.

Summary: While the different screw interfaces poses various advantages and disadvantages, there are some that are common to them all. The most significant drawback is that the stiffness is heavily dependent on actuation length, where the stiffness of the screw is generally lower than the nut itself. The stiffness of the actuator also depends on the support of the screw, where to not interfere with the nut itself, the screw can only be supported at each end, or in some cases only one end. This also makes the stiffness of the screw nonlinear, where it depends on the position of the drive. For a double supported screw, the lowest stiffness is when the nut is in the middle of the screw, where it increases as it moves towards either of the ends. This can create a possible headache when designing a control system, depending on the severity of the stiffness fluctuation.

A limitation of the speed of the screw actuators is a phenomenon known as whipping, which is when the rotation of the screw self-excites its resonance modes. This problem drastically worsens for increased length of the screw where the maximum length is typically no more than 3m for dynamic applications [11]. One method of counteracting this is to rotate the nut instead of the screw, but this places the drive on the moving part instead, which increases the moving mass of the system.

1.2.2 Linear Motor

A linear motor is basically a conventional electric motor where the stator and rotor are cut open and rolled out. These are available in the three different configurations presented in Figure 1.1. One where the motor is "wrapped around" a rod, where the motor configuration resembles the typical linear screw actuator. The other two are flat and u-shaped motors, which require external support from linear bearings.

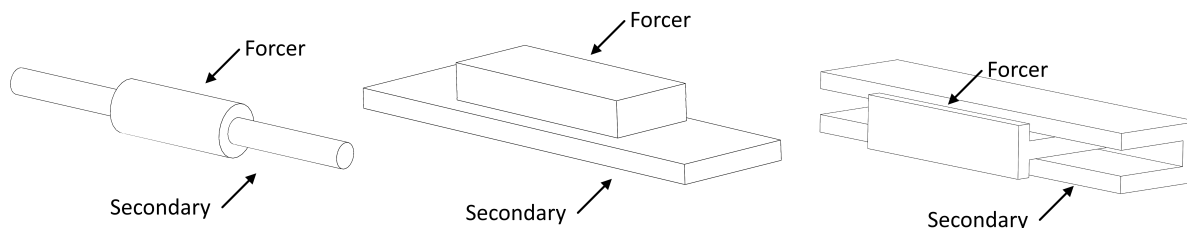


Figure 1.1: Linear motor configurations, rod style (L), Flat (M), U-channel (R)

There are some advantages of using a direct drive over other solutions, where there is no mechanical backlash and stiffness is independent of position. The stiffness of the drive also more or less only relies on the feedback control system, though with some limitations imposed by the motor. These also provide among the highest acceleration rates and velocities. There are no parts in contact between the rail and the motor, except for the support bearings, and there is therefore less mechanical losses and fewer requirements for maintenance.

However, linear motors are not as efficient as it's rotary counterpart. Mostly because of a practical reason, where the air gap between the primary and secondary part cannot be as small as for its rotary motors. Also, because of the open nature of the motor, the flux density is not evenly distributed between the coil (forcer) and the secondary part, which reduces thrust forces at higher speeds [12].

The most common linear motor used for linear drives are synchronous motors, which rely on the secondary part containing magnets. With magnets in the rails, the cost of the rail is high, since strong permanent magnets are expensive. The rail of the system therefore often end up costing more than the motor itself, depending on the length. With parallel gantries, multiple motors can also share the same rail working independently, reducing number of rails needed, or in tandem where a single motor is not adequate. To reduce the cost of the rails the linear induction motor can be used instead, which like it's rotary counterpart, does not require any expensive permanent magnets. Another benefit of the asynchronous induction motor, and its magnet-less secondary section, is that metal shavings are not as strongly attracted to the rails.

With synchronous motors, there are also two distinct types, which is ironcore motors and ironless motors. The ironless motor, as the name implies, contains no iron in the forcer where there is commonly only an epoxy resin that supports the coils. This reduces the weight of the forcer considerably, allowing for higher accelerations. However, the thermal properties of epoxy are close to 1/50th of steel and therefore the heat dissipation is reduced. The continuous force of these is therefore limited, where the peak to continuous force difference is generally high and usually a factor of 4 or higher. With iron core motors this factor is typically around 2.5 (with forced air cooling) [13]. It is also noted in [14] that the primary concern with linear motors is thermal related issues, and the addition of external cooling can go as far as to increase the continuous force by up to 50%. Linear motors, in general, do not offer as high feed forces as other solutions, as it is direct drive and cannot use the advantage of a reduction stage. High force applications then require larger motors with large cooling systems, which not only adds to the cost but also to the weight of the system.

Three factors mainly determine the stiffness of the linear motor [13]. The first is the mechanical stiffness of the mounting as well as the stiffness of the internal supporting material of the coils in the forcer. Ironless motors are therefore not as stiff, since the stiffness of epoxy resin is low compared to steel. Secondly, the resolution of the position sensor will affect the accuracy of the feedback and in turn the achievable closed loop stiffness of the drive. Lastly, also related to the control system, is the sampling rate and loop time of the control system which affect the dynamic stiffness at higher bandwidths.

Linear motors also generate strong attraction forces which pull the motor against the support bearings. Looking at the rated attraction force supplied in various catalogues, such as [15], this can be more than 10 times the rated continuous thrust force. This subjects the linear guideways to large forces which in turn introduces deflections of the rail and bearings. This can be avoided by mounting the motors in pairs, back to back, or by using u-channel motors.

1.2.3 Rack and Pinion

The rack and pinion system is no new invention, which have seen much use in low-end applications, but with the advancement of modern manufacturing and precision cut gears, this has seen its way into high precision applications. Rack and pinion systems do not offer the same high-speed characteristics as belt drives and linear motors, but with precision cut gears, it is seen that both high accelerations and high speeds are achievable. The main advantage of this drive type over linear motors is that it is capable of much higher feed forces since it can be equipped with a gear reducer. The rack and pinion system can also be extended practically endlessly, more or less only limited by the linear guideways. While high precision racks are not cheap, they are not as expensive as the secondary section of a linear motor. The stiffness is also independent of the position of the drive, unlike screw actuators and regular belt drives. The stiffness of a rack and pinion system depends on many components, where the most significant is the torsional and tilting rigidity of the gearbox. The effect of this also depends on the size of the pinion, where a smaller pinion gives higher stiffness and less backlash but also reduces the maximum speed of the drive. A closer look at this is shown in Section 5.3.

It is well known that the most significant drawback of a rack and pinion system is its backlash, which comes from the required clearance between the meshing teeth. This backlash can be reduced by using precision cut gears or eliminated altogether by using mechanical or electronically controlled preload. Three common methods of backlash elimination (reduction) are presented in Figure 1.2.

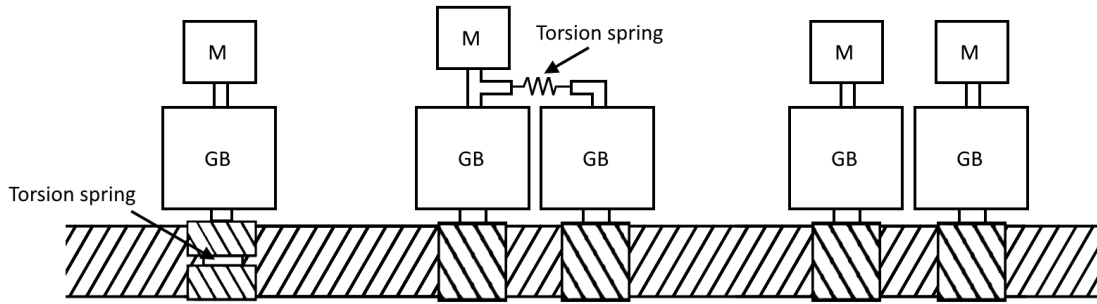


Figure 1.2: Rack and pinion backlash elimination, split pinion (L), torsion spring before gearbox (M), electronic preload (R)

Mechanical preload can take the form of a split pinion which is connected together with springs, such as, when the pinion is pressed into the rack, the two pinions are loaded oppositely. While this eliminates the rack and pinion backlash, the backlash of the gearbox is still present. Another method of mechanical preload is to use two gearboxes and pinions, where the same torsional spring method is used, but between the input of the two gearboxes. This also eliminates the backlash of the gearbox, but increases the weight of the drive system without any performance increase. The last method is electronic preload, where two complete pinion drive system is used. These are mounted to the same carriage, configured as a master and slave drive, where these push against each other and so backlash of the gearbox is also eliminated. This effectively doubles the weight of the system, but since the two drives are controlled independently, these can work in tandem which can reduce the required motor and gearbox size.

While the methods mentioned above can reduce or eliminate backlash, these can add significant cost to the system. While the split pinion only requires a single gearbox and motor, the split pinion itself is more expensive than a regular pinion. High-performance gearboxes are not cheap either, which makes the dual gearbox a costly solution. While the dual drive solution can use a smaller motor and gearbox than the above, it still requires two of both, which is more expensive than a single equivalent system.

Two gear types are commonly available with precision rack and pinion systems, which is helical gear (cross cut) and spur gear (straight cut). The helical gear has the advantage of smoother motion where these run quieter and with less vibrations. Spur gears do not give as smooth motion since the whole width of the tooth meshes simultaneously. Spur gears offer a small increase in mesh stiffness, but the main advantage is, for the most part, their simplicity and lower price. With the advance of modern manufacturing, this difference in price is however small in most cases.

1.2.4 Belt Drive

The standard belt drive actuators are generally characterised with low stiffness. Stiffness are also not independent of position and worsen with the length of the belt. A solution to this is presented in the patent [16], by Michael R. Everman. This uses a stationary belt mounted to the rail which meshes with another belt mounted to a drive on the carriage. With this, only a small part of the belt is under tension, and therefore stiffness of system is independent of the rail length. Since the belts are made of rubber, reinforced with steel or fibres, the stiffness of the drive is still limited. The advantage of this is the lower cost of the belt compared to the rack and pinion.

1.3 Joint

The Gantry-Tau structure is designed around the principle of links only subjected to axial forces. To achieve this, one of the joints on the link must have 3 d.o.f and the other at least 2 d.o.f. As these link assemblies then consist of two joints, these significantly affect the total link stiffness and are therefore a vital component of the machine. The joints discussed in the sections below are divided into spherical joints (3 d.o.f) and Cardan joints (2 d.o.f and 3 d.o.f).

1.3.1 Spherical Joint

The basic spherical joint is based on the kinematics of a sphere supported by an outer shell which prevents translation but does not restrict any rotation, see Figure 1.3. While it offers 360 degrees movement around one axis, the movement around the other two axes are limited by collision between the shaft connected to the ball and the housing. To the authors's knowledge, the largest mobility of these types of joints are with a cone angle of no more than 45 degrees, which is the carbon fibre joints of *Corbon* [17].

Spherical joints are commonly used with direct sliding contact since the surface contact condition yields a high degree of stiffness compared to the size of the joint. With sliding contact, these types of joints are generally characterised by high friction moments where stick-slip can be an issue. This can also pose some implications with the control system of the robot if hysteresis effects are present. Another derivation of the ball joint accounts for this by using rolling ball elements instead of the sliding interface. This is commonly known as spherical roller joints (SR-joints) and are, among others, available from *INA Schaeffler* [18] and *Hephaist* [19]. While this reduces friction, the stiffness of the joint is reduced as the contact is defined as point contact instead of surface contact. The two *INA* joint sizes have a stiffness of 280/400N/ μm and 350/700N/ μm in tension/compression at a weight of 2.3 kg and 4.5 kg. But, these are limited to 20 degrees mobility, with an optional 30-degree mobility, presumably with lower stiffness. The SR-joints of *Hephaist's* are limited to 30 degrees mobility. These are not free of backlash but are available with a reduced backlash of 1 μm [19].

Another spherical joint is the joint known as a rod end, which resembles the conventional ball joint, but where the ball is rotated 90 degrees and has a through-hole in it, see Figure 1.3. The central element of this joint then becomes what is known as a spherical plain bearing. In this configuration, the link pivot angle is no longer restricted by the same angle as the regular ball joints where the link can pivot 360 degrees along one of the axes instead of rotating. Commercial rod ends are typically restricted to 17 degrees or less of a pivot. However, with clearance free spherical plain bearings, this angle is generally less than 10 degrees. The mobility can be increased with the use of misalignment spacers, which essentially is an adapter that allows a smaller shaft to be used such that the ball can be rotated further without the shaft colliding with the raceway. This reduces the stiffness of the joint where the thinner shaft has lower bending stiffness and as well as the contact area of the spherical bearing reduces at larger angles.

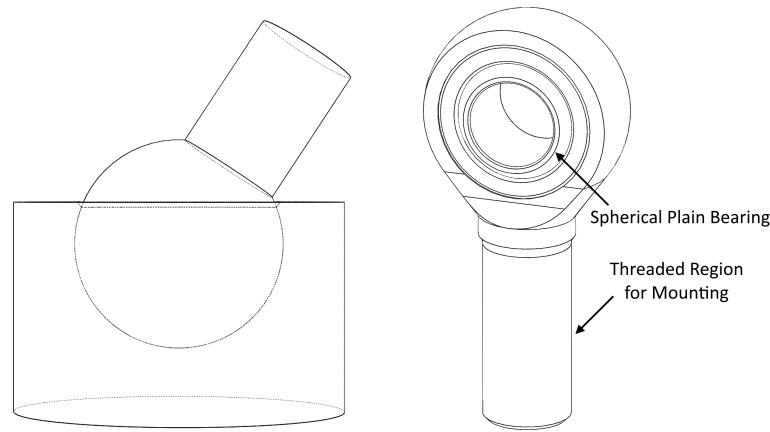


Figure 1.3: Ball joint (L), Rod end (R)

Another method to account for the reduced mobility of the ball joint is presented in [20]. Here, the ball joint is restricted along one axis, making it a 2 d.o.f ball joint. The ball can then rotate much further around this unrestricted axis since it is then less limited by the housing. The last d.o.f is then regained by mounting the housing to a bearing. No stiffness values were obtained with this, but it is presumed to not be high at larger pivot angles because of the single supported pin loading condition. Another design based on this principle is proposed by the author of this thesis, which is presented in section 3.3.

With spherical joints, the limiting factor on the mobility of the joint is how far the housing wraps around the ball. The amount that the housing wraps around the ball is a trade-off between the mobility and stiffness, as this is related to the tensile stiffness of the joint. If the ball were to be retained in the housing by another force, the housing would no longer need to embrace the ball completely. Proposed in [21] is a design where the ball is retained with the use of both electromagnetic and hydraulic force. One drawback, general to the active joints, is that in the case of power loss the joint would disengage and the robot would collapse. Other safety measures could be implemented, such as support wires, but this might not always be applicable as the wire could tangle up in other moving parts and so on.

Another option is the use of passive magnets, such as neodymium magnets. This is not uncommon in the world of small-scale robots, where magnetic ball joints have seen multiple applications in PKM 3D printers. This technique has been popular since there is no backlash in the joint and the construction is simple. However, as far as to the knowledge of the author, no large-scale joints based on this principle have been developed. Even with strong rare earth magnets, such as n52 magnets, the weight of the magnet also becomes significant when large attraction forces are required. Strong rare earth magnets are also expensive. While these joints do not need an energy source to work, these could still pose a safety risk. If the magnetic force were to be exceeded, the ball would separate from the housing, and again the robot could collapse or jolt violently. Since the robot is intended for milling, metal shavings could also pose a contamination issue, where it would be attracted to the joint and could get lodged between the ball and housing.

1.3.2 Cardan Joint

The Cardan joint, also referred to as universal joint or Hook’s joint, consists of two revolute joints arranged with its rotational axis perpendicular to each other, as seen in Figure 1.4. This joint structure is often used with parallel robots as it can provide a higher degree of mobility than the standard ball joint. While this joint is not as limited by geometry, it can be limited by singularity, where if the joint is rotated to the position presented in in Figure 1.4 the joint loses a d.o.f, and the joint locks up in one direction. If an additional d.o.f is added to the yoke, such that the joint becomes 3 d.o.f, two of the axes can coincide. The joint then has another singularity where it gains a d.o.f, as seen in Figure 1.4. It is therefore clear that the largest singularity free movement of the Cardan joint around axis-1 is $< \pm 90^\circ$.

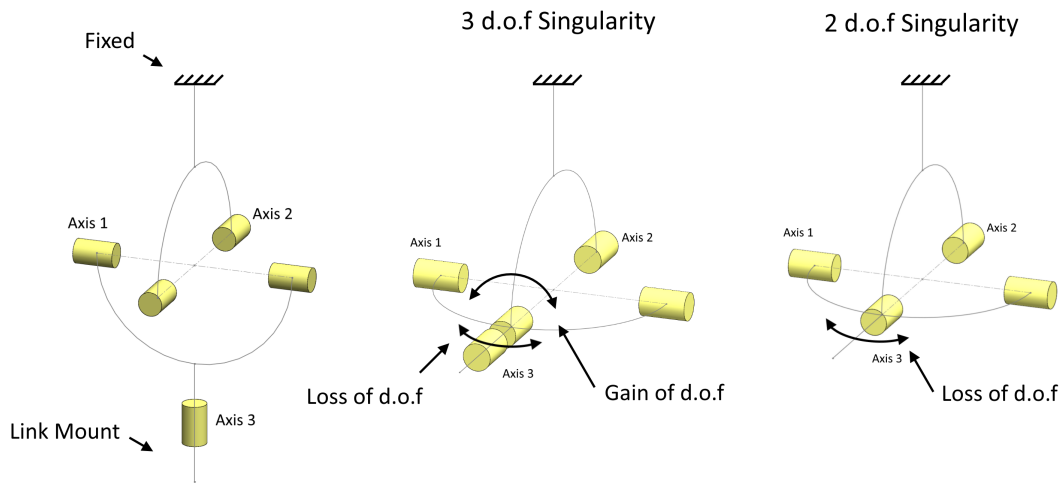


Figure 1.4: Cardan joint structure, normal position(L), singular position(R)

The current solution uses joints that were inspired by the *INA Schaeffler* joint series GLK, seen in Figure 1.5, which are Cardan joints offered with both 2 d.o.f and 3 d.of. These have a stiffness of $50N/\mu m$ and a weight of approximately 1 kg, as it is seen in their catalogue [18] and in [1]. It has a mobility of $360 \times 90 \times 360$ degrees, where the angle limit of 90 degrees is due to the singularity mentioned above.

In the same series of Cardan joints, *INA Schaeffler* also offers larger 2 and 3 d.o.f joints which have a stiffness of $450N/\mu m$ and a mobility of $90 \times 45 \times 360$ degrees. However, as it is seen in the same catalogue [18] these weigh 7 kg, which would, alone, add a wight of 42 kg to the tool platform and are therefore too heavy for the current size of the robot. In between these two joints, they also offer a Cardan joint with the same mobility as the above but at a weight of 3 kg. However, the stiffness of this is $100N/\mu m$, which is only double of the joints in the current solution at three times the weight [22].

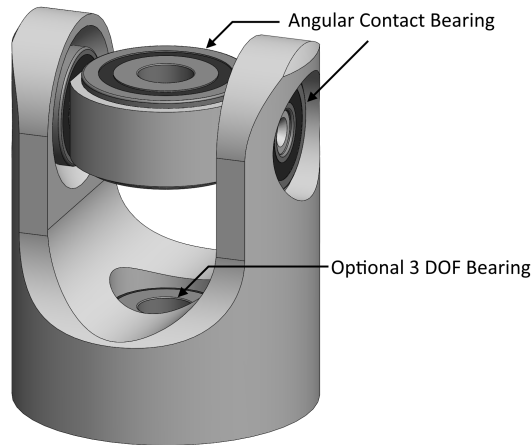


Figure 1.5: INA joint [18], used on current prototype

Another joint, derived from the Cardan joint family, is the joint with offset axis, which is, among others, used on the *Hexapod M850* of *Physik Instrumente* [23]. It is mentioned in [24], that this type of joint can provide twice as high stiffness compared to the regular Cardan joint structure. This is due to the structural freedom that the offset axis offers, where wide needle bearings or bushings can be situated in the centre hub, commonly referred to as the spider. This also allows for a whole axle to be used between both yokes, eliminating the single side supported pin design. The most significant drawback of this design is the fact that the two parts of the joint do not rotate around the same axis. For an accurate kinematic model, the rotation of the centre hub of each joint would need to be calculated, and the complexity of the kinematics is therefore increased.

1.4 Bearing

This part of the literature study was made in conjunction with the joint concept development, where bearings that could support radial and/or axial forces was needed. Bearings can be broadly categorised into two groups, which is rolling element bearing and sliding bearings. The last of these are referred to as plain bearings or bushings. In this report, the word bearing is used as a general term for both rolling element bearing and plain bearings. Presented in this section are the bearings considered to give the highest degree of stiffness, which is needle bearings, cylindrical plain bearings, and spherical plain bearings.

1.4.1 Needle Bearing

Needle bearings can be seen as a special case of a cylindrical roller bearing, where the width of the rollers is much greater than the diameter. Where space is limited, this type of rolling element bearing gives a higher stiffness compared to other roller element bearings. Compared to sliding bearings, these have lower friction losses with friction coefficient of only $\mu = 0.001 - 0.003$ [25].

While regular needle bearings only support radial forces, these can be combined with small angular contact bearings, roller thrust bearings or needle thrust bearings. This combination is also available as a single assembly, which is referred to as a combined needle roller bearing. As with other types of rolling element bearings, radial clearance can also be eliminated by mounting the bearings with a preload. Because of the nonlinear contact condition, this also has the added benefit of increasing stiffness. A drawback of the added preload is the increase in friction, which in turn increases wear of the bearing, shortening its lifespan.

1.4.2 Plain Bearing

Plain bearings are the simplest form of bearing where there are no moving parts internally, and it relies on a sliding interface instead of a rolling interface. One significant advantage of plain bearings is their large contact surface, which gives a high stiffness compared to rolling element bearings. Because of the sliding interface, plain bearings typically have a friction coefficient much higher than rolling element bearings.

A drawback of plain bearings in precision applications is the zero velocity friction, also referred to as stick-slip. To counteract this, the inside face of the plain bearing can be coated or lined with different types of polymers that have better friction characteristics. Two commonly used polymers for this application is PTFE and POM. PTFE has some desirable mechanical advantages such as low friction, virtually no stick-slip, large elastic deformation capability and good dampening characteristics. While raw PTFE has some drawbacks such as high creep rate, low fatigue life, high thermal expansion and low stiffness, it can be mixed with other materials which drastically improves its characteristics. Conventional additives are glass, carbon fibre, metallic particles or by infusing the PTFE in to sintered tin/bronze. While the PTFE composite bearings has virtually no stick slip, their friction coefficient can be up to 0.25.

The plain bearings from *Ampep*, which is a division of *Skf*, claims that their PTFE woven liner has Young's modulus between 5200MPa and 6700MPa [26]. This and the fact that the liner is only 0.30mm to 0.53mm thick and backed by steel results in a plain bearing that still provides a high degree of stiffness. From their catalogue [26], it can be seen that the stiffness of the spherical plain bearings with *Ampep X1* liner is approximately 52% to 64% that of the solid steel variant.

A disadvantage of cylindrical plain bearings is their internal clearance, which is often inevitable in practice. This can be avoided with the use of special polymer bushings from *Igus*, made of their polymer blend *igur-J*, see [27]. This is a more compliant polymer blend which allows for an interference fit and therefore has zero radial clearance. However, as a consequence of this, the stiffness of these are considerably lower as it has a Young's modulus of only 2.4 GPa.

1.4.3 Spherical Plain Bearings

The spherical plain bearing is based on the same principle as the cylindrical plain bearing mentioned above, where it relies on a sliding interface to retain radial motion. The difference is that the contact surface is spherical instead of cylindrical. The spherical bearings are therefore not sensitive to misalignment, but by the same principle, these do not retain any bending moments. The main advantage of these over the above is that their geometry allows for zero clearance fit with a small preload. Spherical plain bearings can also accommodate axial loads, but only to a certain extent. *Skf* recommends that axial load does not exceed 10% of the static load rating, C_0 .

1.5 Linear Bearing

With solutions such as the rack and pinion and the linear motor, the actuator must be externally supported by linear bearings. The load imposed on the carriages, of which the actuators are mounted to, vary significantly with both magnitude and direction. This subjects the linear bearings to large forces, and the stiffness of these affect the stiffness of the robot as a whole. Presented in this section are different types of linear bearings that can be used on the robot.

1.5.1 Rolling Element Bearing

On the current solution, the carriage is supported by one linear ball bearing on each of the two profiled rails. These are *Bosch Rexroth* size 20 bearing blocks with standard length (FNS) [28]. The stiffness of these are nonlinear in terms of applied load, like regular rolling element bearings, but also depends on load direction. An example of this is the bearing blocks on the current prototype, which has a stiffness of $\approx 550N/\mu m$, $\approx 400N/\mu m$ and $\approx 250N/\mu m$, with downwards, upwards and sideways loads. From this, it is clear that side loads are the worst case load condition with less than half the stiffness than the downwards direction.

These bearing blocks also come in an extended version [28], where the increase in stiffness of the long model (FLS) over the short model (FNS) is around 35% of the lowest stiffness, for *Bosch Rexroth* size 25 bearings. Linear bearings are also available with rollers instead of ball elements, which, because of the line contact, provide a higher degree of stiffness for a given bearing block size. With the same size 25 as the current model, the lowest stiffness is doubled to $\approx 500N/\mu m$ with roller bearings from *Bosch Rexroth* [29].

1.5.2 Plain Bearing

Plain bearings can also be used for linear applications with many similarities to the plain bearings used for rotational applications. Like the rotary counterpart, these have considerably higher stiffness than the rolling element bearings. The increased stiffness does however come at a cost, as these usually are not capable of as high speeds and have higher friction losses. As with radial plain bearings running clearance is also an issue. Solutions exist from *Igus* where the running clearance can be adjusted after mounting. While this clearance can be reduced to a few μm , it usually cannot be eliminated entirely. These types of polymer bearings are most commonly seen with circular shaft solutions, but can also take the form of profiled rail systems, which offers a cheaper alternative to the rolling element bearing. Sliding velocity can be a limiting factor with some bearings, but slides with polymers such as *drylin T* of *Igus* claims to offer a surface velocity of up to 15m/s [30].

Another common method used extensively with both modern CNC's and old mills, is the Dovetail slide, box ways or v-ways. Conventionally, these are used with steel on steel contact with grease or thick oil lubrication. While this provides a high degrees of stiffness, it suffers from high friction forces and low-speed capabilities. With the use of a polymer as a boundary layer, such as *Turcite* or *Rulon 142*, friction can be reduced, and travel speeds can be increased. It is claimed by *Birmingham Machining Tool Services*[31], that with *Turcite-B* liner, it is possible to reach speeds over 80 m/min (1.3 m/s). Box ways also require accurate machining and post-processing to give a satisfactory surface quality. This involves the fine art of hand scraping, where the guideways are manually scraped and measured with a surface gauge until it is within the specified tolerance.

2 Kinematics

The kinematics of the Gantry Tau have been well defined in other papers, such as [1], and it is therefore only briefly presented here. While the kinematic parameters of the structure is not the subject of this thesis, some modifications were made and therefore the workspace of the robot had to be investigated. In relation to the design of a tool platform and the joints, an analysis of the joint rotations was also conducted.

2.1 Kinematic Parameters

As mentioned, the Gantry-Tau structure is arranged with link clusters of 3,2 and 1, as seen in Figure 2.1. The cluster of three links can be arranged in different ways, but the prototype at UIA is arranged with a triangular pattern, where the joints on the carriage rotate around one common axis. This Gantry-Tau structure is re-configurable, and as it is seen in [32], that it is possible to re-configure the robot online without encountering singularities. However, this ability was not incorporated in to the design since it poses some limitations of the tool platform, where some structural rigidity weaknesses are unavoidable. Without the possibility of reconfiguration, the selected fixed configuration is presented in Figure 2.1, which is known as the left-handed configuration. This was chosen since it allowed for a closer grouping of the links, where joint E could be placed closer in between joints A and B on the tool platform.

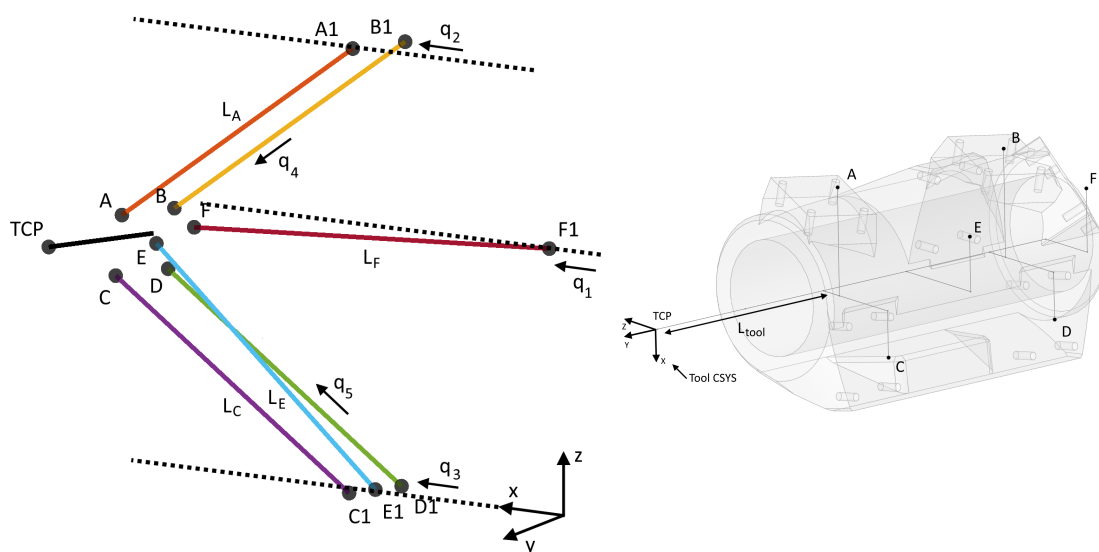


Figure 2.1: Gantry-Tau kinematic structure(L), Tool platform kinematic structure (R)

The kinematic structure of the tool platform is presented in Figure 2.1. The centre of rotation of the joints A to F is defined as Cartesian coordinates relative to the TCP, with the values presented in Table 2.1. Subscript TF indicated coordinates in reference to the coordinate frame of the tool, and no subscript indicates global coordinates. Because all the joints are mounted to the platform at an angle, these coordinates become decimal numbers. Therefore, the values are here presented as a function of the mounting angles, such that these are exact.

	x	y	z
A_{TF}	$-135\cos(20)-5\sin(20)$	$-L_{tool}$	$-135\sin(20)+5\cos(20)$
B_{TF}	$= A_{TF,x}$	$-L_{tool}-250$	$= A_{TF,z}$
C_{TF}	$60-35\sin(5)$	$-L_{tool}$	$-85-35\cos(5)$
D_{TF}	$= C_{TF,x}$	$-L_{tool}-250$	$= C_{TF,z}$
E_{TF}	$-70+35\sin(5)$	$-L_{tool}-125$	$= C_{TF,z}$
F_{TF}	$-85\cos(45)-35/2$	$-L_{tool}-310-35\sin(45)$	$-85\cos(45)-35/2$

Table 2.1: Tool platform kinematic parameters [mm]

The kinematic parameters of the robot are presented in Table 2.2, with reference to the notation given in Figure 2.1. L_{tool} is the virtual length of the tool, which is defined as the distance from the TCP to the first joint, as seen in Figure 2.1. For consistency this was defined as $L_{tool} = 250mm$, since this length is used in other kinematic models of the prototype, which also corresponds with an actual tool length which is conservative. The Y and Z values presented in this table are coordinates on the gantries and are therefore constant.

Description	Value [mm]
L_{tool}	250
L_A, L_C, L_D, L_E	1250
$A1_y, C1_y$	125
$B1_y, D1_y$	-125
$E1_y$	0
$F1_y$	-750
$A1_z, B1_z$	1500
$C1_z, D1_z, E1_z$	0
$F1_z$	750

Table 2.2: Robot kinematic parameters [mm]

2.2 Numeric 5-axis Inverse Kinematics

The Inverse Kinematics (IK) of the robot describes the relationship between the TCP orientation and the position of the five drives. The known input of this is the x, y and z position of the TCP as well as the rotation around the x and z-axis, (r_x and r_z). The rotation r_y is a redundant rotation of the tool, which is an effect of the triangular configuration of the three link cluster. This is not a known input since it is not directly controllable, and was therefore solved along with the drive positions q_1 to q_5 .

The relationship between the global coordinate frame and the tool coordinate frame is then represented by the rotation matrices in equation 2.1 through equation 2.3. The complete rotation around all three axes is then represented by the matrix product in equation 2.4, where the first rotation is around the y-axis, followed by z and x. Since the inverse kinematics is solved numerically, the rotation order is not important, but for consistency this order was used, since it is used in previous kinematic models of the prototype. The initial reason for choosing this is presented in [1], where it is stated that: *"The angle rotation rY is performed first to avoid an additional transformation from the platform Y -axis to the global Y -axis"*

$$R_x(r_x) = \begin{bmatrix} 1 & 0 & 0 \\ 0 & \cos(r_X) & -\sin(r_X) \\ 0 & \sin(r_X) & \cos(r_X) \end{bmatrix} \quad (2.1)$$

$$R_y(r_y) = \begin{bmatrix} \cos(r_Y) & 0 & \sin(r_Y) \\ 0 & 1 & 0 \\ -\sin(r_Y) & 0 & \cos(r_Y) \end{bmatrix} \quad (2.2)$$

$$R_z(r_z) = \begin{bmatrix} \cos(r_Z) & -\sin(r_Z) & 0 \\ \sin(r_Z) & \cos(r_Z) & 0 \\ 0 & 0 & 1 \end{bmatrix} \quad (2.3)$$

$$R(r_x, r_z, r_y) = R_x(r_x)R_z(r_z)R_y(r_y) \quad (2.4)$$

With the rotation matrix in equation 2.4, the global coordinates of the rotation centre of joint A to F , is described by equation 2.5.

$$A = R(r_x, r_z, r_y)A_{TF} \quad (2.5)$$

The objective function to minimise, is then presented in equation 2.6. These functions describe the square of the distance between the endpoints of the links minus the square of the link length.

$$\begin{aligned} obj(1) &= (X + A_x - q_2)^2 + (Y + A_y - A1_y)^2 + (Z + A_z - A1_z)^2 - L_A^2 \\ obj(2) &= (X + B_x - q_2)^2 + (Y + B_y - B1_y)^2 + (Z + B_z - B1_z)^2 - q_4^2 \\ obj(3) &= (X + C_x - q_3)^2 + (Y + C_y - C1_y)^2 + (Z + C_z - C1_z)^2 - L_C^2 \\ obj(4) &= (X + D_x - q_3)^2 + (Y + D_y - D1_y)^2 + (Z + D_z - D1_z)^2 - q_5^2 \\ obj(5) &= (X + E_x - q_3)^2 + (Y + E_y - E1_y)^2 + (Z + E_z - E1_z)^2 - L_E^2 \\ obj(6) &= (X + F_x - q_1)^2 + (Y + F_y - F1_y)^2 + (Z + F_z - F1_z)^2 - L_F^2 \end{aligned} \quad (2.6)$$

To solve this objective function, the nonlinear least squares function *lsqnonlin* in *Matlab* was used. The formulation of the boundary constraints have been proposed in prior reports, such as [1], where the X position of the TCP has been used to describe the limits for the gantry drives, and the redundant angle r_y have been limited to be within an interval of 90 degrees. However, as the tool rotates around r_X and r_Z , this limits valid solutions where the x coordinates of the TCP relative

to the carriages changes with rotation r_Z as well as the redundant angle r_y exceeds the 90-degree interval. For this, it was found to be better to solve the objective function unconstrained, and then check if the solution was valid. To prevent invalid solutions from interfering with the initial values in the next step, the solution was only passed as an initial value to the next step if it was a valid solution. With appropriate initial values for the first step, this was shown to be a robust method.

2.3 Inverse Robot Jacobian

The inverse robot Jacobian matrix describes the relationship between the velocity of the TCP and the five drives. This has previously been derived in [1], but some of the notations have been changed, and it is therefore presented here again. While the redundant angle r_y is not a known variable, it can be obtained from the inverse kinematics. This was therefore treated as a known input variable such that the drives could be represented by equation 2.7 through equation 2.11.

$$q_1 = (X + F_x) \pm \sqrt{L_F^2 - (Y + F_y - F1_y)^2 - (Z + F_z - F1_z)^2} \quad (2.7)$$

$$q_2 = (X + A_x) \pm \sqrt{L_A^2 - (Y + A_y - A1_y)^2 - (Z + A_z - A1_z)^2} \quad (2.8)$$

$$q_3 = (X + C_x) \pm \sqrt{L_C^2 - (Y + C_y - C1_y)^2 - (Z + C_z - C1_z)^2} \quad (2.9)$$

$$q_4 = \sqrt{(q_2 - X - B_x)^2 - (Y + B_y - B1_y)^2 - (Z + B_z - B1_z)^2} \quad (2.10)$$

$$q_5 = \sqrt{(q_3 - X - D_x)^2 - (Y + D_y - D1_y)^2 - (Z + D_z - D1_z)^2} \quad (2.11)$$

The inverse robot jacobian is then described as the derivative of these drive equations with respect to X , Y , Z , r_X and r_Z , with the order of the derivation given by equation 2.12. The derivative of some of these equations are lengthy and were therefore performed with *Maple*, where the code is available in Appendix A.

$$J_q = \begin{bmatrix} \frac{dq_1}{dX} & \dots & \frac{dq_1}{dr_Z} \\ \vdots & \ddots & \vdots \\ \frac{dq_5}{dX} & \dots & \frac{dq_5}{dr_Z} \end{bmatrix} \quad (2.12)$$

2.4 Workspace Analysis

Presented in this section is the workspace analysis that was conducted on the robot. This was done to verify that the kinematic parameters gave a satisfactory workspace, but also to define the workspace limits. The occurrences that can compromise the workspace is link collisions, tool collisions and singularities, which was checked with the methods presented below.

Link collision: Link collision was detected with the methods presented in [33] which was implemented in [1].

Tool platform collision: Tool platform collision with the frame was checked with the coordinates of the joints connected to it against a threshold. These were used as reference points, as the joints on the tool collide with the frame before the tool platform itself. The threshold was defined as a radius of $50mm$, which envelopes the joints, including an additional margin. The surface of the profiled rails were defined as the first point of contact on the frame, which is offset from the centre of the joints connected to the carriage by $\approx 100mm$. This then defines the boundaries $Z > -75mm$, $Z < 1575mm$ and $Y > -850mm$ which all coordinates A to F as well as the TCP has to lie within.

Singularities: As it is presented in [23], the singularities occur when either the robot jacobian or the inverse robot jacobian drops in rank. Since only the inverse robot jacobian is available, the inverse of this was used as the direct robot jacobian.

Non reachable points: To check whether the position is reachable, the validity of the inverse kinematics is checked by first calculating the link lengths from the solution, and then comparing these with the known lengths.

With the kinematic parameters presented above, the reachable workspace with 3-axis and 5-axis motion is shown in Figure 2.2. From this, the workspace limits and the total workspace area presented in Table 2.3 was calculated. These workspace boundaries are later referred to in this thesis as the 3-axis and 5-axis workspace.

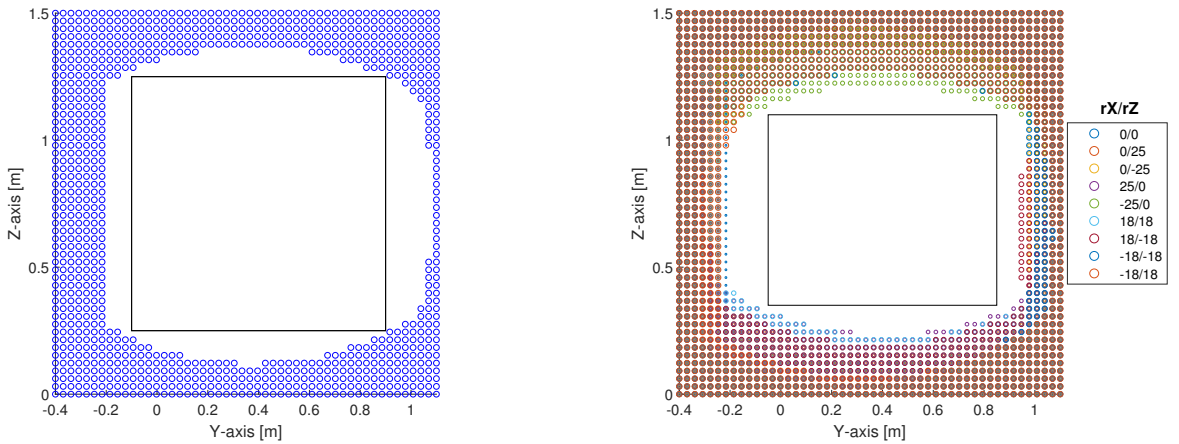


Figure 2.2: Valid workspace, with 3-axis motion (L), with 5-axis motion (R)

	Y (min,max) [mm]	Z (min,max) [mm]	Area [m ²]
3-axis	-100, 900	250, 1250	1
5-axis	-50, 850	350, 1100	0.675

Table 2.3: Reachable coordinates and workspace area

This workspace is valid up until the limits of the gantry drives, which is not specified in this thesis. When the gantries hit their limits, the 3-axis workspace shrinks in the Y and Z axis, as it is presented in [34]. With the above mentioned kinematic parameters, and with 5-axis movement the three gantry drives q_1 , q_2 and q_3 would need at least 1.11m, 1.14m and 1.15m of stroke to not limit the workspace.

2.5 Joint Rotation

From the literature study presented in section 1.3, its clear that the mobility, stiffness an weight of a robots joints are a compromise between one another. Knowledge of the required mobility posed on the joints of the robot is therefore important when selecting or designing joints. This is also vital knowledge when deciding at what positions and angles the joint should be mounted to the tool platform and carriages. The angles of the joints connected through the tool platform and carriage was therefore calculated throughout the workspace with the methods presented in this section.

The centre axis of the joint coincides with the centre axis of the link and can therefore be calculated as the link direction vector by equation 2.13. With 5-axis movement, the rotation of the joints on the tool platform is also affected by the rotation of the tool. These were therefore converted to the coordinate frame of the tool by equation 2.14, which uses the rotation matrix in equation 2.4.

$$\vec{V}_A = \frac{P_A - P_{A1}}{\|P_A - P_{A1}\|} \quad (2.13)$$

$$\vec{V}_{A,T} = R(r_x, r_z, r_y) \vec{V}_A \quad (2.14)$$

From the direction vector, the joint angle can be calculated from equation 2.15 and equation 2.16. Where α and β are the angle the joint makes with the x-z and x-y plane, respectively. V_x , V_y and V_z is the x, y and z component of the direction vector \vec{V} which has a length $r = 1$.

$$\alpha = \sin^{-1} \left(\frac{V_y}{r} \right) \quad (2.15)$$

$$\beta = \sin^{-1} \left(\frac{V_z}{r} \right) \quad (2.16)$$

The other quadrant solutions of \sin^{-1} was handled with the logic presented in equation 2.17. However, the rotation span of the joints does not exceed $\pm 90^\circ$ in any direction, and the other quadrant solutions of \sin^{-1} was therefore not an issue.

$$\begin{aligned} \alpha &= \pi - \alpha, & \text{if } \vec{V}_x < 0 \ \& \ \vec{V}_y > 0 \\ \alpha &= -\pi - \alpha, & \text{if } \vec{V}_x < 0 \ \& \ \vec{V}_y < 0 \\ \beta &= \pi - \beta, & \text{if } \vec{V}_x < 0 \ \& \ \vec{V}_z > 0 \\ \beta &= -\pi - \beta, & \text{if } \vec{V}_x < 0 \ \& \ \vec{V}_z < 0 \end{aligned} \quad (2.17)$$

To find the best mounting orientations of the joints, this direction vector was rotated until the point cloud of the calculated direction vectors \vec{V}_A and $\vec{V}_{A,T}$ yielded angles α and β that were centred around the x-axis. This was done with the same rotation matrix used above. Since these are the rotations required to centre the x-axis to the joint rotations span, it is the opposite offset angles that the joints should be mounted on the tool platform and carriages to minimise the joint mobility requirement. The selected mounting angles are then presented in Table 2.4.

With the joints mounted at these angles, the rotation with 5-axis motion within the 5-axis workspace is presented in Figure 2.3 and 2.4. If tool rotation is not considered the joint rotation presented in Figure 2.5 and Figure 2.6 is obtained within the 3-axis workspace.

	Angle	A	B	C	D	E	F
Carriage	r_x	0	0	0	0	0	0
	r_z	0	0	0	0	0	45°
	r_y	45°	45°	-45°	-45°	-45°	0
Tool	r_x	-20°	-20°	0	0	0	0
	r_z	0	0	0	0	0	-135°
	r_y	-200°	-200°	95°	95°	85°	-45°

Table 2.4: Recommended joint offset angles

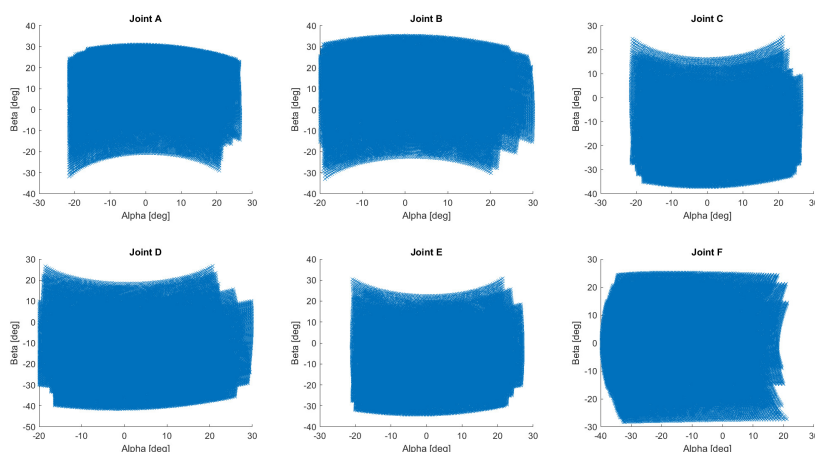


Figure 2.3: Rotation of carriage mounted joints, with 5-axis motion

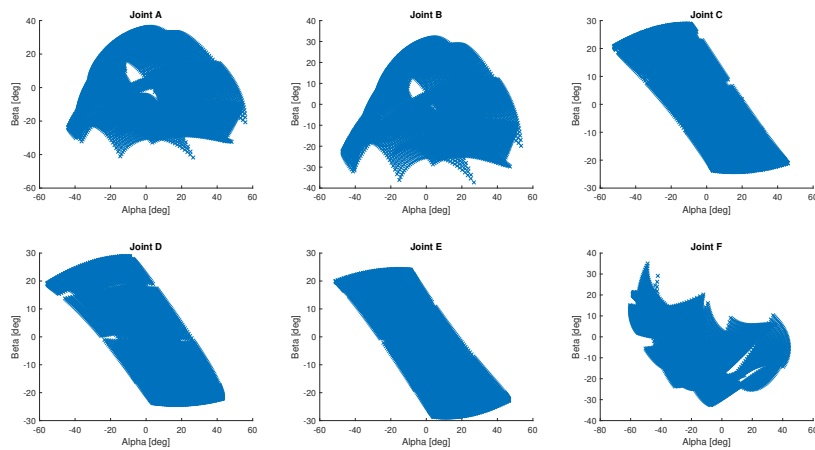


Figure 2.4: Rotation of tool platform mounted joints, with 5-axis motion

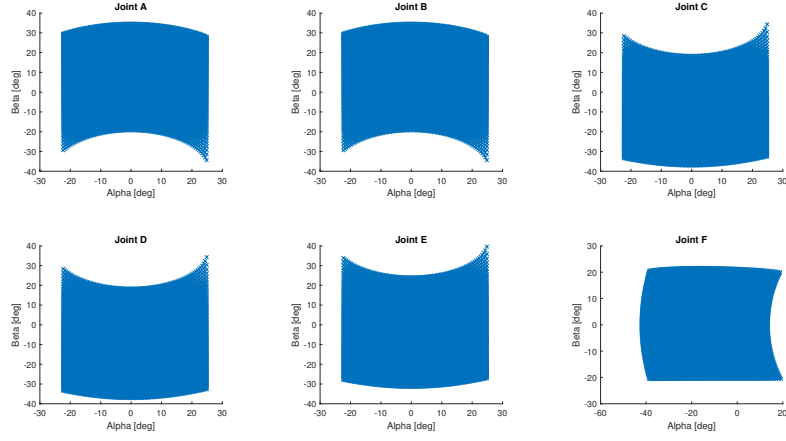


Figure 2.5: Joint rotation with 3-axis motion, carriage mounted joints

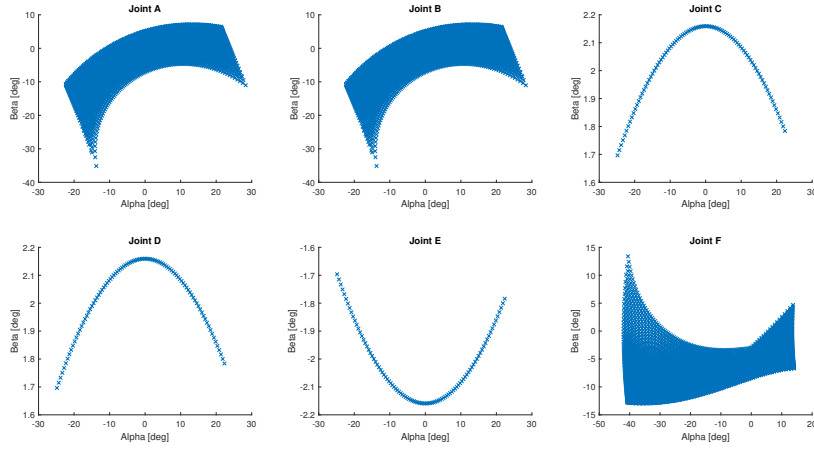


Figure 2.6: Joint rotation with 3-axis motion, tool platform mounted joints

The required mobility of the joints, presented in Table 2.5, is then represented by the maximum and minimum values found from this. All values in this table are rounded up, where the largest absolute rotation of α and β is used to describe the \pm rotation requirement.

Movement	Placement	Angle	A	B	C	D	E	F
3-axis	Carriage	α	$\pm 25^\circ$	$\pm 25^\circ$	$\pm 25^\circ$	$\pm 25^\circ$	$\pm 25^\circ$	$\pm 43^\circ$
		β	$\pm 35^\circ$	$\pm 35^\circ$	$\pm 38^\circ$	$\pm 38^\circ$	$\pm 40^\circ$	$\pm 22^\circ$
	Tool	α	$\pm 29^\circ$	$\pm 29^\circ$	$\pm 25^\circ$	$\pm 25^\circ$	$\pm 25^\circ$	$\pm 42^\circ$
		β	$\pm 36^\circ$	$\pm 36^\circ$	$\pm 2.5^\circ$	$\pm 2.5^\circ$	$\pm 2.5^\circ$	$\pm 14^\circ$
5-axis	Carriage	α	$\pm 27^\circ$	$\pm 30^\circ$	$\pm 27^\circ$	$\pm 30^\circ$	$\pm 27^\circ$	$\pm 43^\circ$
		β	$\pm 35^\circ$	$\pm 36^\circ$	$\pm 38^\circ$	$\pm 42^\circ$	$\pm 35^\circ$	$\pm 29^\circ$
	Tool	α	$\pm 56^\circ$	$\pm 54^\circ$	$\pm 52^\circ$	$\pm 56^\circ$	$\pm 52^\circ$	$\pm 61^\circ$
		β	$\pm 42^\circ$	$\pm 38^\circ$	$\pm 29^\circ$	$\pm 29^\circ$	$\pm 29^\circ$	$\pm 35^\circ$

Table 2.5: Required joint mobility with 3-axis and 5-axis motion with $r_x = \pm 25$ and $r_z = \pm 25$

3 Joint Design

The joint is an essential part of any parallel robot, and as it is seen with the current prototype, it is one of the limiting factors. Since most existing joints with a high degree of stiffness are either heavy or limited in mobility, it was desirable to see if a joint concept could be developed to improve on this.

This chapter presents the two joint concepts that were developed. The first part of this, presents the analysis that were conducted on material selection, which also applies to the design of the machine presented in Chapter 5. Then presented, is the stiffness calculations that were performed on different bearing types, where it is also shown an application example, where two of the bearing types are evaluated under comparable conditions. In the last part, the two joint concepts are presented.

3.1 Material

In this section, three types of material are presented, where the characteristics of each are evaluated. The three materials that were considered for construction of the joint and other parts of the robot were aluminium, steel and carbon fibre. With the process of material selection, a well-known parameter is the specific modulus, also known as specific stiffness of the material. This can be calculated by equation 3.1, which is the ratio of the young's modulus, E , over the density ρ .

$$K_s = \frac{E}{\rho} \quad (3.1)$$

The values obtained from this formula is very general for most metals since the variation of Young's module within a specific metal is relatively small. Composites with carbon fibre, can, however, vary greatly depending on factors such as fibre composition, fibre orientation, load direction, production quality, resin type etc. The carbon fibre composite that was chosen for the comparison is pultruded *IM7* carbon fibre with *Epon 828* resin. The properties of this were investigated in [35] where the compressive strength of pultruded carbon fibre rods of two types where tested. The steel chosen for the comparison is grade 416 stainless steel since it has good machinability and a decent resistance to corrosion. Aluminium alloy 6061 was chosen because of its availability and low cost.

Type	CF IM7/828 [35]	steel 416	Aluminum 6061-T6	Unit
Density	1600	7800	2700	kg/m^3
Young's modulus	186	205	68.9	GPa
Specific stiffness	116.25E+6	26.28E+6	25.52E+6	Nm/kg

Table 3.1: Specific stiffness of carbon fibre, steel and aluminium

As it is seen in Table 3.1, the material with the highest specific stiffness is carbon fibre. It does have its limitations, where if standard profiles, such as those produced by pultrusion, can not be used, it is considerably more expensive than the other two. It can also be seen that aluminium and steel have virtually the same specific stiffness. However, where space is the limiting factor, it's clear that steel will offer the highest stiffness, due to the higher Young's modulus. Where volume is not a limiting factor, but the weight is, it can be seen that aluminium can provide a better design as the weight is not accumulated as quickly for parts that require a certain size, such as the tool platform and the carriages.

3.2 Bearing Stiffness

To constrain the relative motion of all the parts of the joint except rotational, bearings of some sort was needed. Since these are the only connection between the parts, the stiffness of these significantly affects the total stiffness of the joint. It was therefore desirable to investigate what level of stiffness which is to be expected from the bearings presented in section 1.4. Some of the bearings in the joints are subjected to both radial and axial loads, therefore, both the axial and radial stiffness of the different bearing types were investigated.

3.2.1 Plain Bearing

To determine the radial stiffness of composite plain bearings, such as the PTFE based composite bushing, FEM (Finite Element Method) simulations were conducted. The dimension of the simulated bushing sizes is presented in Table 3.2 with reference to the notation given in Figure 3.1. The dimensions of the bearings presented here are based on the available sizes in the catalogue of *Ampep*, which can be found at [26].

The radial stiffness was simulated with the quarter symmetry model presented in Figure 3.2. This incorporates a dummy housing, which is rigidly supported, where a load of 1000N is applied to a dummy shaft with a uniform surface traction. Friction between the bearing and the axle is defined as frictionless $\mu = 0$ and between steel parts it is defined with $\mu = 0.4$. The thickness of the PTFE lining is 0.3mm and defined with Young's modulus of 5.2GPa and Poisson's ratio of 0.3. The backing of the bushing is stainless steel, which is assumed to have Young's modulus of 205GPa and a Poisson's ratio of 0.283, which corresponds to 416 stainless steel.

The radial stiffness of three bearing sizes is presented in Table 3.2. An example of the simulation result is the radial deformation presented in Figure 3.2, which is a bearing with a bore of, $d = 22mm$. The relative deformation of this bearing is $0.302\mu m$ giving it a stiffness of $\approx 3300N/\mu m$.

The axial stiffness is simpler than the case of radial stiffness, where the stiffness can be represented with equation 3.2. t is the thickness of the flange, and A is the area in contact.

$$K = \frac{EA}{t} \quad (3.2)$$

However, these bearings are constructed of a PTFE composite backed by stainless steel, and therefore an equivalent Young's modulus, E_{eq} , was defined by equation 3.3. With a PTFE layer of 0.3mm and a flange thickness $t = 1.5$, the equivalent Young's modulus, E_{eq} , is 15.74GPa. The axial stiffness of the three bearing sizes is then presented in Table 3.2.

$$E_{eq} = \left(\frac{t_1}{E_1} + \frac{t_2}{E_2} \right)^{-1} \quad (3.3)$$

d [mm]	D [mm]	W [mm]	W_{lin} [mm]	B [mm]	b [mm]	t [mm]	K_r [N/ μ m]	K_x [N/ μ m]
18	22	20	18	28	20	1.5	2219	3165
22	26	20	18	32	24	1.5	3300	4450
25	30	20	18	36	27	1.5	2670	4673

Table 3.2: Composite flange plain bearing stiffness [26]

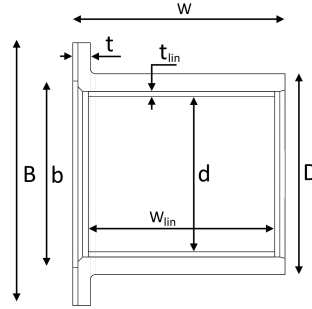


Figure 3.1: Flange plain bearing dimension

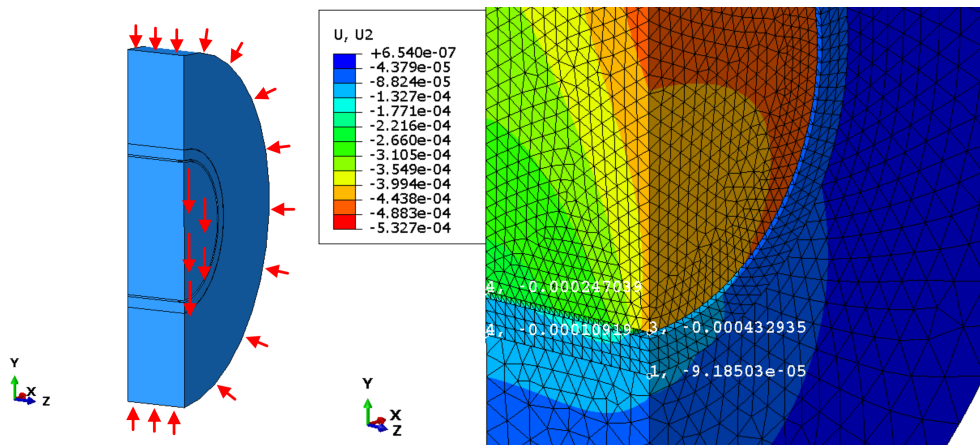


Figure 3.2: Composite plain bearing FEM model setup (L), deformation radial load 1000N (R)

3.2.2 Spherical Plain Bearing

The stiffness of the spherical plain bearing was also calculated by FEM simulations, using the same FEM setup as the above. This spherical bearing was a composite spherical plain bearing in the *Ampep* series [26], which has a thin layer of PTFE composite, with the same properties as the plain bearing presented above. The dimensions of the simulated bearing is presented in Table 3.3, with reference to the notation given in Figure 3.3. From the simulation result, shown in Figure 3.4, the relative deformation of the bearing is $0.504\mu\text{m}$ which gives a radial stiffness off $\approx 1980\text{N}/\mu\text{m}$.

The axial stiffness of a spherical bearing was also simulated, but this time with axis symmetry with the setup presented in Figure 3.3. Presented in Figure 3.4 is the axial deformation of the bearing with a load of 1000N , applied downwards. The bearing raceway is in this case simplified as a rigid tie connection with the dummy hub. The relative deformation of the bearing is then $2.74\mu\text{m}$ which gives the bearing an axial stiffness of $365\text{N}/\mu\text{m}$.

d[mm]	D[mm]	ϕB [mm]	W[mm]	H [mm]	K_r [N/ μm]	K_x [N/ μm]
17mm	30mm	27.31	14.5	18	1980	365

Table 3.3: Spherical plain bearing dimensions [26]

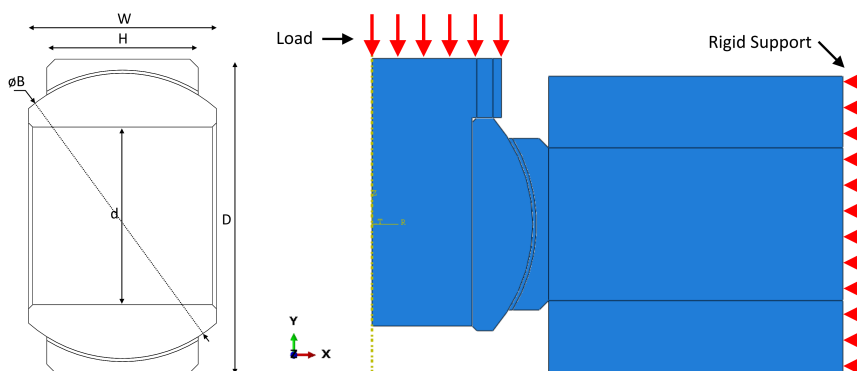


Figure 3.3: Spherical plain bearing dimension (L), axial load simulation setup (R)

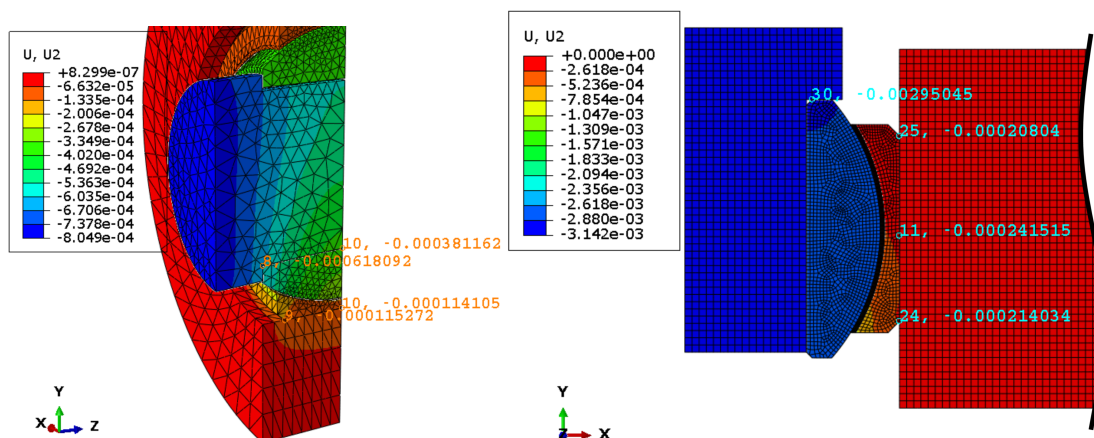


Figure 3.4: Spherical plain bearing deformation, radial load 1000N (L), axial load 1000N (R)

It should be noted that with loads in this direction, the friction between the ball and liner is more critical, where a higher friction increases the stiffness of the bearing. Seen in Figure 3.5 is a simulation with same load case as above but with a friction coefficient $\mu = 0.1$ instead of $\mu = 0$. Also, if preload is included, in the form of an interference fit between ball and axle or raceway and hub, the stiffness is also increased. Also presented in Figure 3.5 is the result of a simulation including an interference fit of $3\mu\text{m}$ between the raceway and housing without friction between the ball and the liner. Friction between steel parts were left at $\mu = 0.4$. From this, the relative deformation with the two cases is $2.24\mu\text{m}$ and $1.86\mu\text{m}$, which gives an axial stiffness of $446\text{N}/\mu\text{m}$ and $538\text{N}/\mu\text{m}$. Note that the deformation of $1.86\mu\text{m}$ is larger than what is seen in Figure 3.5, which is because the deformation from the first frame, the interference fit (not shown here), is positive $0.36\mu\text{m}$ at the reference point.

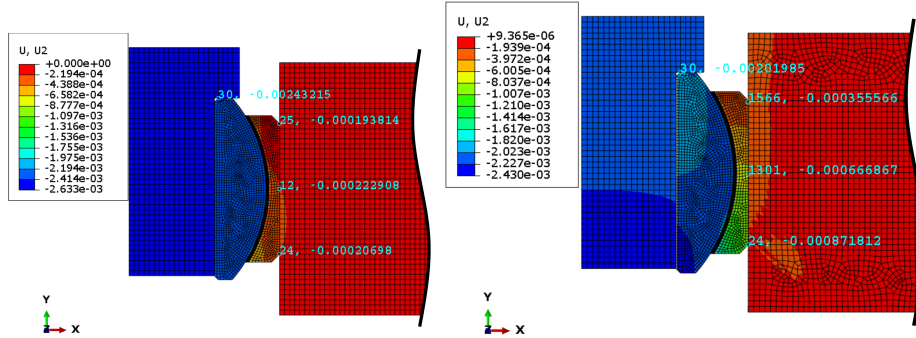


Figure 3.5: Composite spherical plain bearing deformation, axial load, tie connection $\mu = 0.1$ (L), interference fit $\mu = 0$

3.2.3 Needle and Roller Rearing

One important characteristic of rolling element bearings, in general, is the contact between the elements and the raceway. In an unloaded bearing, this contact is in the form of a point(ball) or a line(roller). When the elements deform elastically, the contact area increases, which makes the stiffness of the bearing inherently nonlinear. A common method for describing this contact relationship is with the use of the Hertzian contact theory. There are several theories developed to describe the relationship between applied force and deformation of the rolling element bearings, such as the equations presented in [36]. Also, it is supplied by some manufacturers such as *INA Schaeffler*. From their page [37], the relationship between the radial load, F_r , and the radial deformation, δ_r , is represented by equation 3.4.

$$\delta_r = \frac{F_r^{0.84}}{K_c d^{0.65}} + \frac{s}{2} \quad (3.4)$$

K_c is a stiffness parameter which depends on the geometry of the bearing. For the NKI series bearings, this is given as $K_c = 4.4B^{0.8}/d^{0.2}$, where B is the width of the bearing and d is the diameter of the bore. s is the internal radial clearance, which is not considered here. From this, the radial stiffness of various bearing sizes is presented in Figure 3.6.

While a needle bearing does not support any axial loads, it can be paired with a ball, roller or needle thrust bearing. This can be in the form of a roller thrust bearing such as the K811 series, which occupies comparably the same radial space as the flange plain bearing presented above and

was therefore used for the comparison. From INA's own page [37], the relationship between the axial load, F_a , and the axial deformation, δ_a , is represented by equation 3.5. Where K_c is in this case constant an equal to 36.7. F_{av} is the axial preload of the bearing, which is not considered here. From this, the axial stiffness of various bearing sizes is presented in Figure 3.6.

$$\delta_a = \frac{1}{K_c d^{0.65}} [(F_{av} + F_a)^{0.84} - F_{av}^{0.84}] \quad (3.5)$$

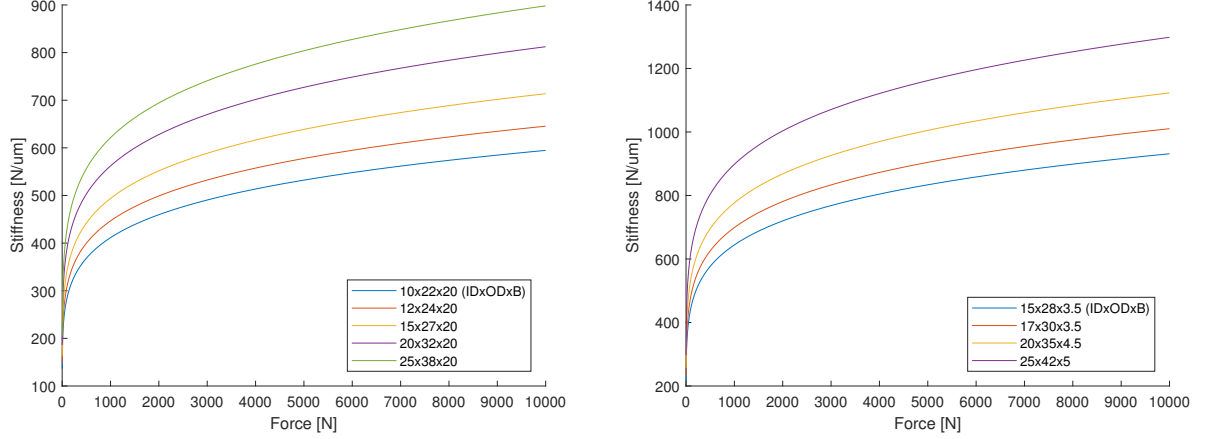


Figure 3.6: Radial stiffness of NKI series bearings(L), axial stiffness of K811 series bearings (R)

3.2.4 Application Example

From the result above, it is clear that the simple cylindrical plain bearing has the highest stiffness compared to its size. However, the accuracy of these are limited by the radial running clearance. Spherical plain bearings can be used with zero clearance and is therefore preferred over regular cylindrical plain bearings. These are however limited to applications where the load is mostly radial, as the axial stiffness of these are not as good.

Care must also be taken when evaluating the above results, as the different bearings have some characteristics that affect the stiffness of the whole assembly. While spherical bearings have the advantage of being less sensitive to misalignment, by the same principle these do not retain any bending forces (if friction is neglected). It also occupies more space than cylindrical plain bearings which reduces the stiffness of supporting structures. The difference between these is therefore best evaluated in a representative assembly of the joint.

Presented in the following figures are two simulations of a former iteration of the ball joint concept, where two bearings are needed to support the joint body. Presented in Figure 3.7 and Figure 3.8 is the deformation of the joint using PTFE lined flange plain bearings. To support loads in both directions, two of these were used on each bracket, where the dimension is the same as the $d = 18mm$ bearing presented in Table 3.2, but with $W = 10mm$. Shown in the same figures are the same joint, but with the spherical plain bearing presented in Table 3.3. As a simplification, the threaded cup that retains the ball when the load is in compression is not modelled here.

The first load condition, in Figure 3.7, is when the link is perpendicular to the rotation axis of the bearings. The second load condition, in Figure 3.8, is when the link makes an angle of 45 degrees, which is the worst case condition regarding the spherical plain bearings. The load is a pulling load of 1000N applied to the face of the link adapter, see section 3.3, and the underside of the platform brackets is rigidly constrained.

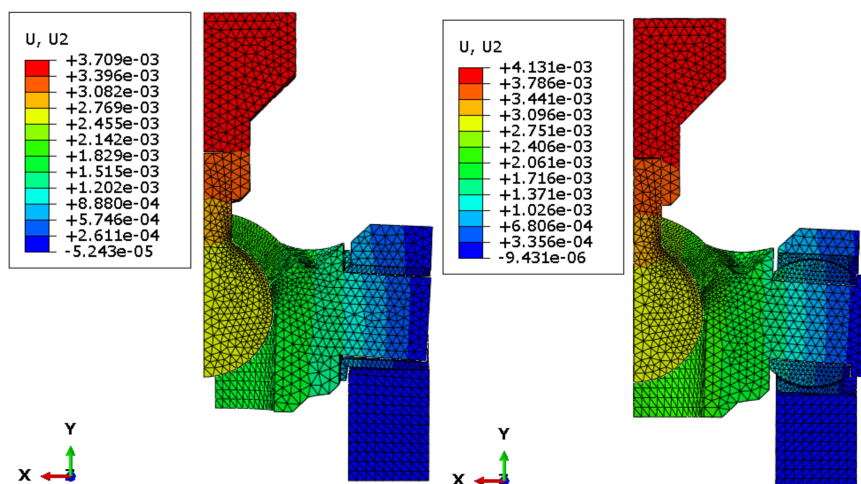


Figure 3.7: Ball joint at 0 deg. W/ flange plain bearing (L), W/ spherical plain bearing (R)

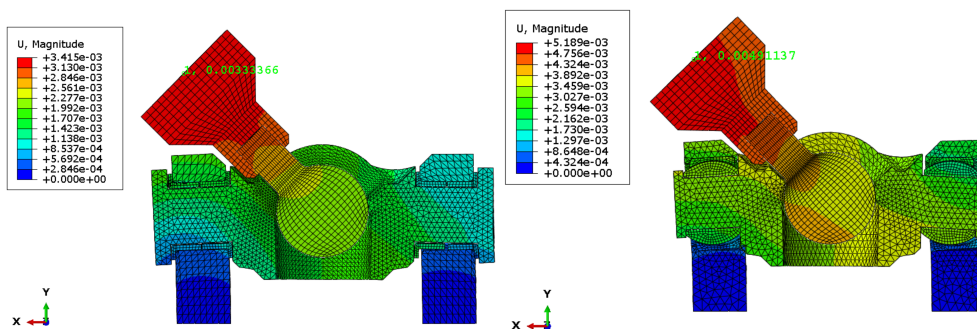


Figure 3.8: Ball joint at 45 deg. W/ flange plain bearing (L), W/ spherical plain bearing (R)

From this, it is observed that the joint construed with flange plain bearings have 11% higher stiffness when the link is perpendicular to the joint and loaded in tension, see Figure 3.7. With the link at 45 degrees, see Figure 3.8, the stiffness of the joint with flange plain bearing is 47% higher than the spherical plain bearing equivalent.

It must be noted that these simulations are quite simplified and are of a former iterations of the joint design, and therefore only serves to compare the two bearing types. The actual stiffness of the ball joint is presented in Chapter 4.

3.3 Ball Joint

With ball joints, the compromise between mobility and rigidity mainly boils down to how far the housing wraps around the ball. To avoid some of the compromises of regular ball joint, a design was made where one of the pivot angles was restricted, making the ball joint a 2 d.o.f joint. It was then possible to increase the mobility along the unrestricted axis, with less effect on the stiffness. The lost d.o.f was then regained by using bearings, as seen in Figure 3.9. Drawings of the individual parts, with dimensions, are available in Appendix C.

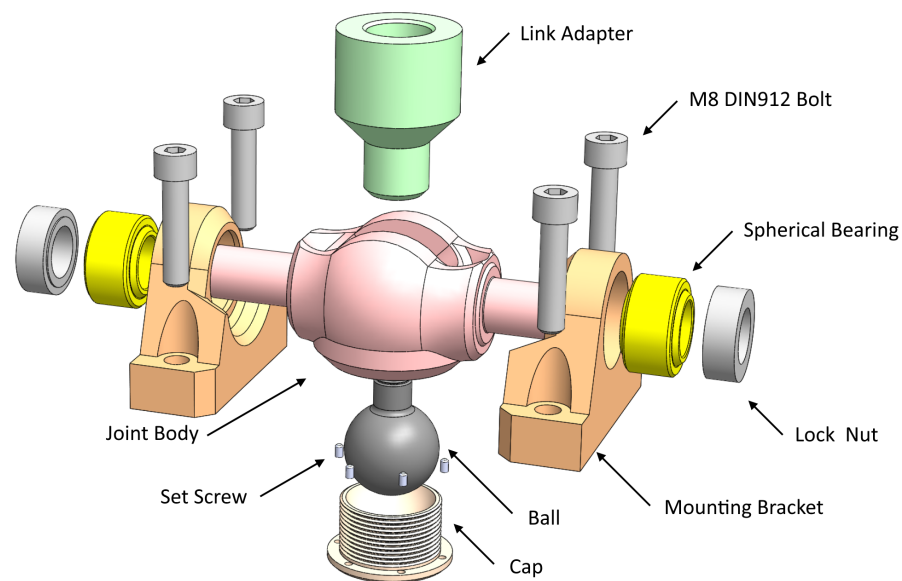


Figure 3.9: Ball joint design, exploded view

This joint consists of five main components, which is a ball, joint body, spherical bearings and mounting brackets. The link and joint is connected together with a link adapter, which is presented in the section below. The mounting brackets and the tool platform is connected with four 35mm M8 bolts. To mount the spherical bearings to the joint body, bearing lock nuts such as [38], can be used, and to fix the raceway to the platform bracket, it is proposed that the raceway of the bearing is mounted with an interference fit.

While it is shown in the previous section that cylindrical plain bearings will yield a stiffer joint, the proposed design uses spherical plain bearings. This was mainly chosen because of the zero-operational clearance these can be delivered with, which makes it possible for the joint to have zero backlash. Also, because these are less sensitive to misalignment, the accuracy requirement of the machined parts should be lower.

With all parts made of steel, the joint comes in at a weight just under 2.1kg. The mobility of the joint is defined as $\pm 70^\circ$ around axis-1 and $\pm 45^\circ$ around axis-2.

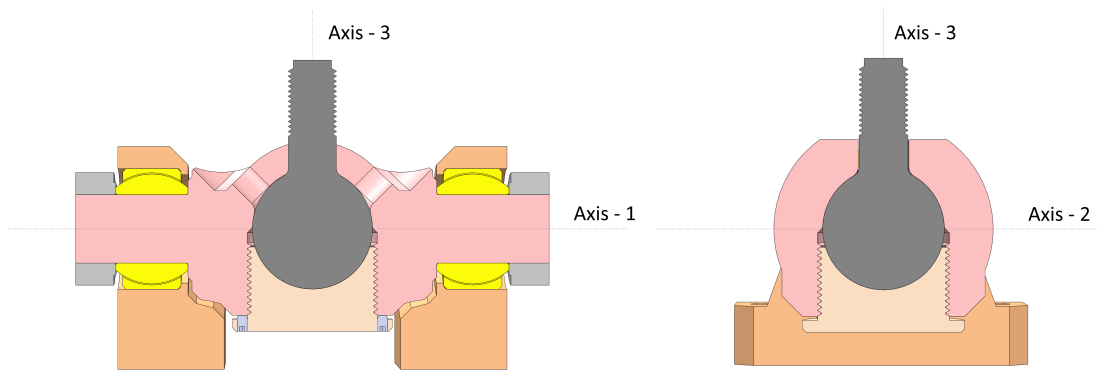


Figure 3.10: Ball joint design, cut view with rotation axes

3.3.1 Link Adapter

To mount the carbon fibre rod to the ball of the joint, the link adapter presented in Figure 3.11 was constructed. It is proposed that this is mounted to the carbon fibre rod with use of epoxy or similar two component glue. The ball is attached with a 12mm metric thread. To preload the threads, such that there is no play in the connection and to lock the threads, the ball can be screwed in until it hits the bottom of the hole in the adapter. If this is not sufficient to retain the rotational force between the joint and link, it is suggested that a set-screw can be used, as shown Figure 3.11. Optionally, another threaded nut can be used on the shaft of the ball which can be tightened against the link adapter.

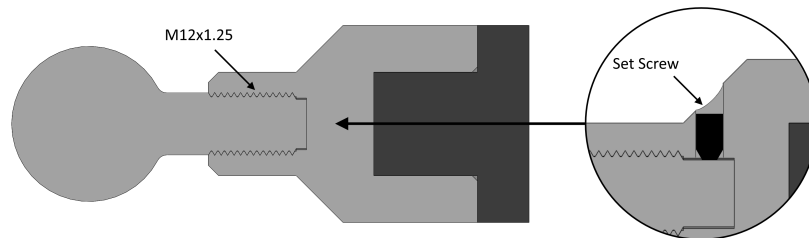


Figure 3.11: Ball joint link adapter (L), optional set screw (R)

3.3.2 Joint Cap

To support the ball when the joint is subjected to compressive loads, the threaded cap with a ball socket presented in Figure 3.12 was constructed. This is suggested to have a 32mm metric thread with a pitch of 1.5mm. To prevent the cap from rotating with the ball and to eliminate any clearance in the thread, six (or more) m2.5 sets screws are suggested to be used.

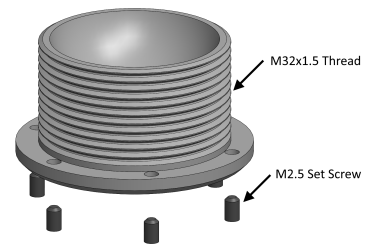


Figure 3.12: Ball joint threaded cap

3.4 Cardan Joint

The second joint design was based on the Cardan joint structure, which is a structure often used with parallel robots, as it can provide a higher degree of mobility than the standard ball joint. One design challenge with this joint structure, is that the centre hub needs to be fitted in between the yoke. The yoke is commonly referred to as the frame of the joint which connects the centre hub, in this case, to the link. This was solved by splitting the yoke, where two plates are bolted to a centre bracket with M8 bolts, as seen in Figure 3.13. The bearings in the joint are a combination of spherical plain bearings and flange plain bearings. In this case, the spherical bearings are only loaded with radial loads, and it is seen as sufficient with a light interference fit of the bearing in both the centre hub and the side plates. The centre hub houses two 22x26x28 flange plain bearings, with the same dimensions as the $d = 22mm$ bearings in Table 3.1, but with $W = 28mm$. These bearings supports a shaft which in turn is supported by the mounting brackets. To accurately control the clearance between the two brackets, a lock nut, such as [38], is suggested to be used on the end of the shaft. Drawings of the individual parts, with dimensions, are available in Appendix D.

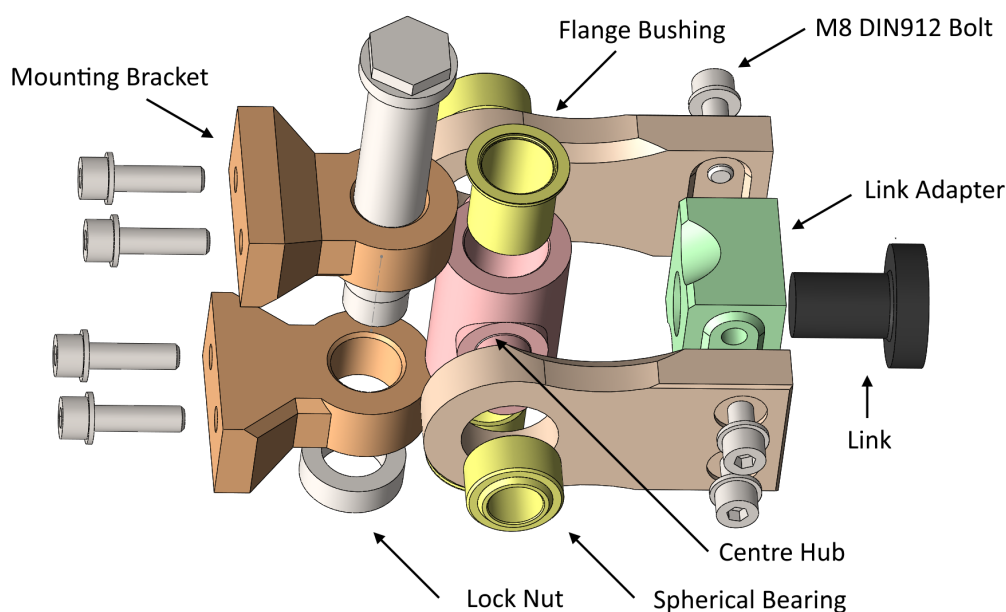


Figure 3.13: Cardan joint, exploded view

With all parts made of steel, the joint comes in at a weight of 3.5kg. The mobility of the joint is not as independent as the ball joint presented above. The joint can rotate up to $\pm 55^\circ$ around axis-1 but is then limited in rotation of $\pm 35^\circ$ around axis-2, see Figure 3.14. The joint can rotate up to $\pm 90^\circ$ around axis-2, but this limits the rotation around axis-1 to just $\pm 10^\circ$. Because of these limitations, the usable mobility was defined as $\pm 50^\circ$ rotation around axis-1 and $\pm 40^\circ$ rotation around axis-2 or $\pm 40^\circ$ rotation around axis-1 and $\pm 50^\circ$ rotation around axis-2.

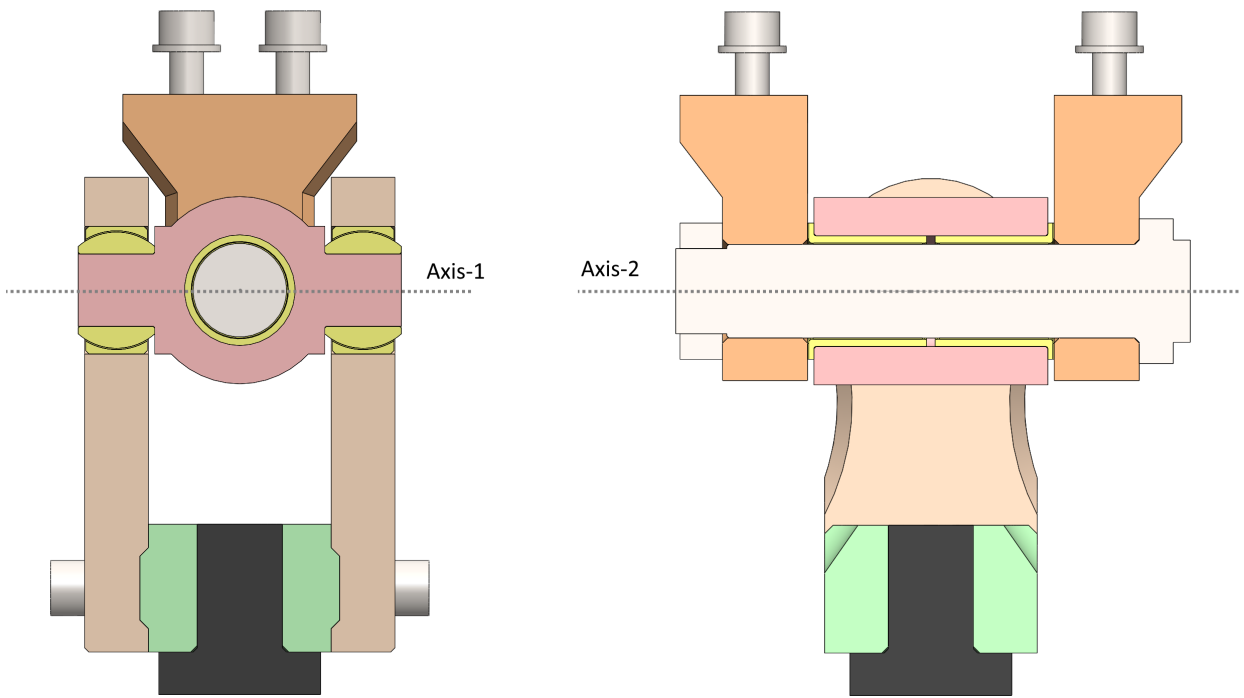


Figure 3.14: Cardan joint, split view

3.4.1 Link Adapter

The Cardan joint can be mounted to the carbon fibre rod in the same manner as the ball joint with the link adapter presented in Figure 3.15. The 45-degree tapered groove is used to reinforce the bolted connection with the side plates since it is slip-critical. The Cardan joint can be converted to a 3 d.o.f joint if another adapter were to be used here, where it could then house thrust bearings.



Figure 3.15: Cardan joint link adapter

4 Joint Stiffness

Presented in this chapter, is the theoretical stiffness of the two joint concepts, which was analysed with the use of *Abaqus* (FEM software). First presented is the 3 d.o.f ball joint where an additional design choice and the effect it has on the stiffness is presented. Then the 2 d.o.f Cardan joint is presented.

4.1 Ball Joint

The load conditions of the joint can be divided in to four load cases, which is when the joint is perpendicular to its mounting face and when it is at the maximum mobility limits. With the ball joint, these maximum limits was defined as when the joint is rotated with $\pm 45^\circ$ and $\pm 70^\circ$ around axis-1 and axis-2. The simplest load-case, is the first of these where quarter symmetry was utilised. The bolted connection was simulated with a preload of 5kN, (bolt load function, see [39]), against a dummy plate of aluminium, see Figure 4.1. Friction between steel mating faces are defined with a friction coefficient of $\mu = 0.4$, and bearing friction is set to frictionless. The bottom face of this dummy plate was rigidly supported and the load was applied to the shaft of the ball with an MPC-constraint, (Multi-Point Constraint, see [40]), simulating a rigid connection. The raceway of the bearing was simulated with an interference fit of $5\mu m$.

Shown in Figure 4.1 is the deformation of the joint with a load of 1000N. Due to the combination of interference fit and preload, the joint is initially displaced at the reference point by $+0.930\mu m$. Subtracting this from the simulation result gives a total deformation of $3.268\mu m$, which means that this part of the joint assembly has a stiffness of $306N/\mu m$.

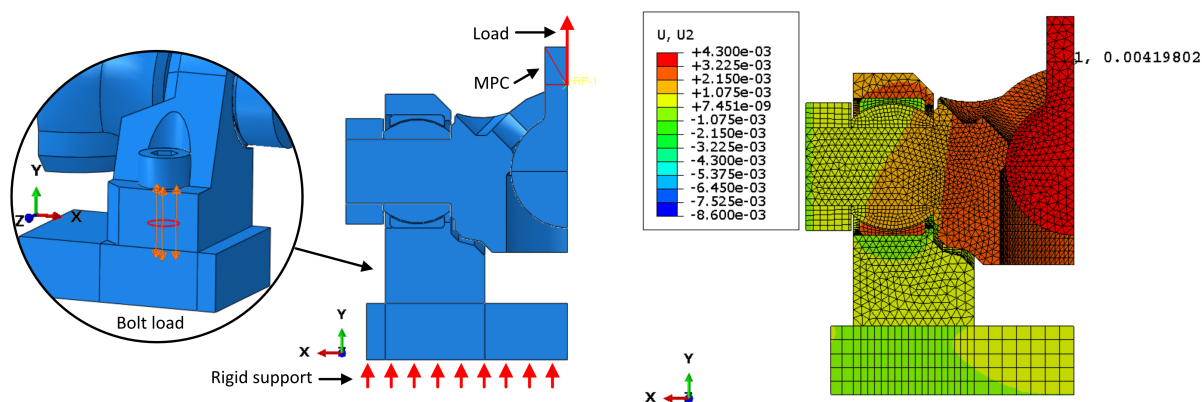


Figure 4.1: Ball joint quarter symmetry, simulation setup (L), simulation result (R)

4.1.1 Link Adapter

The link adapter was omitted from the analysis above since an accurate model including the threads were not feasible in the solid body simulation. This was then simulated together with the ball, including the M12x1.25 thread using axis symmetry, as seen in Figure 4.2. The bonding glue between the rod and link adapter was simplified as a rigid tie constraint. The link is carbon fibre composite, but it was simulated as an isotropic material with Young's modulus of 180GPa and Poisson's ratio of 0.3.

The deformation of this assembly is presented in Figure 4.2, where the applied load is 1000N. Deformation measured at the same reference point used in the simulations without the adapter is $1.253\mu m$, which means that the assembly has a stiffness of $798N/\mu m$.

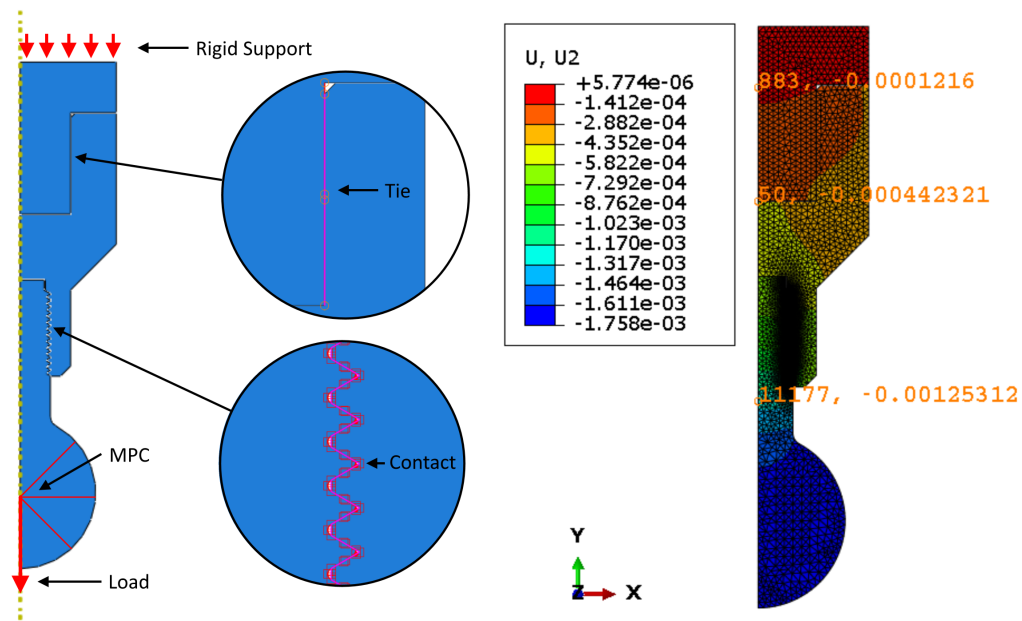


Figure 4.2: Link adapter simulation, FEM setup (L), Deformation w/ 1000N load (R)

4.1.2 Joint With Rotation

In order to investigate how the stiffness changed with the rotation of the joint, it was separated as it is shown in Figure 4.3, since the complete joint assembly was too substantial to simulate at once. The first part of the joint, the body, ball, bearings and lock nuts were then simulated, where the bearing raceway was rigidly supported on the surface, as seen in Figure 4.3. The interference fit of the bearing was not included and symmetry was defined in the x-y plane. Presented in Figure 4.4 is the stiffness of this with the load at an angle from 0° to 45° around axis-2 (see Figure 3.10). The second part of the joint, the bracket, bolts, dummy plate and bearing raceways, was then simulated. This simulation included the same bolt preload and bearing interference fit as the quarter symmetry model presented above. The joint body was modelled as a rigid body with the use of MPC-Constraints, as seen in Figure 4.3. Link MPC-Constraints were used between the raceway and rigid body to allow it to rotate as the actual spherical bearing would. The lower face of the dummy plate was rigidly constrained in all directions. Presented in Figure 4.4 is the stiffness of this with a load at an angle from 0° to 45° around axis-2, but also at various angles around axis-1.

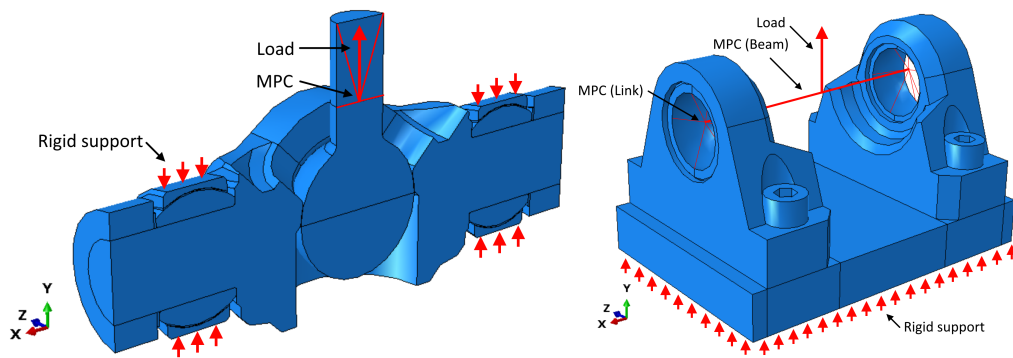


Figure 4.3: Ball joint simulation setup, body and bearing(L), bracket and bolt connection (R)

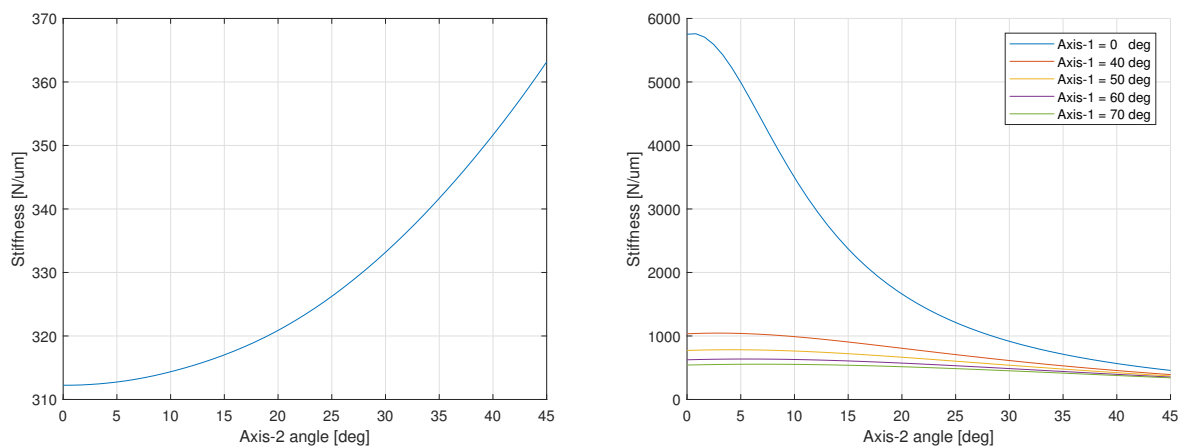


Figure 4.4: Stiffness of ball joint with rotation, body and bearing (L), mounting bracket (R)

The total stiffness of the joint assembly at these load angles were then combined after the simulation, with the relationship $K_{tot} = (1/k_{bdy} + 1/k_{brkt} + 1/k_{lka})^{-1}$. Where k_{bdy} is the stiffness of the joint body, k_{brkt} is the stiffness of the mounting brackets and, k_{lka} , is the stiffness of the link adapter. The combined stiffness of the joint at different angles is then presented in Figure 4.5.

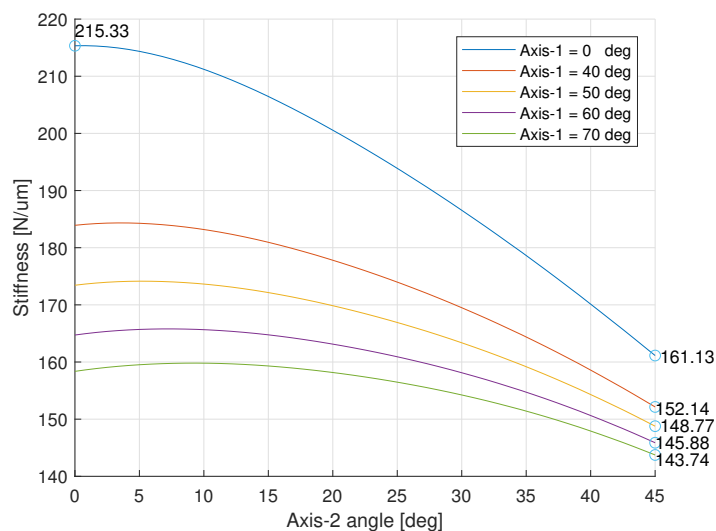


Figure 4.5: Total ball joint stiffness with rotation of axis-2

4.1.3 Compression Stiffness

In the results presented above, the stiffness is only evaluated with a tensile load, as it was presumed to be more critical than a compressive load. While the ball will have a larger contact surface in compression, the stiffness of the joint is in this case also affected by the stiffness of the threads between the cup and the joint body. To investigate this, the cup was modelled including the M32x1.5 threads. Because of the large number of elements that a solid body simulation would require, axis symmetry was used with the model setup presented in Figure 4.6. The deformation of the threads with a load of 1000N is then presented in Figure 4.6. From this, it is seen that the relative deformation of the thread is $< 0.04\mu\text{m}$, which implies that the stiffness of the thread section is in excess of $25000\text{N}/\mu\text{m}$, and is therefore not considered to be a limitation.

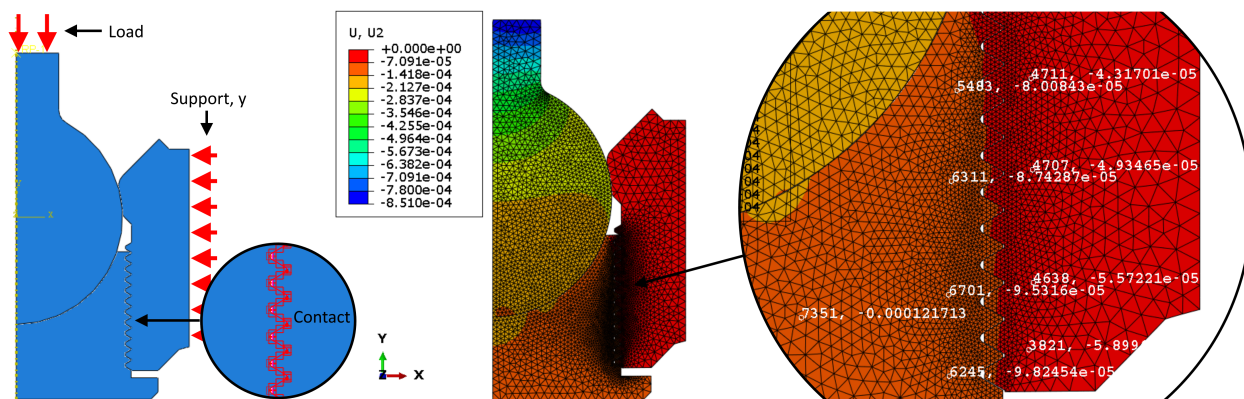


Figure 4.6: Joint cap simulation, FEM setup (L), thread deformation (R)

4.1.4 Ball Polymer Liner

With all the results presented above, the contact interface between the ball and housing was steel to steel contact (but frictionless in simulations). This surface can be lubricated in order to reduce friction, but the effects of stick-slip could still be present. It is therefore proposed that either the ball or the housing is coated with a PTFE composite layer similar to the liner used in the plain bearings from *Ampep*. An application example of this is illustrated in Figure 4.7, where the liner is applied to the joint body and the cap.

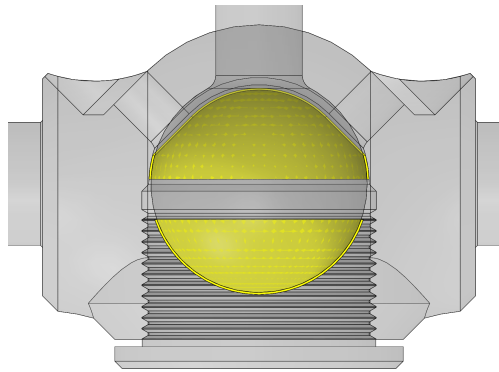


Figure 4.7: Application proposal of PTFE liner (yellow) on ball joint

The effect that the liner has on the total stiffness was investigated by simulating a simplified joint with and without the liner. The load was applied in the same way as presented above and bearing was simulated as rigid with the use of a MPC-Constraint, where the master point was only supported in the y-direction. The housing and ball was simulated with a 0.3mm and 0.5mm layer of PTFE with the same properties as the plain bearings presented earlier. Simulations were only carried out for tensile loads of the joint. The reference simulation of the joint without the liner, and with 0.3mm and 0.5mm thick liner is then presented in Figure 4.8. Again, the total force applied to the joint is 1000N. From this, the joint with the 0.3mm and 0.5mm layer deforms $0.372\mu\text{m}$ and $0.580\mu\text{m}$ more than the joint without. With the total joint stiffness of $221\text{N}/\mu\text{m}$, the layer of 0.3mm and 0.5mm reduces the stiffness by $\approx 10\%$ and $\approx 15\%$.

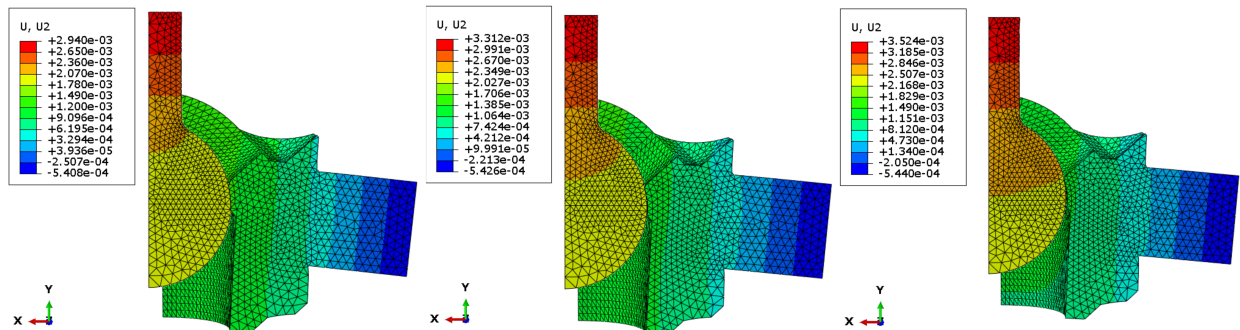


Figure 4.8: Deformation of simplified ball joint, W/o liner (L), W/ 0.3mm liner (M), W/ 0.5mm liner (R)

4.2 Cardan Joint

Because of the large number of parts in the Cardan joint, it was simplified down in to the two assemblies shown in Figure 4.9. This was separated at the spherical bearing since it does not transmit any bending forces (if friction is neglected). The first part of the assembly included the mounting bracket, centre hub and other connecting parts. This also included a dummy plate of aluminium, of which the mounting brackets were bolted to with a preload of 10kN. Friction between steel mating faces was defined with a friction coefficient of 0.4, and bearing friction was set to frictionless. In this simulation, the load was applied to the dummy platform, with the use of a MPC which was supported in all directions except y.

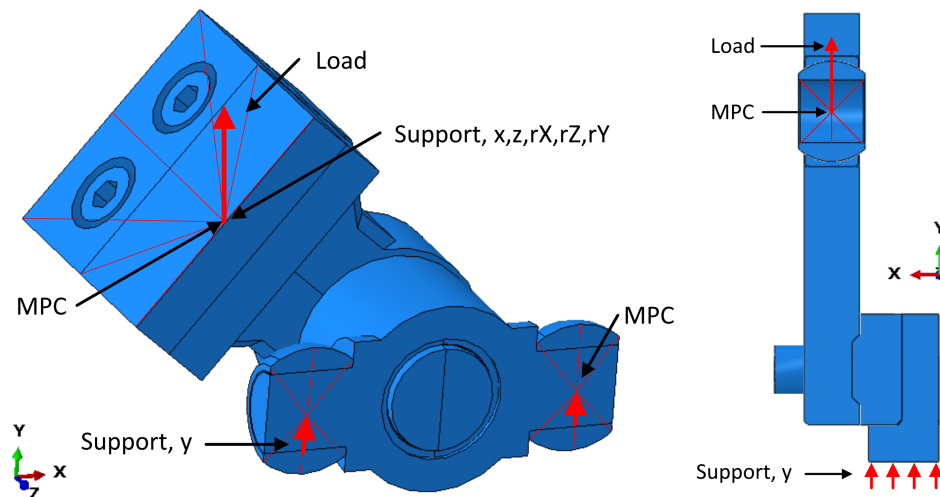


Figure 4.9: Cardan joint, simulation setup

The load on the joint is 1000N at an orientation of $(0^\circ, 0^\circ)$, $(0^\circ, 50^\circ)$ and $(50^\circ, 0^\circ)$ around axis (1,2). The preload also initially deforms the joint in the first simulation frame with $-1.847\mu\text{m}$, $+0.598\mu\text{m}$ and $-0.590\mu\text{m}$ in the direction of the applied load. Adding this to the total deformation in Figure 4.10 gives a deformation of $3.18\mu\text{m}$, $4.20\mu\text{m}$ and $4.88\mu\text{m}$ with the three load cases. Note that with the simulation of load angle $(50,0)$ in Figure 4.10 the boundary constraints are not the same as the other two, hence the reference point is on the spherical bearing ball.

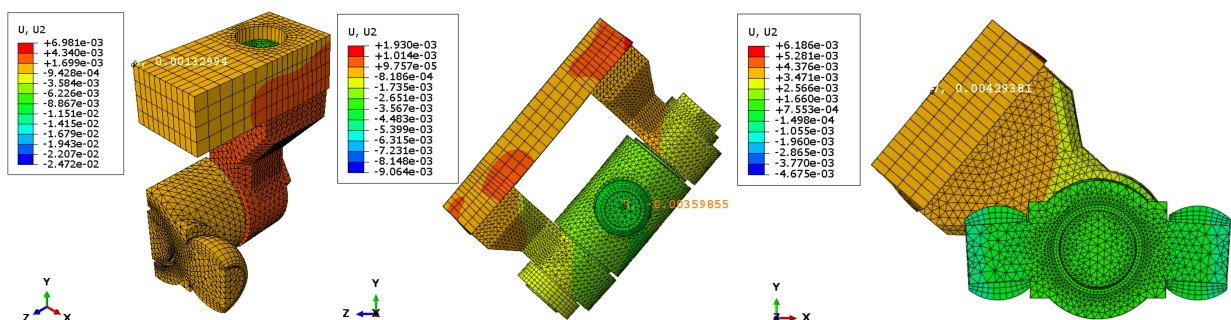


Figure 4.10: Deformation of simplified Cardan joint assembly, Load angle $(0,0)$ (L), Load angle $(50,0)$ (M), Load angle $(0,50)$ (R)

The second part of the assembly is then what makes up the yoke of the Cardan joint, which includes the side plates, spherical bearing, link and link adapter. With this, the load was applied to the inside of the spherical bearing ball with the use of an MPC-Constraint, and the face of the link was supported in the y-direction, as seen in Figure 4.9. Since the bolted connection is perpendicular to the direction of the applied load, it is a slip critical connection. To investigate the effect of this bolt connection, two model setups were simulated. The first simulation, presented in Figure 4.11, is with a tie connection, where the side plates and link adapter essentially is a solid part. The next two simulations included the bolts with a preload of 10kN and a friction coefficient of $\mu = 0.2$ and $\mu = 0.6$. The preload initially deforms the joint at the reference point by $0.316\mu m$ in the direction of the applied load. From this, it can be seen that the bolted connection deforms $1.71\mu m$ with $\mu = 0.2$ and $1.51\mu m$ with $\mu = 0.6$, while the joint with a tie connection deforms $1.30\mu m$.

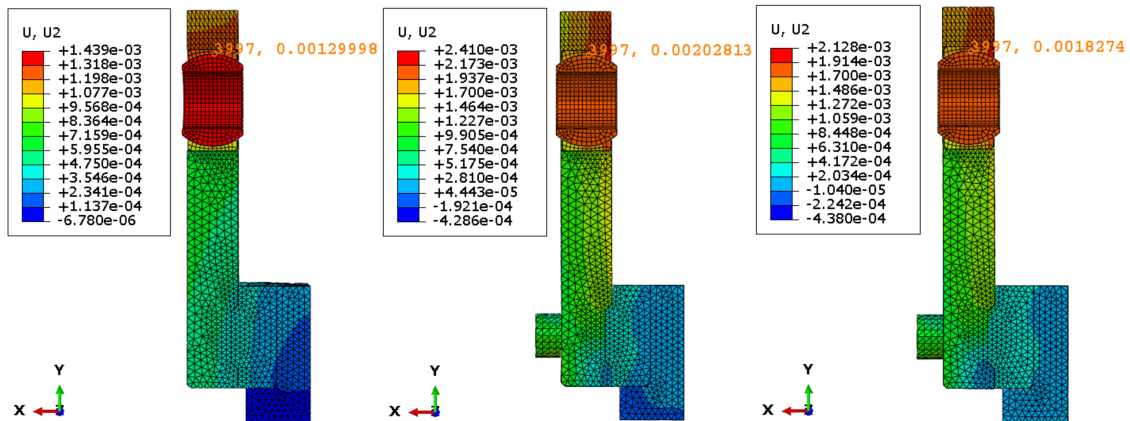


Figure 4.11: Deformation of Cardan joint yoke, with tie connection(L), $\mu = 0.2$ (M), $\mu = 0.6$ (R)

With these three load cases the stiffness of the Cardan joint is presented in Table 4.1.

Load angle [deg]	stiffness [$N/\mu m$]
(0,0)	204
(50,0)	169
(0,50)	152

Table 4.1: Cardan joint stiffness

5 Machine Design

Based on the state of the art study presented in Chapter 1 and the joint design presented in Chapter 3, the concept presented in Figure 5.1 was constructed. In this chapter, the process of incorporating the different components into the design, including the considerations that were made, is presented. The Gantry-Tau presented here is referred to as a machine, rather than a robot, where it refers to the assembled robot that makes up the milling machine.

First presented in this chapter is the machine requirements, which is then followed by the calculation of equivalent actuator requirements. Then the selection procedure of the telescopic link actuators and gantry drives is shown, where the expected force, speed and stiffness is calculated. The passive link selection is then presented, and lastly, the proposed tool platform design is shown.



Figure 5.1: Complete assembly of proposed design

5.1 Actuator Requirements

To properly size the drives for the application, the force and speed requirements were first formulated. Presented in this section is an approximation of the forces and speeds of the TCP in the metal machining application, which is then used to calculate the force and speed requirement imposed on the actuators.

The HSM application requirements presented in Section 1.1.1 is seen as requirements aimed at higher production rates than what this machine is intended for. While this is a task that suits a high-performance PKM very well, the requirements formulated below is closer to the regular machining tasks.

5.1.1 TCP Forces

The forces acting on the tool during the process of milling, is complicated and depends on many parameters. Most of these are determined by the specific work, such as radial and axial depth of cut, and the specific material, with different hardness and recommended cutting speeds. It was therefore seen to be more representative to consider some particular cases of milling work to be performed by the machine. For this, the process of slot milling with High Speed Steel (HSS) end mills was considered. Since many of the parameters are directly linked to the properties of the specific tool, it is seen as most accurate to use the calculators given by the vendor of the specific tool such as the online calculator on *Sandvik Coromant's* page, see [41]. Table 5.1 shows the recommended values for a 2 and 4-flute roughing end mill in the *CoroMill Plura* series [42][43], at different Depth of Cut (DOC). Presented here is the cutting speed, V_c , spindle speed, n , feed rate, V_f , and cutting power, P_c . The radial depth of cut is half of the tool diameter, D_{tool} and the material is aluminium and steel, assumed to have a hardness 90 HB and 175 HB.

Mill and material	D_{tool} [mm]	DOC [mm]	V_c [m/min]	n [rpm]	V_f [mm/min]	P_c [kW]	F_c [N]
HSS 2-flute [42], Alu.	6.35	10	725	36400	6530	3.18	262
	12.7	10	747	18700	6920	5.61	226
	12.7	15	732	18400	6780	8.25	674
HSS 2-flute [42], Steel	6.35	10	216	10800	901	2.27	632
	12.7	5	231	5780	935	1.89	492
HSS 4-flute [43], Alu.	6.35	10	773	38700	16900	4.14	322
	12.7	5	708	17100	11900	4.87	428
HSS 4-flute [43], Steel	6.35	10	299	15000	6040	1.59	318

Table 5.1: Recommended parameters and requirement for slot milling with HSS end mill in aluminium and steel

If only a single cutter is engaged at any time, the cutting force, F_c , can be calculated from equation 5.1, where, P_c , is the cutting power in *Watt*, D_{tool} is the effective cutting diameter of the tool in mm, and n is the rotational speed of the spindle, in rpm.

$$F_c = \frac{P_c}{n \frac{\pi}{30}} \frac{2}{D_{tool} 10^{-3}} \quad (5.1)$$

While this gives a good idea of the loads inflicted on the machine with different work types and workloads, it must be noted that the spindle performance is also a factor. Skipping ahead to section 5.6.1, the spindle that was selected as a reference, has a torque rating of 4.1Nm continuous and 5.4Nm intermittent. The maximum cutting force that this spindle is capable of maintaining is then a function of the tool cutting diameter with the relationship presented in Figure 5.2. While this tends to infinity as the tool diameter, D_{tool} , tends to zero, the load that the end mill can take without breaking tends to zero as the diameter does. It is therefore seen as realistic to limit this to a maximum of $F_c = 900N$.

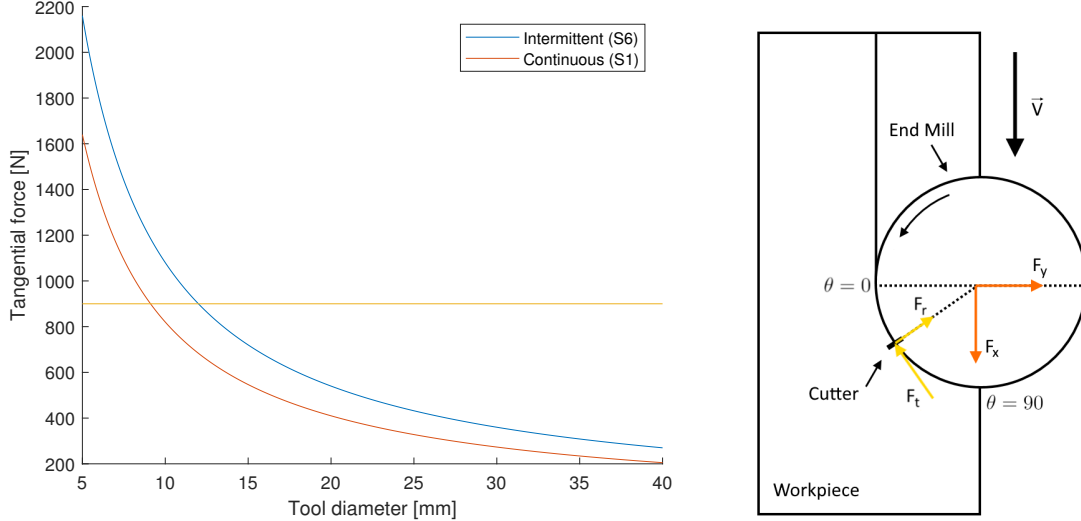


Figure 5.2: Max cutting force of spindle versus tool diameter (L), Cutting force components (R)

The force calculated from the above equation is the total effective tangential force acting on the tool. In reality this is not constant, where it depends on many factors, but mainly varies with chip thickness, h . The chip thickness can be related to the instantaneous angle of the tool, θ , by $h(\theta) = f \sin(\theta)$ [44], where f is the feed pr. tooth. The tangential force component can then be related to the chip thickness by Equation 5.2, where $F_{C,max}$ is here assumed to be equal to the cutting force F_c

$$F_t = F_{c,max} \sin(\theta) \quad (5.2)$$

There is also a radial force component, F_r , which acts perpendicular to this tangential force component, F_t , as seen in Figure 5.2, which is the case of up-milling. This force component depends on the geometry of the tool, but it is seen as a good approximation that it is no more than $F_r = 0.5 F_t$ [44]. Combining these force vectors, the reaction force components F_x and F_y can then be represented by equation 5.3 and equation 5.4.

$$F_x = F_t \sin(\theta) + F_r \cos(\theta) \quad (5.3)$$

$$F_y = -F_t \cos(\theta) + F_r \sin(\theta) \quad (5.4)$$

From this relationship, it can be seen that the resultant force vector, $F_R = \sqrt{F_x^2 + F_y^2}$, is maximum when $\theta = 90$, which gives $F_{R,max} \approx 1.12F_{C,max}$. With $F_c = 900N$, the total force vector is then $F_R \approx 1000N$. There are also thrust forces which act along the length of the tool. The magnitude of this depends on many factors, but it is observed that it corresponds well with $F_a = 0.2 F_R = 200N$ [44].

5.1.2 TCP Speeds

From the recommended feed speeds, V_f , in Table 5.1, it is seen that aluminium gives the highest requirements of up to $16.9m/min$ ($0.28m/s$). Based on this, and by studying other PKM machining centres, the maximum feed speed requirement was determined to be $30m/min$ ($0.5m/s$).

Another aspect of 5-axis machining is the ability to rotate the head such that the tool can follow the contours of the workpiece surface (machined surface), which is desirable when using tools such as ball end mills. It is therefore also important that the robot can rotate the tool quickly enough to follow the contours of the work. These limits are not as straightforward since these are very much related to the geometry of the work. Through studying other PKM machining centres, such as those presented in Appendix B, a maximum of $1.5rad/s$ was determined. With this, and the other statements above, the final requirement for the machine is summarised in Table 5.2.

Description	min	unit
Resultant force (x-z plane)	1000	N
Axial force (y direction)	200	N
Feed rate	0.5	m/s
Tool rotation speed	1.5	rad/s

Table 5.2: Machine requirements

5.1.3 TCP to Actuator Force

These requirements are in relation to the TCP in global Cartesian coordinates of the tool, and must therefore be converted to the equivalent force transmitted through the drives of the machine. This relationship can be described with different methods, but in this section, the process of using the inverse robot jacobian as well as the static matrix is presented.

With the principle of conservation of energy, assuming no energy loss, the relationship of equation 5.5 must be true. The right side of the equation is the energy put into the system, described by the actuator velocity, \dot{q} , and force, F . The left hand is the corresponding output of the system, which is defined by the TCP velocity, \dot{X} , and the wrench, \mathcal{T} .

$$\dot{X}^T \mathcal{T} = \dot{q}^T F \quad (5.5)$$

With use of the Jacobian matrix, the relationship between the drive and TCP velocity is described by equation 5.6 [23], where J_x is the direct robot Jacobian, and J_q is the inverse robot Jacobian.

$$\dot{X} = J_x \dot{q} = J_q^{-1} \dot{q} \quad (5.6)$$

Equation 5.7 is then obtained by combining equation 5.6 and equation 5.5 and utilising the matrix relationship $(A \cdot B)^T = B^T \cdot A^T$.

$$F = J_x^T \mathcal{T} = J_q^{-T} \mathcal{T} \quad (5.7)$$

One limitation of this method is that it does not consider torque applied to the TCP around the y-axis. This is because the Jacobian is a 5x5 matrix, as it was derived with consideration of the redundant angle r_Y as a known independent variable. To accommodate this torque, the static matrix, presented later in section 6.1, can be used instead. Shown here, in equation 6.6, is the relationship between the link jacobian, J_L , and the static matrix, H . From this, the relationship between the wrench, \mathcal{T} , and link forces, F_L , can be described by equation 5.8.

$$F_L = H^{-1} \mathcal{T} \quad (5.8)$$

Since this is equivalent to using the link Jacobian, the force vector, F_L , is the link reaction forces. The force in each gantry drive q_1 , q_2 and q_3 can then be calculated from the sum of forces acting in the x-direction in the links connected to it. The force in the telescopic link actuator drives q_4 and q_5 , is then just the force acting in the corresponding link. This torque load mostly affects the links of the three link cluster, and it must be noted that the added forces due to the maximum torque of $5.4Nm$, with the selected spindle, makes little effect compared to the total forces on the TCP.

Since the forces applied to the TCP during 5-axis milling follows the rotation of the tool, the force vector was rotated correspondingly. This was obtained by the rotation matrix presented in equation 2.4, where the tool rotation is described by equation 5.9. For consistency, since the tool rotation r_y varies with TCP position, the force vector was not rotated with r_y , hence $r_y = 0$.

$$\begin{aligned} F_{TCP} &= R(r_x, r_z, 0) \begin{bmatrix} F_x & F_y & F_z \end{bmatrix}' \\ M_{TCP} &= R(r_x, r_z, 0) \begin{bmatrix} M_x & M_y & M_z \end{bmatrix}' \end{aligned} \quad (5.9)$$

$$\mathcal{T} = \begin{bmatrix} F_{TCP} \\ M_{TCP} \end{bmatrix} \quad (5.10)$$

The combined weight of the tool platform, spindle and the joints connected to the platform, seen in Section 5.6, is 44kg, which is not inconsiderable compared to the force generated from the milling operation. To account for the weight of an end mill, the links and other unknown factors, the force due to gravity, G , was defined as $G = 600N$.

Directly applying this to the TCP does, however, introduce some errors, as it results in a moment load on the tool platform which depends on the length of the tool. This was therefore cancelled out by applying an equal but opposite moment on the TCP, with the magnitude calculated by equation 5.11. L_G is the moment arm vector between the centre of gravity, COG , to the TCP, which can be calculated from equation 5.12. Since the robot is intended to be arranged with the tool facing downward, the direction of this force is in the positive y-direction, hence the unity vector $[0, 1, 0]^T$.

$$M_G = L_G G \quad (5.11)$$

$$L_G = \left(Rot(rX, rZ, 0) \begin{bmatrix} COG \end{bmatrix} \right) \times \begin{bmatrix} 0 \\ 1 \\ 0 \end{bmatrix} \quad (5.12)$$

If the spindle, platform and joints are considered, the centre of gravity in relation to the TCP is $COG = [-0.012, -0.120 - L_{tool}, -0.026]^T$. The wrench, \mathcal{T} , including the weight, is then calculated from equation 5.13.

$$\mathcal{T} = \begin{bmatrix} F_{TCP} \\ M_{TCP} \end{bmatrix} + \begin{bmatrix} G \\ -M_G \end{bmatrix} \quad (5.13)$$

5.1.4 TCP to Actuator Speed

With the inverse robot jacobian, the speed of the actuators can be related to the speed of the TCP with equation 5.14 [23]. Since the Jacobian was derived with r_y as an independent variable, the velocity vector of the TCP is a 5x1 vector. This contains velocity in x, y and z as well as rotational velocity around x and z. In this case, the lack of input to the rotation around y-axis is not a problem since it is not directly controllable anyway.

$$\dot{q} = J_q \dot{X} \quad (5.14)$$

It was also interesting to investigate how the relationship of TCP speed and the speed of the drives changed with rotation of the tool with 5-axis motion. The largest movement is then expected to be along the surface of the workpiece, perpendicular to the tool, and therefore the speed vector is expected to rotate with the tool correspondingly. The speed vector \dot{X} was then rotated by the same method used with the force vector in equation 5.9.

5.1.5 Summary

With the requirements in Table 5.2 and the methods presented above, eight load cases were considered in both 3-axis and 5-axis motion with tool rotation up to $\pm 25^\circ$. The first three were with a force of $1000N$ and velocity of $0.33m/s$ in only x or z-direction, and at an angle of 45 degrees with the x/z-axis, all with thrust force of $200N$ in the negative y-direction. Since the thrust force is in the opposite direction of gravity with 3-axis motion, the above three cases were also considered with no thrust force. The last two were with a rotational velocity of $1.5rad/s$ around the x and z-axis. The maximum actuator values found with these load cases are presented in Table 5.3. These are presented as the maximum values found within the whole 5-axis workspace and within the 75% and 50% centre of the workspace.

	Workspace	q_1	q_2	q_3	q_4	q_5	Unit
Force	100%	2254	2215	2091	3195	3985	[N]
	75%	2254	2184	2006	2562	3984	[N]
	50%	2254	2144	1908	2062	3973	[N]
Velocity	100%	1.80	2.18	2.65	0.40	0.42	[m/s]
	75%	1.22	1.20	1.38	0.38	0.38	[m/s]
	50%	1.16	0.95	0.97	0.36	0.36	[m/s]

Table 5.3: Actuator force and velocity requirement

5.2 Link Actuator

From the study presented in Section 1.2, the screw actuator was considered to be the best solution. While the performance of these are heavily dependant on actuation length, it was seen not to pose as large of a limitation with the short stroke length. The current solutions use this type of actuator, but the performance of the specific actuator was not adequate for the goal of the machine. The solid nut screw actuator was ruled out due to its high mechanical losses and therefore evaluated in this section is a solution using recirculating ball screws and planetary roller screws.

With the values presented in Table 5.3, the following requirement was formulated for the screw actuator. The solution must be able to deliver a feed force above $4000N$ and must be able to reach a speed of 0.45 m/s or higher. The required stroke length for 25-degree tool rotation was calculated from the inverse kinematics to be $< 230mm$ for both of the link actuators. The stroke length of commercial actuators are typically available with increments of $50mm$, and therefore a stroke length of $250mm$ was chosen.

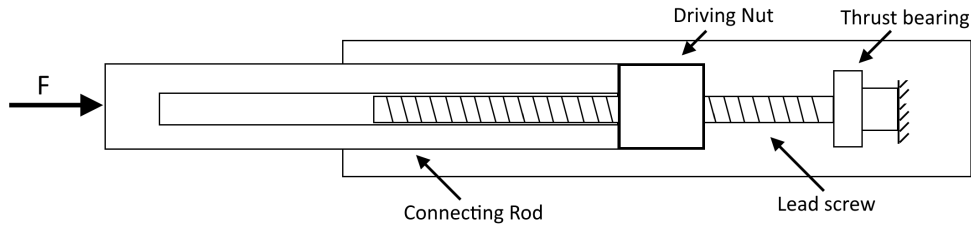


Figure 5.3: Main components of the linear actuator

5.2.1 Stiffness

While a stiffer screw and nut interface will undoubtedly increase the stiffness of the system, it is not the only factor of which determines the stiffness of the complete actuator Assembly. While a modern actuator consists of many parts, it can be simplified down to the key components presented in Figure 5.3. Since all of these components are connected in series, the total stiffness of the actuator can be approximated from equation 5.15.

$$K_{tot} = f_{mnt} \left(\frac{1}{K_{nut}} + \frac{1}{K_{brg}} + \frac{1}{K_{screw}} + \frac{1}{K_{rod}} \right)^{-1} \quad (5.15)$$

The first parameter, f_{mnt} , is a design parameter of $f_{mnt} = 0.8$, which was included to account for the unknown stiffness of components such as mounting brackets and a frame. The stiffness of the nut, K_{nut} , and support bearing, K_{brg} , for various screw dimensions was obtained from *Bosch Rexroth's* own catalogue [9], and is presented in Table 5.4. While, ideally, the screw should be supported at both ends, it is not practically feasible due to the geometry of the actuators. Therefore the screw is only supported by one bearing.

The stiffness of the lead screw, K_{screw} , also depends on the stroke length of the actuator, S , where it can be represented by equation 5.16. This can be calculated from the effective area of the screw, or by the stiffness factor, R_s , which is also given in the catalogue [9]. Due to clearances, the actual screw length under load is longer than the stroke length of $250mm$, where it assumed to be an additional $S_0 = 100mm$.

$$K_{screw} = R_s \frac{1}{(S + S_0)} \quad (5.16)$$

The stiffness of the connection rod, K_{rod} , is related to the construction of the actuator itself. The inside diameter of this must be larger than the outside diameter of the screw with some clearance, where it is assumed to be, $d_{i,rod} = d_0 + 5mm$. The outer diameter of the rod is commonly seen to be around 50% larger than this diameter. This rod must also be longer than the stroke length to provide clearance, but also to accommodate space for a mounting bracket. This length is assumed to be around 200mm longer than the maximum stroke length. The stiffness of the connection rod can then be calculated from equation 5.17. The rod is most commonly constructed of steel and it is therefore assumed to have Young's modulus $E = 210GPa$.

$$K_{rod} = \frac{\pi}{4} ((1.5 d_{i,rod})^2 - d_{i,rod}^2) \frac{E}{450} \quad (5.17)$$

5.2.2 Speed

The linear speed of the actuator, V_x , is related to the rotational speed of the screw, n_{screw} , and the lead, P_{screw} , by equation 5.18 [9]. With n_{screw} in *rpm* and P_{screw} in *mm*, V_x is in *m/s*. The maximum linear speed of the actuator is therefore limited by the maximum rotational speed of the screw, which in turn can be limited by different components.

$$V_x = \frac{P_{screw} n_{screw}}{60000} \quad (5.18)$$

One limitation is the resonance frequency of the screw itself, where the rotational speed is limited by the critical speed calculated from equation 5.19 [9]. The coefficient f_{ncr} is 4.3 with a single bearing support and the critical length, l_{cr} , is equal to the stroke length of 250mm plus the estimated 100mm for clearances. An additional factor of 0.8 is included, as it is recommended not to exceed 80% of the critical speed. With the smallest screw size in Table 5.4 this is above 6700rpm, which gives a linear speed of 0.56*m/s* and 1.12*m/s* with a lead of 5 and 10 *mm*.

$$n_{cr} = \frac{0.8 f_{ncr} d_2}{l_{cr}^2} 10^7 \quad (5.19)$$

Other limitations can then be posed by the thrust bearing or the nut itself. Thrust bearings such as the *FEC-F* bearing range from 6900rpm to 2800rpm in permissible speed with screw size 20mm to 40mm [9]. The last component, the nut itself, varies significantly with the type of nut, but it is seen to range from 2300 rpm to 6000 rpm with ball screws and 2500 to 6000 rpm with planetary roller screws [9]. Limitations can also be posed by the motor, where if a reducer is used between the motor and screw, the speed requirement of the motor increases.

5.2.3 Force

The feed force of the actuator can be related to the motor torque by equation 5.20 [45]. i is an optional gear ratio between the motor and the screw and η is the efficiency of the screw, which is assumed to be 0.98 for ball screws and 0.9 for planetary roller screws [9].

$$F_x = 2000\pi M_m \eta \frac{i}{P_{screw}} \quad (5.20)$$

Since the design is stiffness driven, the components are generally used well below their rated limits. This is also the case for the screw and nut, where all the screw types listed in Table 5.4 has a dynamic load rating well above the requirement in Table 5.3.

5.2.4 Summary

Presented in Table 5.4 is the approximated stiffness of actuators with different screw size and lead, with ball and roller screw nuts. While the larger screw sizes in this table will give the highest stiffness, the size and weight of commercial actuators that use these are considerable. It is also seen that the ball screw assemblies take up less space than the planetary roller screws. This commonly allows for one size larger screw for a given frame size with actuators such as the *EMC-HD* from *Bosch Rexroth* [46]. The frame of these is constructed of steel which means these are stiff but also heavy. With the smallest size, *085*, these weigh 38kg, not including the motor. While not as stiff, the aluminium housed actuators in the *EMC* series were therefore considered instead.

Nut type	$d_0 \times P$ [mm]	K_{nut}	K_{brg}	$K_{screw} (S_0/S_{250})$	K_{rod}	$K_{tot} (S_0/S_{250})$
Ball screw	25x5	360	450	246/860	286	83/64
	25x10	370	450	246/860	286	84/64
	32x5	440	600	411/1440	469	118/94
	32x10	580	600	403/1410	469	128/100
	40x5	660	750	663/2320	733	172/140
	40x10	580	750	603/2110	733	163/132
Roller screw	25x5	460	450	294/1030	286	90/71
	25x10	290	450	294/1030	286	79/64
	30x5	620	600	426/1490	412	125/99
	30x10	420	600	426/1490	412	112/91
	39x5	750	750	717/2510	697	178/146
	39x10	500	750	717/2510	697	155/130

Table 5.4: Approximated stiffness of ball and roller screw actuators, [$N/\mu m$] [9]

Another limitation of the actuator is the dimension of the frame. For the actuator to not collide with link E, and limit the workspace, the frame must fit within a cylindrical envelope of $< 120mm$. The largest actuator that fits is then the *EMC-63* [45] which uses a 25mm ball screw. This is then suggested to be paired with the *MSK050C-0450* [47] motor and a reduction of $i = 2$. This gives a feed force of $F_0 = 6158N$ at zero speed, which gives an overhead of 53% with the above-mentioned requirement. The components of the actuator can reach a speed of $0.55m/s$, but in this case the motor is limited to 6000rpm and therefore the linear speed is limited to $0.5m/s$. The performance of this combination is summarised in Table 5.5.

$d_0 \times P$ [mm]	F_0 [N]	V_{max} [m/s]	W [kg]	K_x [$N/\mu m$]
25x10	6158	0.50	15.8	64

Table 5.5: Bosch Rexroth EMC-63 with MSK050C-0450, [45] [47]

5.3 Gantry actuator

From the study presented in section 1.2 the rack and pinion drive were considered to be the best option for the machine. It was also mentioned in [48], that within the *EU FP-6 project SMErobotTM*, regarding low cost and high stiffness, the Gantry-Tau design based on the rack and pinion drive was determined to be the optimal design. The dual drive solution was then regarded as the best method for eliminating backlash, as it poses the least significant drawbacks of the three.

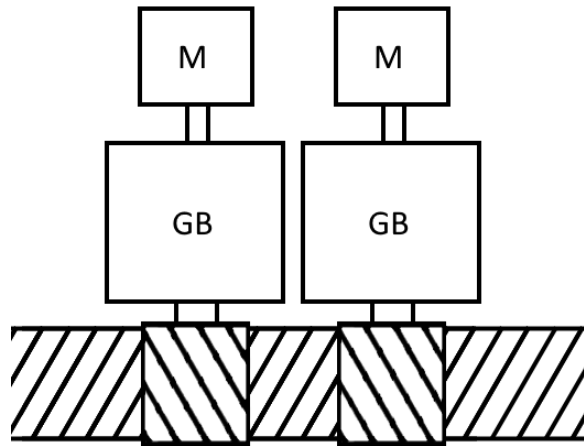


Figure 5.4: Dual drive rack and pinion solution

Various control schemes can be implemented to control the dual drive, where it is seen in [48] that the complexity ranges from constant torque control to a non-linear switching controller. The topic of control is not addressed in this report, but the last of these control schemes is assumed to be implemented in the future, since it allows for tandem drive.

With the values presented in Table 5.3, the following requirement was formulated for the rack and pinion drive. The solution must be able to deliver a feed force above 2300N and must be able to reach speeds higher than 1.4 m/s. While the required velocity of the drive is higher at the edges of the workspace, the speed requirement within the middle 75% of the workspace was considered to be more realistic.

5.3.1 Backlash

There are two sources of backlash in this drive system, one which originates from the gearbox and one in the rack and pinion mesh itself. The linear backlash, j_x , of the system, from the torsional backlash of the gearbox, j_θ , depends on the pinion pitch diameter, D_p , and can be represented by equation 5.22. Where Z is the number of teeth in the pinion, m_n is the normal module, and β is the helical angle of the gear. With j_θ in radians j_x is μm of linear backlash.

$$D_p = \frac{Z m_n}{\cos(\beta)} \quad (5.21)$$

$$j_x = j_\theta \frac{D_p}{2} 10^3 \quad (5.22)$$

From this, it is clear that the effect of the gearbox backlash is proportional to the pitch diameter of the pinion. This is especially important for split pinion drives, where this is more or less the only source of backlash in the system.

5.3.2 Stiffness

The stiffness of the rack and pinion drive can then be approximated with the same approach as the link actuators, where the total linear stiffness, K_x , can be calculated from its main components with equation 5.23.

$$K_x = \left(\frac{1}{K_{x,gb}} + \frac{1}{K_{msh}} + \frac{1}{K_{x,tan}} + \frac{1}{K_{x,rad}} \right)^{-1} \quad (5.23)$$

The first parameter $K_{x,gb}$ is the equivalent linear stiffness calculated from the torsional rigidity of the gearbox. This depends on the pitch diameter of the pinion, D_p , where it can be represented by equation 5.24. From this, it is clear that the linear stiffness, only considering the gearbox, is inversely proportional to the square of the pitch diameter of the pinion. With the size 4 gearbox (PH4) from *Stöber* [49] and a 12 tooth module 2 pinion, the equivalent linear stiffness is $700 N/\mu m$. If then a 16 tooth pinion is used instead, this drops down to $394 N/\mu m$.

$$K_{x,gb} = \frac{K_\theta}{(D_p/2)^2} \quad (5.24)$$

Another parameter, is the mesh stiffness, K_{msh} , between the rack and the pinion. The mesh stiffness of a gear pair depends on many factors, such as tooth form, gear quality and more. It is also not a constant value where it varies with the angular position of the gear in mesh [50]. The average mesh stiffness can, however, be approximated as constant with the values presented in *ISO-6336*. It is then defined as a stiffness per unit width of the gear, where it is $18.7 N/um mm$ for helical gears with 20° helix and $20 N/um mm$ for spur gears, both with 20° pressure angle. With a normal module of $m_n = 2$, the rack is typically 24mm wide, which gives a mesh stiffness of $449 N/um$ with helical cut gear. If a split pinion design were to be used, it is important to notice that the width of the gear is less than half of the rack width, and in turn, this stiffness is halved.

With most rack and pinion solutions, the pinion is only supported from one side, and the tilting stiffness of the gearbox affects the total linear stiffness. This can be divided into tangential stiffness, $K_{x,tan}$, related to the feed force acting on the pinion along the direction of travel and radial stiffness, $K_{x,rad}$, related to the radial forces in the gear mesh, which pushes the pinion out of mesh. Both of these are determined from internal parameters of the gearbox, and can be approximated from equation 5.25 and equation 5.26, which was obtained from the catalogues of *Wittenstein* [51]. C_{2K} is the tilting rigidity of the gearbox in $Nm/arcmin$ and L_b is the distance, in mm , from the centre of the pinion to the effective load centre of the rearmost angular contact bearing. α is the pressure angle, which is 20° , and β is the helix angle of 19.5283° .

$$K_{x,tan} = 180 \frac{60 C_{2K}}{\pi L_b^2} \quad (5.25)$$

$$K_{x,rad} = 180 \frac{60 C_{2K}}{\pi (L_b \tan^2(\alpha))(L_b + \frac{\tan(\beta) d}{\tan(\alpha) 2})} \quad (5.26)$$

The tilting stiffness of the PH4 gearbox is $160N/arcmin$, but the length L_b found at [52] does not fully correspond with their published total linear stiffness. Instead, a length $L_b = 56mm$ was found to correspond, which gives a tangential component $K_{x,tan} = 175N/\mu m$ and a radial component $K_{x,rad} = 1084N/\mu m$.

To improve the tilting rigidity, a solution is to support the pinion from both sides, which is the case for the ZTRS line from *Atlanta drives/Stöbel*. This includes an additional bracket that houses a bearing which supports the opposite side of the pinion. From their published values, this is seen to increase the total linear stiffness by approximately 50% with their size-7 gearboxes.

5.3.3 Speed

The maximum speed of the rack and pinion system is limited by the allowable input speed of the gearbox, n_m . The maximum linear speed of the drive can be calculated from equation 5.27, where it is a function of both the gear ratio, i , and the pinion pitch diameter, D_p . From this, it is clear that, while a smaller pinion has the benefit of decreased backlash and increased stiffness it also reduces the attainable speed of the drive.

$$V = \frac{2\pi}{60} n_m \frac{i}{D_p/2} \quad (5.27)$$

5.3.4 Force and Acceleration

The linear force of the drive is related to the output torque of the motor, M_m , the gear ratio, i , and the pinion pitch diameter, D_p , with equation 5.28. The efficiency of the *PH* gearboxes from *Stöber*, is $\leq 96\%$ [49], but there are additional losses between the pinion and rack mesh as well as between the linear bearings and rails. A total efficiency, η , of the gantry drive system is therefore assumed to be $\eta \geq 85\%$.

$$F_x = \eta M_m \frac{i}{D_p/2} \quad (5.28)$$

The inertia that this force needs to accelerate is not only determined by the mass of the carriage, M_{cr} , but also the motor inertia, J_m , and gearbox inertia, J_{gb} . By the principle of conservation of energy, assuming rigid couplings, the effective mass inertia of the system, M_{eq} , can be related through it's kinetic energy by equation 5.29. The effective mass inertia considering both drives, $M_{eq,2x}$, was then calculated by equation 5.30. i is the gear ratio of the gearbox and $M_{m,gb}$ is the combined weight of two motor and gearboxes. The mass of the carriage, M_{cr} , not including motor and gearbox, is $M_{cr} \approx 35kg$.

$$\frac{1}{2}M_{eq} \dot{x}^2 = \frac{1}{2}(M_{cr} + M_{m,gb}) \dot{x}^2 + (2J_m + 2J_{gb}) \left(\frac{i}{D_p/2} \dot{x} \right)^2 \quad (5.29)$$

$$M_{eq,x1} = M_{cr} + (2J_m + 2J_{gb}) \left(\frac{i}{D_p/2} \right)^2 \quad (5.30)$$

The maximum acceleration of the carriages can then be calculated from equation 5.31. Taking advantage of the dual drive, the feed force is, in this case, $F_{x,2x} = 2 F_x$.

$$a_{max} = \frac{F_{x,2x}}{M_{eq}} \quad (5.31)$$

5.3.5 Natural Frequency

To not affect the control system, the natural frequency of the carriage system should be much greater than the frequency of which the drives operate. Assuming a simplified one-dimensional spring-mass system, the natural frequency can be calculated from equation 5.32. In this case, only one drive was considered, and therefore the effective mass inertia, $M_{eq,x1}$ was calculated from equation 5.33.

$$W_n = \sqrt{\frac{K_x}{M_{eq}}} \quad (5.32)$$

$$M_{eq,x1} = M_{cr} + (J_m + J_{gb}) \left(\frac{i}{D_p/2} \right)^2 \quad (5.33)$$

5.3.6 Summary

Shown in Table 5.6 is the performance values for different size gearboxes with a gear ratio, $i = 5$ and different pinion teeth numbers, Z , with normal module, $m_n = 2mm$. Shown here is the weight of the gearbox, W_{gb} , the linear backlash from the gearbox, Δs , maximum attainable speed, V_{max} , linear force to motor torque ratio, and finally the total linear stiffness, K_x , obtained from [53].

Description	Z [-]	W_{gb} [kg]	Δs [μm]	V_{max} [m/s]	$Nm/1000N$ [Nm]	K_x [N/ μm]
ZTR-PH4	12	3.9	11	1.60	2.55	97
	16	3.9	15	2.13	3.40	91
ZTR-PH5	12	6.6	11	1.47	2.55	94
	19	6.6	15	2.31	4.03	92
	23	6.6	21	2.81	4.88	88
ZTR-PH7	12	12.3	11	1.33	2.55	116
	23	12.3	21	2.56	4.88	115
ZTRS-PH7	23	>12.3	21	2.56	4.88	175

Table 5.6: Properties of rack and pinion drive system sizes [49] [53]

Based on the above, the *PH4* gearbox was selected with a 12 teeth pinion. To select a suitable motor and gear ratio for this combination, the force, speed, acceleration and natural frequency were calculated from the different combinations. Presented in Figure 5.7 is the calculated performance with the *EZ402U* and *EZ404U* motor [54] and a gear ratio of 4,5,7 and 10.

Motor [54]	i [-]	F_{x2} [N]	V_{cont}/V_{max} [m/s]	K_x [N/ μm]	$M_{eq,2x}$ [kg]	$M_{eq,1x}$ [kg]	a_{max} [m/s ²]	W_n [Hz]
EZ402U	5	2337	0.72/1.60	97	140	97	17	159
	7	3271	0.61/1.14	96	205	129	16	137
	10	4673	0.47/0.80	90	354	204	13	106
EZ404U	4	3098	0.77/1.67	97	144	100	22	156
	5	3872	0.72/1.60	97	186	122	21	142
	7	5421	0.61/1.14	96	291	174	19	118

Table 5.7: Motor and gear combinations, [53]

From this, the *EZ404U* motor and a gear ratio of 5 was chosen. This is then suggested to be paired with a *SI6A161* motor driver [54]. This combination can deliver a total linear force of 3872N which allows for an overhead of 68% over the above-mentioned requirement. The maximum speed of the drives is also above the requirement with a margin of 14%.

F_{x2} [N]	V_{cont}/V_{max} [m/s]	a_{max} [m/s ²]	W_m/W_{gb} [kg]	K_x [N/ μm]
3872	0.72/1.60	21	7.2/3.9	97

Table 5.8: ZTR212S PH421F0040 with EZ404U [53] [54]

5.4 Gantry Carriage

For external support of the rack and pinion system, the carriage solution presented in Figure 5.5. This is guided by four linear roller bearings on profiled rails, which was selected because of the higher stiffness compared to the ball bearing systems while it maintains a low friction interface. It is generally desirable for these to be as rigid as possible, but the weight is also a limiting factor. The size-35 linear roller bearings with standard length (FNS) was considered to be the best option, which weighs 1.7kg each (6.8kg tot) [29]. These are available in different classes of preload, where a higher preload increases the stiffness of the bearing, but at the cost of friction and service time. Rigidity is the primary concern and therefore the highest preload, class C3, was chosen, which has a preload of 13% of the dynamic load capacity. The stiffness is then $\approx 1300N/\mu m$, $\approx 1100N/\mu m$, and $\approx 800N/\mu m$ with a push, pull and a side load of 10kN.

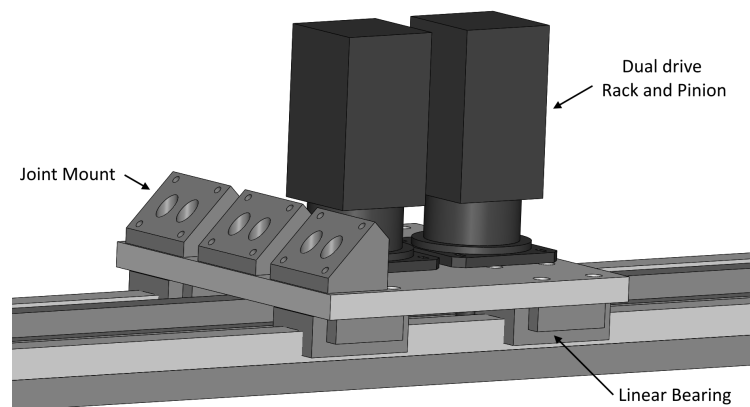


Figure 5.5: Gantry carriage

It is also shown in Section 2.5, that the joints mounted to the carriages should be installed at an angle of 45° relative to the surface of the carriage, such that the mobility requirement of the joint is minimised. Therefore the joints are proposed to be mounted with the bracket shown in Figure 5.5.

5.5 Passive Link

As it was mentioned in [1], the stiffness of the passive links could be increased without increasing the weight by using carbon fibre rods/tubes. There are many different ways of constructing these where the most common methods are braiding (BRD), filament winding (FW) and pultrusion. For simple profiles such as rods, the process of pultrusion can be used, which is the most cost-effective of the three. As a consequence of the production, rods produced by this method has all the fibres arranged along the length of the rod, which means that it has great tensile and compressive characteristics. While, it has poor torsional and bending characteristics compared to the other production methods, it is not as great of a concern since the links are ideally only loaded with tensile and compressive forces.

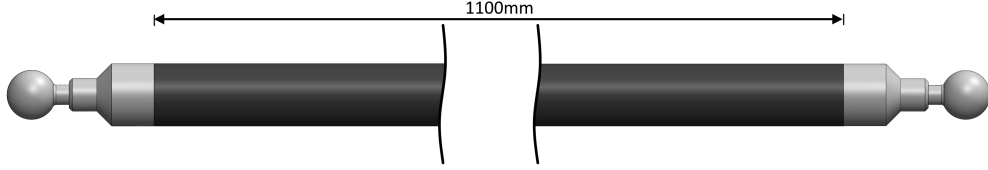


Figure 5.6: Passive link assembly, rod length

Another benefit of using carbon fibre reinforced epoxy is that it has a low coefficient of thermal expansion (CTE). This means that the dimensions of the links, and in turn the relative position of the TCP, is less affected by temperature fluctuations. While the environment temperature is relatively constant, the drives and the spindle will generate heat, which will, to some extent, be conducted through the joints and the links. The CTE of carbon fibre composites varies for the different production methods and different fibre volume fractions, but mostly with the direction of the fibres. The longitudinal CTE of pultruded carbon fibre is generally observed to be lower than $2\mu m/(mK)$ [55], around one-tenth of aluminium, which gives an expansion of $40\mu m$ at 20-degree temperature fluctuation.

To minimise the chance of link collision, it is desirable to maintain a high stiffness while minimising the outer diameter of the links. Therefore, a solid rod profile is preferred over the hollow tube section used on the current prototype. Pultruded carbon composite rods are available with a diameter, D , up to 38.1mm from *Rock West Composites*, [56]. The stiffness of these can then be calculated from equation 5.34. E is the longitudinal Young's modulus, where high modulus carbon fibre (HMCF), such as [57], have a compressive modulus of $228GPa$ and a tensile modulus of $197GPa$. With a length, L of 1100mm, the compressive stiffness is $236N/\mu m$ and tensile stiffness is $204N/\mu m$.

$$K_{rod} = \frac{E \frac{\pi}{4} D^2}{L} \quad (5.34)$$

5.6 Tool Platform

The tool platform design of PKM's is something that has not seen as much attention as other components have, but the stiffness of this is something that can not be overlooked, as it will compromise the rigidity of the robot if it is not adequate. The current solution to the tool platform is presented in Figure 5.10, which is light, at ≈ 6.5 kg, but has poor stiffness, as it is seen in the next chapter, which makes it inapplicable to the milling application. The most apparent weakness is the single side supported pins that the joints are mounted to. The second is it's poor resistance to both torsional and bending moments, which is an effect of the sandwich based design where six bolted pins support the three layers of the frame, see [1].

Even with simple load conditions, such as loads in pure x, y or z-direction, the load imposed on the tool platform by the links becomes very complicated. An example of a load in these three directions is presented in Figure 5.7, which is the visualised deformation of the tool platform with exaggerated scaling.

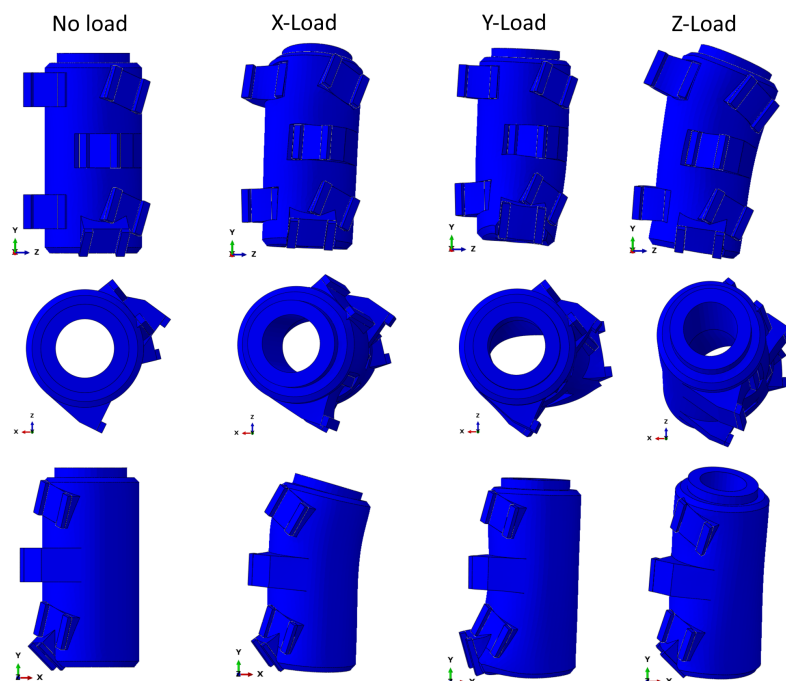


Figure 5.7: Tool platform load cases

The general shape of the tool platform was chosen as a tubular form. This was first of all selected because of the circular shape of the spindle, which makes it easier to obtain a weight efficient design. But also, the cylinder shape handles the wide variety of load conditions very well. The final design of the tool platform is presented in Figure 5.8 and the dimensions of it is presented in Appendix E. The joints are mounted to this with the angle offset presented in Table 2.4, where the centre of rotation of the joints correspond to the kinematic parameters presented in Table 2.1. This is intended to be fabricated out of a solid block of aluminium, which requires a raw stock with a diameter of $298mm$. Optionally, the body of the platform could be made from a $170mm$ diameter raw stock where the mounding plates for the joints are welded on afterwards.

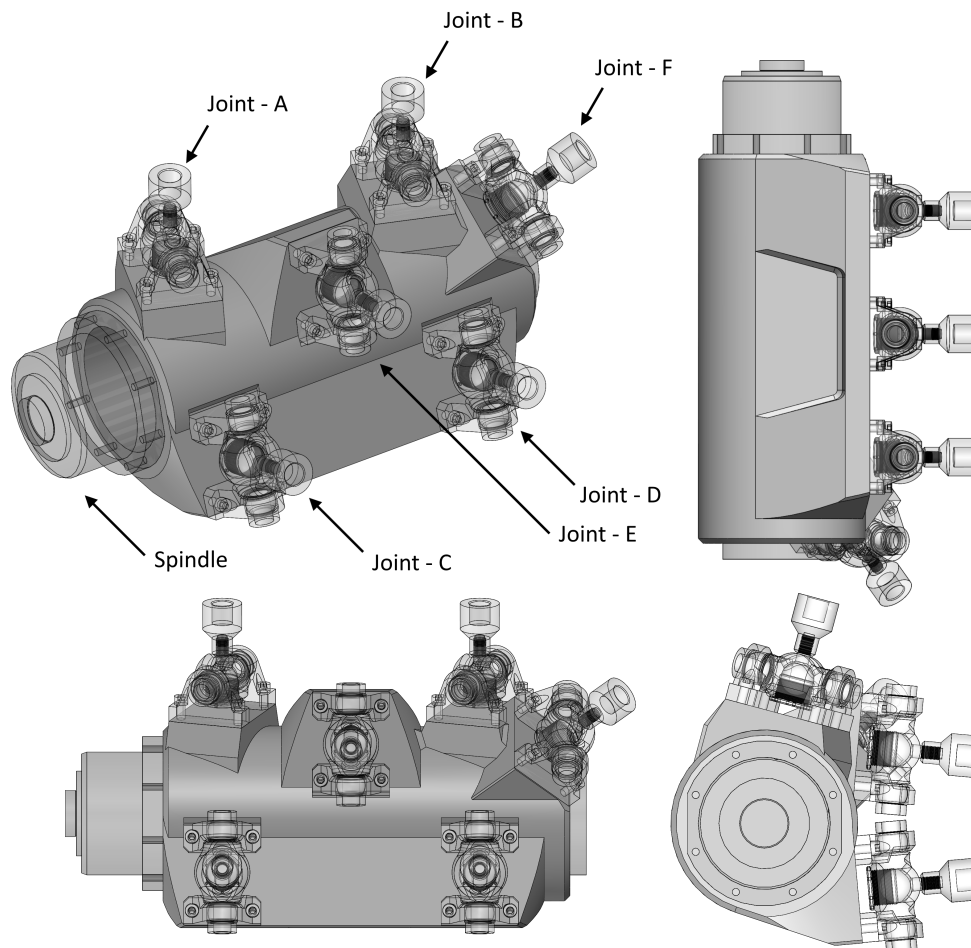


Figure 5.8: Proposed tool platform design

5.6.1 Spindle

The new design of the machine is generally scaled up regarding stiffness and capacity compared to the old prototype. It is, therefore, more representative to consider a larger spindle, as the current spindle is only 2.2kW. The existing spindle also gave some design restriction where the body of the spindle is square and requires clearance for air cooling. This was shown to limit the achievable stiffness of the frame where the weight would have to be increased substantially in order to reach the same stiffness as the proposed design. A 120mm spindle was therefore chosen, since these can fit the whole housing within the cylindrical envelope of 120mm. The general form-factor of this spindle is presented in Figure 5.9.

The spindle that was chosen as a reference, was the *HT 100 A/D/S 45* spindle from *IBAG* [58]. This can deliver power of 7/9.1 kW (S1/S6) and torque of 4.1Nm/5.4Nm (S1/S6). S1 is continuous load, and S6 is the intermittent load.

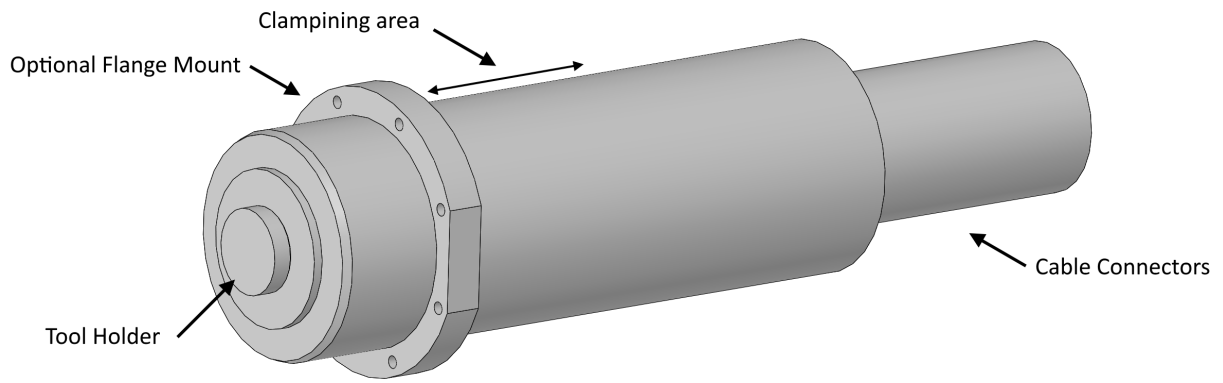


Figure 5.9: Spindle form factor illustration

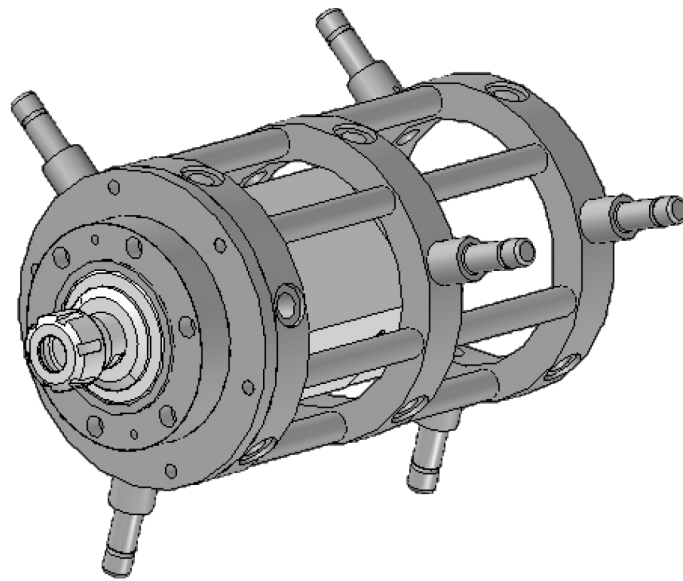


Figure 5.10: Current solution to the tool platform, w/o extended pins for joint A and B

6 Machine Stiffness

In this chapter, the theoretical stiffness of the robot is presented. First shown, is the method used for calculating the workspace stiffness if only the link stiffness is considered. Then, the stiffness of the proposed tool platform design and the gantry carriages are presented, where the effect these have on the total stiffness is presented. Then a short analysis of how the rotation of the tool with 5-axis motion affects the workspace stiffness is presented.

6.1 Only Considering Link Stiffness

Since the links are only subjected to axial forces, the total stiffness of the link can be reduced to a simple one-dimensional problem, where the equivalent stiffness is calculated from equation 6.1.

$$K_{link} = \left(\frac{1}{K_{joint,1}} + \frac{1}{K_{rod/act}} + \frac{1}{K_{joint,2}} \right)^{-1} \quad (6.1)$$

The stiffness of the joints, presented in Chapter 4, was calculated up to the maximum mobility limits of the joints, but as it is seen in Section 2.5, most of the joints do not reach these angles. While it was initially intended for the 2 d.o.f Cardan joint to be used on the side of the gantry carriage, the ball joint design gave a slightly higher stiffness at a lower weight and is therefore considered here. From the stiffness presented in Figure 4.5 and the joint rotation presented in Table 2.5, the minimum stiffness of the joint is $150N/\mu m$, for the joints connected to the tool platform, and $160N/\mu m$, for the joints connected to the carriage. Together with the stiffness of the carbon fibre rod K_{rod} , this gives the passive links a stiffness of $56N/\mu m$ and with the actuator stiffness K_{act} , the active links a stiffness $35N/\mu m$, .

Since the links only transmit axial forces, the force, F , and torque, M , applied to the TCP can be related to the link forces, F_i , by equation 6.2 and equation 6.3, [3].

$$F = \sum_{i=1}^6 F_i u_i \quad (6.2)$$

$$M = \sum_{i=1}^6 F_i A_i \times u_i \quad (6.3)$$

This can be represented as a 6×6 matrix, which is known as the static matrix, H . The first three rows of this matrix are the directional vector of the links A through F. This is described by equation 6.4 between point A on the tool platform and point A1 on the carriage. This was done correspondingly for the other five connection links, B through F.

$$\vec{V}_A = \frac{P_A - P_{A1}}{\|P_A - P_{A1}\|} \quad (6.4)$$

The last three rows of this matrix are the moment arm vector that the TCP makes with the connection points on the tool platform. This is defined as the cross product between the link vector in equation 6.5 and the vector distance between the TCP and the corresponding connection point on the tool platform. The complete static matrix is then assembled as it is presented in equation 6.6.

$$\vec{M}_A = \begin{bmatrix} A_x - X \\ A_y - Y \\ A_z - Z \end{bmatrix} \times \vec{V}_A \quad (6.5)$$

$$H = \begin{bmatrix} \vec{V}_A \cdots \vec{V}_F \\ \vec{M}_A \cdots \vec{M}_F \end{bmatrix} \quad (6.6)$$

Further, in [3] it is shown the duality between the static matrix, H , and the link Jacobian, J_L , where the relationship is described by equation 6.7. Care must be taken in distinguishing this link Jacobian from the robot jacobian, as their not the same for the Gantry-Tau structure.

$$H^{-1} = J_L^T \quad (6.7)$$

It is also shown, that the Cartesian stiffness matrix then reduces to equation 6.8, where K_L is a 6×6 diagonal matrix with the corresponding stiffness of the links A through F. In the derivation of this, the congruence transformation matrix is not taken in to account. This means that the stiffness matrix is not accurate for large displacements, or large external forces, F , since it does not account for change in geometry due to deflection of the TCP. With the low deflections compared to the overall size of the machine, this is seen as an insignificant error.

$$K = H K_L H^T \quad (6.8)$$

The robot stiffness in the corresponding x,y and z-direction are then found with the principle of virtual work. A small force F is applied to the TCP in one direction, where the displacement of the TCP is calculated from the inverse of the Cartesian stiffness matrix, K . The stiffness in each direction x,y and z was then calculated by the magnitude of the applied force divided by the displacement. Since the TCP not only deflects in the direction of the applied force, the stiffness was calculated from equation 6.9, which uses the vector magnitude of the TCP deflections δ_x , δ_y and δ_z .

$$K_x = \frac{F_x}{\sqrt{\delta_x^2 + \delta_y^2 + \delta_z^2}} \quad (6.9)$$

Presented in Figure 6.1 is the Cartesian stiffness with 3-axis motion of the tool, within the 3-axis workspace, presented in Table 2.3, with the link stiffness calculated above.

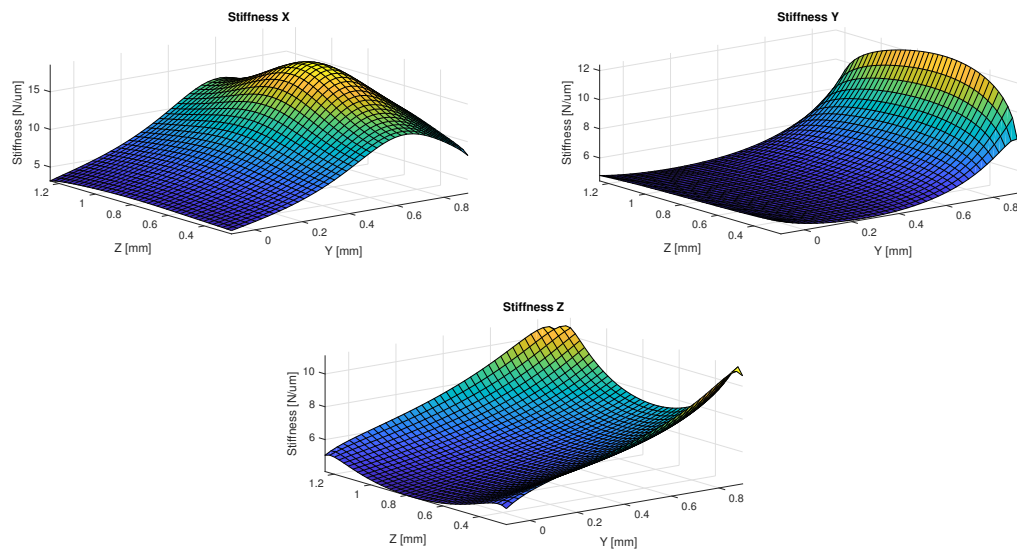


Figure 6.1: Cartesian stiffness, $r_x = 0^\circ$, $r_z = 0^\circ$

To compare the new design to the current prototype, the same calculation was done with the parameters of this. The current prototype uses aluminium links and $50N/\mu m$ joints, which gives a link stiffness of $17N/\mu m$, as presented in [1]. In this, the stiffness of the telescopic link actuator was not considered, but it is seen that the actuators presented in this thesis would not affect this. For consistency, the same kinematic parameters, presented in Section 2.1, is used for this.

The min, max stiffness as well as the stiffness at the centre of the workspace is presented in Table 6.1. Presented in this table is also the gain in stiffness of the new design over the current prototype.

	K_x			K_y			K_z		
	min	max	ctr.	min	max	ctr.	min	max	ctr.
old	1.24	5.99	4.40	1.66	3.92	1.80	1.45	3.60	1.84
New	3.16	18.54	11.85	4.43	12.37	4.94	4.05	11.10	5.17
gain	255%	310%	269%	267%	316%	274%	279%	308%	281

Table 6.1: Workspace stiffness, current and new design

6.2 Tool Platform

With the use of FEM software the proposed tool platform design and the old design was simulated. The simulations were simplified to be calculated at five key positions in the workspace. Four points were placed at the edges of the 5-axis workspace and one in the middle.

To get a better picture of the tool platform stiffness, all other components were simulated as rigid, where the simulation was set up as shown in Figure 6.2. The spindle was modelled as a thin steel body coupled to the TCP with a MPC-Constraint and connected to the tool frame with a bolted flange simplified as a tie constraint. Contact between the spindle body and tool platform was included where the spindle body extends 100mm into the platform. The joint connection was simulated as two dummy plates of steel, tied to the mounting surface of the platform. These are joined to the rigid links with the use of MPC-Constraints where the centre of rotation is in the same place as it is for the actual joints. The frame was meshed with 8mm quadratic tetrahedral elements (C3D10). The stiffness at the reference-points is presented in Table 6.2, where the values are the stiffness of the robot relative to the TCP, where all other components are rigid.

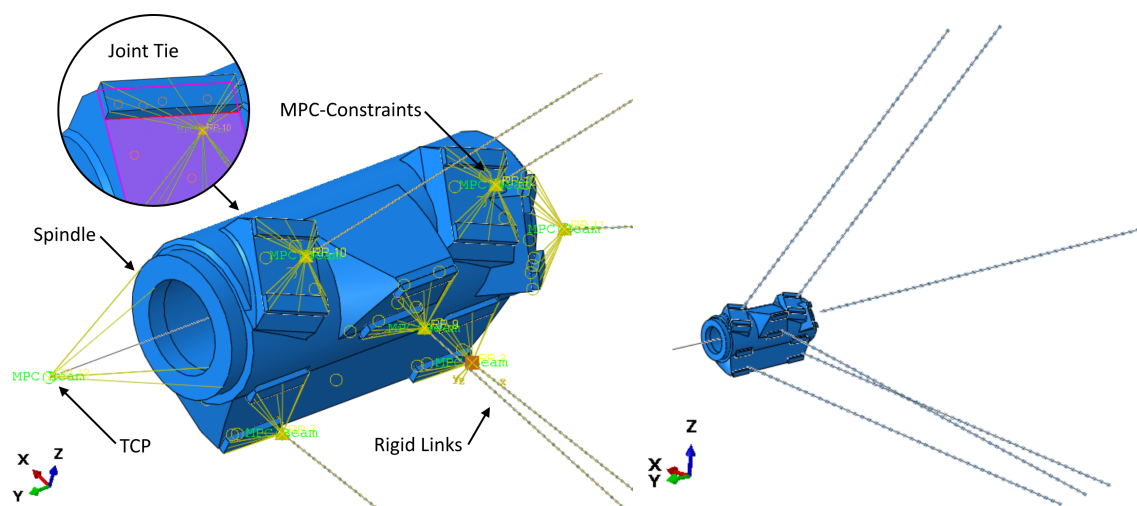


Figure 6.2: Setup of tool platform FEM model

Pos. (y,z)	(0,0.35)	(0.8,0.35)	(0.4,0.75)	(0,1.1)	(0.8,1.1)
K_x	172.53	83.35	188.77	180.30	92.85
K_y	338.50	115.04	154.24	371.31	128.23
K_z	248.38	115.04	113.92	170.93	86.79

Table 6.2: Stiffness of tool platform, relative to TCP [$N/\mu m$]

To compare the new design to the existing solution, the old spindle platform was simulated at the same reference points. The model of the tool platform was simplified as a solid part, since the simulation of all the parts with bolted connections would be far too complicated, considering the goal of the simulation. All simplifications are made in favour of the old design. The result of the simulation is presented in Table 6.3.

Pos. (y,z)	(0,0.35)	(0.8,0.35)	(0.4,0.75)	(0,1.1)	(0.8,1.1)
K_x	1.41	0.49	0.45	0.28	0.30
K_y	1.01	0.53	0.38	0.45	0.43
K_z	0.28	0.53	0.24	0.37	0.47

Table 6.3: Stiffness of old tool platform, relative to TCP [$N/\mu m$]

6.3 Gantry Carriage

The stiffness of the carriage along the direction of travel is primarily characterised by the gantry drive. While both of the drives of the dual drive rack and pinion system can support loads in the same direction, the stiffness of one rack and pinion drive was only considered here. With the rack and pinion solution presented in Section 5.3, the total linear stiffness of this is $97N/\mu m$. The stiffness of the linear bearings characterises the stiffness along the other three directions, as well as the torsional stiffness of the carriage assembly. The stiffness of these are not linear as it depends on the applied load as well as the direction of the load. These were simplified as four linear spring elements with a stiffness of $1100N/\mu m$ in up/down-wards direction and four linear springs with $800N/\mu m$ in the sideways direction. A simplified model was created where the carriage body, and other components, was modelled as rigid bodies using MPC-Constraints, as seen in Figure 6.3.

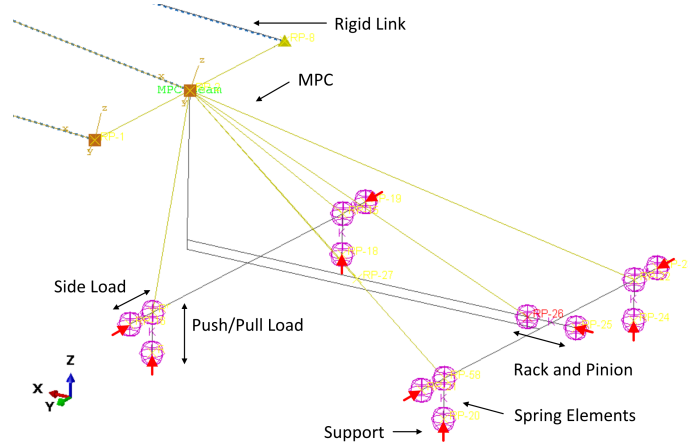


Figure 6.3: Gantry carriage simulation setup

With the rigid carriage frame, the linear bearings, and the rack and pinion drive, the stiffness at the reference-points is presented in Table 6.4. These values are the stiffness of the robot relative to the TCP, where all other components are rigid.

Pos. (y,z)	(0,0.35)	(0.8,0.35)	(0.4,0.75)	(0,1.1)	(0.8,1.1)
K_x	52.71	44.72	90.76	56.01	49.33
K_y	51.06	26.19	23.72	49.24	26.63
K_z	114.47	26.19	50.78	96.02	43.64

Table 6.4: Stiffness of carriage, relative to TCP [$N/\mu m$]

6.4 Platform, Carriage and Link

The total stiffness from the platform, carriage and links was then combined. Since the different components have different stiffness characteristics, the TCP does not deflect in the same direction. Therefore the sum of the deflection, $\delta_x = \delta_{x,link} + \delta_{x,carr} + \delta_{x,plt}$, when only considering links, $\delta_{x,link}$, carriage, $\delta_{x,carr}$ and platform, $\delta_{x,plt}$ was calculated along each direction x, y and z. The total stiffness was then calculated by equation 6.9. With the results above, the stiffness at the reference points is presented in Table 6.5. Shown here is also the percent reduction in stiffness when the carriage and tool platform is considered compared to when only the links are considered.

Pos. (y,z)	(0,0.35)	(0.8,0.35)	(0.4,0.75)	(0,1.1)	(0.8,1.1)
K_x	9.03 (21.7%)	3.81 (12.9%)	10.91 (11.4%)	9.35 (20.7%)	3.98 (12.1%)
K_y	6.96 (15.0%)	3.98 (17.7%)	4.04 (18.8%)	6.87 (15.6%)	3.92 (16.8%)
K_z	7.88 (10.0%)	3.98 (17.7%)	4.55 (12.8%)	7.43 (11.5%)	4.22 (14.6%)

Table 6.5: Robot stiffness w/ link, tool platform and carriage [$N/\mu m$]

It is clear from these results that the link stiffness has the most significant influence on the total stiffness of the robot. This is made more apparent when looking at Figure 6.4, which is the percentage that each of the components contributes to the total deflection at the TCP with the load in each direction x, y and z. Since the deformation is inverse proportional to the stiffness, the lower the area in the graph is, the less effect it has on the total stiffness.

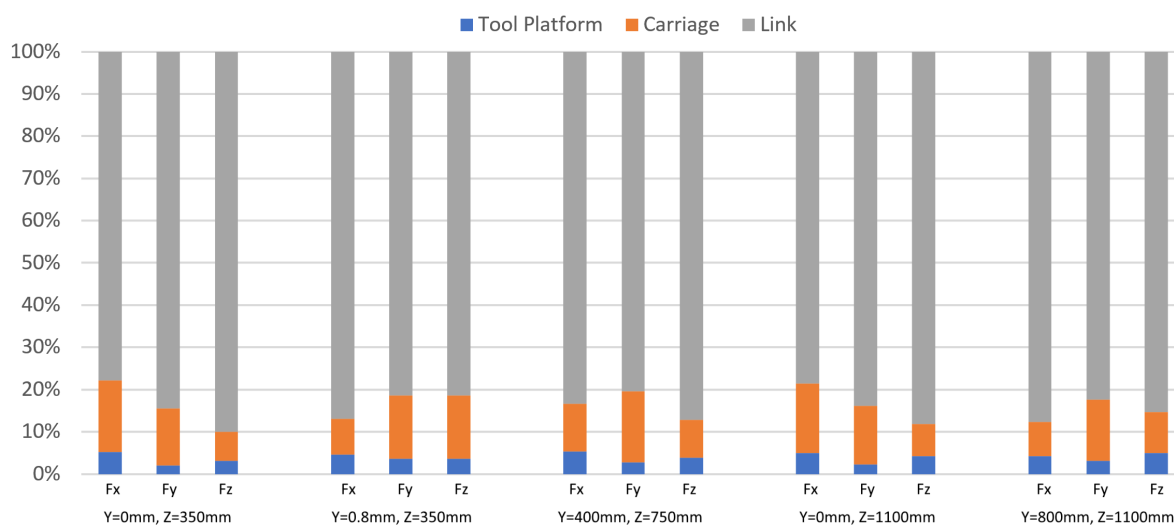


Figure 6.4: Deformation contribution of Tool frame, carriages and links

6.5 5-Axis

Since the robot is intended for 5-axis machining, it was desirable to investigate the stiffness with rotation of the tool. By the same principle mentioned in the previous chapter, the forces follow the rotation of the tool, and it was therefore seen as most representative to calculate 5-axis stiffness in the coordinate frame of the tool. This was done by transforming the force in each direction, x, y and z, with the same method as before by equation 5.9. From the deflection of the TCP the stiffness is then calculated the same way as before by equation 6.9.

The robot stiffness was then calculated with a tool rotation of $\pm 25^\circ$ around X and Z. This changes the stiffness characteristics of the robot where it varies between higher and lower stiffness than with 3-axis movement. Presented in Figure 6.5 is the robot stiffness with tool rotation of positive 25 degrees around the z-axis and no rotation around the x-axis, where only link stiffness is considered. The max and min values found within the 5-axis workspace is presented in Table 6.6. The stiffness at the centre of the workspace, defined as $Y = 389\text{mm}$ and $Z = 715\text{mm}$, is also shown here.

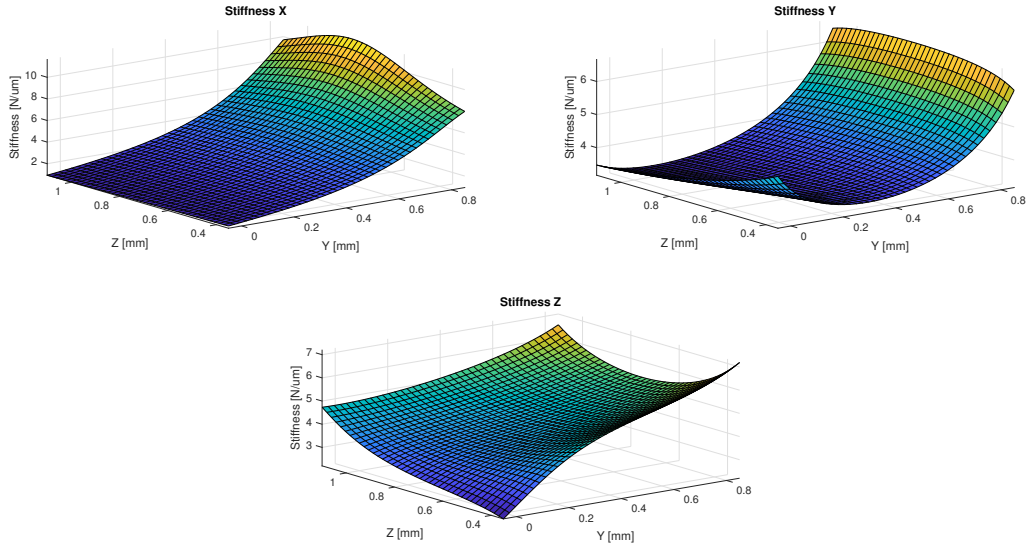


Figure 6.5: 5-axis robot stiffness, $r_x = 0$ $r_z = 25$

dir.		$r_x = 0^\circ$	$r_x = +25^\circ$	$r_x = -25^\circ$	$r_z = 0^\circ$	$r_x = 0^\circ$
		$r_z = 0^\circ$	$r_z = 0^\circ$	$r_z = 0^\circ$	$r_z = +25^\circ$	$r_z = -25^\circ$
K_x	min	4.02	2.75	1.85	0.93	2.91
	max	18.54	17.32	15.44	11.65	15.48
	ctr.	11.83	11.23	11.31	3.01	10.15
K_y	min	4.58	3.56	3.70	3.17	6.08
	max	10.41	10.54	7.28	6.66	14.01
	ctr.	4.94	4.28	3.99	3.54	7.79
K_z	min	4.16	1.41	1.87	2.20	5.54
	max	9.27	5.66	5.45	7.20	11.50
	ctr.	5.19	2.59	2.47	4.18	6.75

Table 6.6: 5-axis robot stiffness, min,max, workspace centre [$N/\mu m$]

7 Discussion

Disclaimer: While specific brands such as *Atlanta Drives/ Stöber* and *Bosch Rexroth* was presented in this thesis, the methods apply to other makes, and does by no means refer to their products as optimal. Their products were rather used due to their available data and the support they provided. It should also be mentioned, that the calculated stiffness of the linear actuators from *Bosh Rexroth* was only approximated from the data in their catalogues, and does not necessarily reflect their actual stiffness. Unknown factors, such as the stiffness of the actuator body and the mounting brackets, may affect these results.

Kinematics The current Gantry-Tau prototype allows for tool rotations of up to 30° . This posed high requirements on the mobility of the joint, and the due to limitations of the proposed design, this was reduced to 25° .

Considering collisions, singularities and reachable limits of the robot, the 2D workspace was presented. While the minimum stroke length of the gantry actuators, required to maintain this workspace was presented, the 3D workspace was not calculated. While it is presented in [34] how the 3 d.o.f workspace shrinks at the end of the gantry limits, tool rotation of the 5 d.o.f robot would also affect this. It should also be noted that, by not making the robot re-configurable, the workspace to footprint ratio is considerably reduced. This decision was made because the author was not able to maintain this ability without reducing the stiffness of proposed joint and tool platform design.

The workspace is also limited at the bottom of the y-axis by collision with the frame of the machine. While the first point of contact is assumed to be between the joint F and the frame, cables from the spindle will likely be sticking out the back of the tool platform, which could cause premature collisions.

The Gantry-Tau structure can be arranged with different configurations than what is presented in this thesis. It should be noted that this can have a significant effect on the machine stiffness and that the configuration of the proposed solution is not necessarily optimal.

Joint design: It is seen with the proposed ball joint design, that the stiffness would be higher if flange plain bearings were used instead. However, the running clearance of these was a concern, and these were therefore ruled out. For applications where the backlash is not as critical, this can, however, be a desirable solution.

In the main FEM simulations of the ball joint, the threaded cap was omitted. While the simulations were conducted with a tensile load on the joint, it can be argued that the cap will add stiffness to the joint. For an accurate representation of its contribution, the threads would likely have to be modelled in the solid model. This was not feasible in this project, due to the large number of elements it would require.

With the separated ball joint simulation, the joint had a slightly lower stiffness than the complete quarter symmetry model. This is presumably because the raceway of the bearing is included in both simulations, and its deformation is calculated twice.

It is seen that the primary cause for the low stiffness of the ball joint is the poor stiffness of the brackets with off centre loads, as seen in Figure 4.4. While some of this effect is due to the bracket being less stiff with bending load, the bolt connection is seen as the largest factor. With increasing load angle, this connection becomes increasingly more slip critical, where some degree of slip is inevitable. This was simulated with a bolt preload of 5kN per bolt and friction was assumed to be $\mu = 0.4$, which is a conservative assumption. Higher preloads would presumably yield a higher stiffness.

The proposed ball joint design is very similar to the one presented in [20]. While no numbers were obtained on the stiffness of this, it was presumed to be inadequate because of the single supported pin design. The advantage of this design is that it has much higher mobility than the joint proposed by the author of this thesis. This would allow for larger tool rotations within the workspace.

The Cardan joint did not reach the same levels of stiffness as the ball joint, even though the ball joint was lighter. It also has a drawback, where the clearance of the cylindrical plain bearing might not be possible to eliminate. The Cardan joint also has a tapered groove, which was added to reduce the effect of the slip critical connection. However, it is clear from the simulation results that it still depends on the coefficient of friction. Some of the issues with the design were addressed, but there was no time left to evaluate this. The latest iteration is presented with 2D-drawings, including dimensions, in Appendix D. It can be argued that it did not receive as much attention as the ball joint did.

With the simulations of the plain bearings, the PTFE polymer based lining was approximated as a linear isotropic material. The material data of the PTFE composite used in the plain bearings were also not well known, where the approximate Young's modulus is known from the catalogues of *Ampep* [26], but the Poisson's ratio is not. It was assumed to be 0.3 which is, presumably, lower than what it is, since pure PTFE has a Poisson's ratio of around 0.48.

Application requirements: The actuator requirements were formulated by studying some specific milling examples. The cutting force calculations shown in this thesis is very simplified compared to the different cutting force models that are available, and the accuracy of this is therefore debatable. These numbers were however merely used to get an understanding of what ballpark the forces were expected to be. Based on this, the actual force requirements were defined through discussion with the supervisors. It is therefore seen in this thesis that there is not a distinct correlation between the defined requirement and what is presented as milling loads. However, it is seen that the feed force of the selected drives, would allow for a higher load than the specified requirement. The actual capacity of the robot was not calculated, which could be done through the forward kinematics.

The specific spindle was also very loosely defined since there was no time for an extensive analysis of the selection of a specific spindle. This is also very much work specific, where the spindle power correlates with the desired material removal rate. Since the machine here at UIA is not intended for high production rates, this spindle was seen as the largest that would be required, which is a conservative assumption.

There is no bright line which separates HSM from conventional machining, and it is seen that the requirements formulated in this thesis fall somewhere in between these. The main selling point of HSM is the increased productivity, which is not the primary focus of the robot here at UIA. It was, however, desirable to get as far into this region as possible as it generally is a high demand application that looks good in an exhibition flyer.

Link actuator The size of the telescopic link actuator was mainly limited by collision with other links. It should be noted that, if the kinematic parameters were adjusted, it could be possible to fit a larger more rigid actuator. This would, however, affect other parameters of the robot such as the tool platform, which would have to be extended. By the time the stiffness of the actuators were calculated, there was no time left to alter these dimensions as it would change many other parameters of the design.

The larger actuators will also increase the overall weight in motion. Due to concerns of compromising the dynamics of the robot, the *EMC-HD* [46] and similar steel frame actuators were ruled out. Other less dynamic applications, such as friction stir welding, could, however, benefit from the higher stiffness these should obtain.

With the selected actuator and the stroke length of 250mm, the total length of the actuator at the middle stroke is not equal to the actual distance between the two joints of 1.1m. It would, therefore, be required to have a rod section that connects the piston of the actuator to the joint on the platform. This would further reduce the stiffness of the actuator where if a 500mm section of the same rod used for with the passive links were used, the total link stiffness would be reduced to $33N/\mu m$.

Rack and pinion drive: The equations for radial and tangential stiffness did not fully correspond with the values presented in [52]. It was therefore assumed that the tilt stiffness given in this was correct, which left the length L_b as the only unknown. While these correspond with the values given by *Wittenstein*, of which the formulas originated from, the definition of the length L_b might not be the same. Presumably, it is the distance to the centre of stiffness with the *Stöber* gearboxes. This is expected to be in between the two angular contact bearings, which more closely correlates with the value of $L_b = 56mm$ which was found through back-calculation from the known total linear stiffness, K_x . While this does not necessarily ensure that the radial and tangential stiffness components are correct, it was only used to highlight the difference between the radial and tangential component. The actual total linear stiffness, used in further calculations, is known from their catalogue [53].

All calculations with the rack and pinion drive were also made with consideration of rigid external support. If the compliance of the carriage were considered, the linear stiffness would likely be notably reduced, where the tangential component of the stiffness would be most critical. It should also be noted that, while not considered in this report, the stiffness of the linear bearing that guides the carriage, will affect the linear stiffness of the rack and pinion drive. To some extent, affect the tangential stiffness but mostly relates to the radial stiffness component, where the pinion is pushed away from the rack towards the linear bearing. This being said, the calculated radial stiffness components is more than ten times the total linear stiffness. This was therefore considered to be insignificant, but more accurate calculations including carriage compliance might show otherwise.

The proposed solution reaches the speed requirement with $V_{max} = 1.6m/s$ but not with the allowable continuous speed, $V_{cont} = 0.72m/s$. It is however expected that the average velocity in a real application should fall below this. Some of the maximum drive speeds were also due to the rotational speed requirement, where the drives required a higher speed to allow for the tool to rotate at a fixed TCP position, where rotation around x-axis was most critical. The rotational speed requirement was not based on the property of any work, and it can be discussed how realistic the requirement of $1.5rad/s$ is. **Gantry Carriage** The body of the gantry carriages was simulated as rigid with linear spring elements representing the bearings and the rack and pinion drive. The linear bearings are presumably much more rigid than the carriage frame, and the usefulness of this simulation is debatable. There was no time to design and test a carriage with considerations of its stiffness, and the shown carriage design is merely a presentation of the overall size and shape it should have. Evaluating the stiffness of this would therefore not be realistic either.

Platform: The tool platform presented in this thesis is intended to be fabricated out of a solid block of aluminium. This requires a rather large raw stock of aluminium, where a large amount of material would have to be removed. This might not be economically feasible, and it was therefore also proposed that the mounting brackets of the joints are welded on afterwards. The welded connection could, however, compromise the stiffness of the platform, and it might not be a feasible solution either.

The FEM simulation of the tool platform and carriage was also limited to five positions in the workspace, primarily due to the time it took to set up the model and evaluate the results. Each calculation point required a designated step, where each load direction x, y and z requires a separate step, as well as movement between calculation points, requires a separate step. Nonlinear geometry, see [59], also had to be included in all the steps, which increases computational time, especially with the steps including movement. This could be avoided by making a designated model for each of the calculation points, but this would significantly increase the model setup time. There might be other more efficient methods, not known to the author, which would simplify this process and allow for a better resolution of the calculated space.

Passive links: The carbon fibre rods were chosen to be 38.1mm as these were the largest commercially available size that the author could find. It is seen that the stiffness of the link assembly can be further increased by using larger rods, which should be possible to custom order. Carbon fibre rods are however reasonably expensive, and if the stiffness of the joints is not increased, the gain in stiffness is not significant.

Dynamics While it is mentioned that the stiffness of the machine was the main focus of this project, it can not be ignored that its dynamic capabilities are also important. Especially if the machine is to be considered an HSM capable machine. Considerations were made to keep down the weight of components such as the tool platform, and joints, but the effect these had on the dynamics was not calculated. Simplified dynamic calculations were performed in conjunction with selecting a motor and gearbox for the rack and pinion drive, where the carriage system was simplified as a one-dimensional system. This did, however, not account for the coupled dynamics of the rest of the system.

An increase in mass will affect the mechanical bandwidth of the machine where it requires higher actuation forces to accelerate the TCP at the same rate. While efforts have been made to keep the weight of the components down, it should also be noted that this goes both ways. It is then seen that disturbances, due to forces transmitted through the tool, also has less effect on a higher mass. It might, therefore, be concluded that for a lightweight design, it is a larger demand on the stiffness of the machine as there is less mass that acts as a dampening of disturbances.

The dynamic performance of the telescopic link actuator was not calculated either. The inertia seen by the motor is mostly determined by the rotational inertia of the platform assembly. The effective inertia seen by the actuator not only changes with tool rotation but also with its TCP position. It is therefore not as easily simplified to a one-dimensional system, where one might have to consider a worst-case scenario. However, it can be argued that the dynamic requirement of this is much lower than for the gantry actuators.

Machine stiffness The stiffness calculations made in this report was performed with a virtual tool length of 250mm, which is defined as the distance from the TCP to the first joint (in the y-direction). This was primarily chosen for constancy, as most of the calculations from earlier papers on the robot were based on this length. It should be noted that this has a significant influence on both the reachable workspace and the machine stiffness, particularly in x and z-direction. The actual length of the end mill would not be 250mm, as this depends on how far into the platform that the spindle is seated. It is therefore seen as a conservative tool length, as the actual tool length considering the selected spindle, is longer than most standard tools.

While the stiffness was evaluated with 5-axis motion, the study was somewhat limited, where only link stiffness was considered. From the presented results, it can, however, be seen that the tool rotation has a significant influence on the machine stiffness where it is as low as $0.99N/\mu m$. This was only investigated for tool rotation of $\pm 25^\circ$ around the x and z-axis independently, which is not necessarily the worst case scenario.

Frame The design of a new frame was not addressed in this report as the time did not allow for it and therefore the effect it has on the machine stiffness was not investigated. It is presented in [60] that, even with the added reinforcement on the current frame, the stiffness is not great, where stiffness in z-direction was as low as $13.55N/\mu m$. This will therefore undoubtedly decrease the stiffness further if it is not improved.

8 Conclusion

A concept of a Gantry-Tau milling machine with 5-axis capabilities has been designed, and its performance has been theoretically evaluated. A state of the art study was conducted on components relevant to the machine, where the best solution was concluded to be a combination of dual drive rack and pinion, for the gantry drives, and ball screw actuators, for the telescopic links.

State of the art study also concluded that no commercial joint reached the desired stiffness while having high enough mobility and low enough weight. Two joint concepts were therefore developed, where one was a 3 d.o.f joint based on a ball joint structure and the other was a 2 d.o.f joint based on the Cardan joint structure. The 3 d.o.f ball joint obtained a stiffness of above $144N/\mu m$ with rotation up to 45° and 70° and a weight of just under 2.1kg. The Cardan joint obtained a stiffness of $152N/\mu m$ at a rotation of 50° around one axis, with a weight of 3.5kg.

A new platform design was also developed, where the lowest calculated stiffness was $83N/\mu m$, compared to $0.49N/\mu m$ with the tool platform of the current prototype, at the same load condition. The new design comes in at a weight of 16.6kg compared to the current, at ≈ 6.5 kg.

With the ball joints, the passive links obtained a stiffness of $56N/\mu m$, and the active links obtained a stiffness of $35N/\mu m$. The lowest calculated workspace stiffness, only considering link stiffness, is $3.16N/\mu m$, $4.42N/\mu m$ and $4.05 N/\mu m$ in x,y and z-direction with 3-axis motion. Including stiffness of linear bearings, rack and pinion drive, and the new tool platform, the workspace stiffness is reduced by 11-21%.

The machine can deliver a feed force more than 1000N with both 5-axis and 3-axis motion, as well as to reach linear feed speeds and a rotational speed of above $1.4m/s$ and $1.5rad/s$ within the centre 70% of the 5-axis workspace.

The desired stiffness of $10N/\mu m$ in the usable workspace was not obtained. Further work is therefore required to meet this goal, where the stiffness of the joints should be further improved. The initial goal for the joint stiffness was $>300 N/\mu m$, which could reach the desired workspace stiffness if larger rods and stiffer actuators are used.

Further Work

Joint design: The dimension of the joints was chosen in an early phase of the development and might therefore not be optimal. However, judging from the final design of the robot, the size of the joints can realistically be increased. How the stiffness of the joints scale with its size should, therefore, be investigated such as to determine an optimal size of the joints better. Also, not all of the joints require the same mobility, as it is seen in Section 2.5, and it could, therefore, be desirable to develop a lower mobility version of the joint for the carriage side of the links. These would also not need 3 d.o.f, and a 2 d.o.f iteration of the joint might give better characteristics.

Tool platform: The design of the tool platform can be further improved, where a more weight efficient design can be obtained. Another approach to the design could then be to construct the platform out of a welded steel link structure instead of solid aluminium. Also, the use of topology optimisation in FEM software such as *Abaqus* could yield a better design.

Rack and pinion drive: The dual drive rack and pinion solution were assumed to be able to work in tandem. This requires more advanced control methods, such as those presented in [48], since the constant torque control scheme will not allow for this. Future work would then be to implement a feedback control system on a carriage system where the accuracy and dynamics can be verified before it is implemented on a complete machine.

It is seen that the limiting factor of the rack and pinion stiffness is the tilting rigidity of the gearbox, where the added pinion support on the ZTRS solution from *Atlanta Drives/ Stöber* can increase the linear stiffness by $\approx 50\%$. This is, to the knowledge of the author, not available for the smaller gearbox size, but a similar solution should be possible to develop if another does not exist for the selected size.

Like with the linear motors, the stiffness of the rack and pinion system can be affected by the control system. The actuation and measurement can then be separated, as it is presented in [61], where the position feedback of the carriages and link actuators can be measured externally with a linear sensor. This can also help with the control system, where there is less disturbance from vibrations within the link structure. This being said, linear encoders will add additional cost to the system, and the cost of accurate encoders might not make the rack and pinion system economically feasible.

Carriage and linear bearings: The linear bearings were more or less selected based on their weight and size. For a more accurate selection process, the different sizes should be simulated where the gain in stiffness can be weighed against their weight and size. This should then be evaluated along with a deformable carriage frame, as this is presumably less rigid than the bearings. The bearings should then be modelled in a more accurate manner, as the method presented in this thesis does not account for the torsional stiffness of the bearings. Modelling the bearing block including all the roller elements would likely require far too many elements and should, therefore, be simplified. Either by replacing the rolling elements by spring elements or by a solid material with an equivalent stiffness, similar to what is presented in [36].

Redundant link d.o.f: Since 3 d.o.f joints were used on both sides of the link it is free to rotate. While this is not an issue for the passive links, where friction within the joint will keep them from rotating, the active links would need external support. Else, the heavy side of the actuator, where the motor is mounted, would create an undesirable rotation of the link.

Redundant actuator: On the current robot, there is an other actuator that replaces the single link, which was not considered in this thesis. With this redundant actuator, the link can be controlled such that its length is minimised, which reduces the forces it is subjected to. This increases the stiffness, where it is seen in [62] that the Cartesian stiffness in the y-direction is increased in the lower region of the y-axis. It should be noted that stiffness of the telescopic actuator is not as high as the passive links. These would also likely require a larger stroke length than 250mm to be effective, which would reduce the stiffness values presented in Table 5.4. This actuator is, however, not as limited by collision, such as the actuator within the three link cluster, and a larger more rigid actuator could then be used. Since this is the only link connected to the carriage, it should also allow for a heavier actuator compared to the other link clusters, assuming equal drives on all carriages. Another parameter is also the economic aspect, where accurate and rigid linear actuators are expensive. It is therefore clear that this should be evaluated within the context of the whole assembly to determine if it is a viable solution.

Robot configuration: While the focus of this thesis has been to improve the stiffness of the robot through structural design of its components, the kinematic parameters and the configuration of the links in the robot has a significant impact on its workspace stiffness. Ongoing research by, T. Brogårdh, have shown that other link configurations can significantly improve the stiffness, which shows that it is still advantageous to work more on the kinematics of the robot.

It is also shown in Section 2.5 that there is much lower mobility requirement on the joints mounted to the tool when the robot only moves in 3-axis. Particularly in joint C, D and E, where it can then be seen that other simpler type of joints, such as Rod ends could be used. These would give a much higher stiffness compared to their weight than the proposed designs. The last two d.o.f required to reach 5-axis motion can then be obtained with a 2-axis milling head, similar to the solution of the *Tricept*. But, as it is discussed in [63], even if the 2-axis head is constructed light and rigid, it risks compromising the advantages of a PKM. Also discussed in [63] is another Gantry-Tau, which is known as the F1 prototype, which is a 6 d.o.f SKM and PKM hybrid solution. This uses fixed links with a parallel configuration of the three link cluster and movable mounting points on the carriage. While this eliminates the need for a 2-axis head, it is understood from conversations with the supervisors that this solution also compromises the stiffness of the robot. It is therefore clear that work can also be done on improving the method of obtaining 5-axis motion, where the current solution with telescopic link actuators might not be the optimal solution.

Machine frame: The time did not allow for the design of a new frame for the complete machine assembly. While the overall size of the robot has not changed much and the proposed solution could be implemented into the old frame, it is desirable to change the orientation of the machine such that the tool is oriented vertically instead. Weight is not as great of a concern with this, and the design is therefore mostly a compromise between installation footprint and stiffness. It is also seen in [60] that the stiffness of the current frame is not necessarily satisfactory, and it is, therefore, desirable to improve this. It also poses other challenges, where accessibility and shielding of operators need to be addressed. Also, to compete against modern milling machines, an automatic tool changer, chip evacuation system and coolant system should be incorporated into the frame.

Dynamic model: As it is mentioned, the coupled dynamics of the robot was not considered. It might, therefore, be advantageous to develop a dynamic model of the machine in software such as *SimulationX* or *SimMechanics* to better evaluate its performance.

Bibliography

- [1] M. Murray, "Design, Analysis and Construction of a Reconfigurable 5-Axis Parallel Kinematics Manipulator," Master's thesis, University of Queensland, Australia, 2006.
- [2] T. Brogårdh, "PKM Research - Important Issues, as seen from a Product Development Perspective at ABB Robotics," *Proc. Workshop on Fundamental Issues and Future Research Directions for Parallel Mechanisms and Manipulators, Quebec, Canada*, Oct. 3-4, 2002.
- [3] Geir Hovland, Ilya Tyapin, "The Gantry-Tau parallel kinematic machine—kinematic and elastodynamic design optimisation," *Meccanica (2011)*, 2009.
- [4] Geir Hovland, Ilya Tyapin, "Multi-Objective Design Optimisation Of A Class Of PKMs - The 3-Dof Gantry-Tau," *Proceedings of the 29th IASTED International Conference Modeling, Identification and Control (MIC 2010), February 15-17, Innsbruck, Austria*, 2010.
- [5] S. coromant, "Die and mold making - application guide," 1999.
- [6] Z. M. R.S. Mishra, "Friction stir welding and processing," *Materials Science and Engineering: R: Reports*, vol. 50, no. 1-2, pp. 1-78, 31 August 2005.
- [7] M. Melendez, W. Tang, C. Schmidt, J. C. McClure, A. C. Nunes, L. E. Murr, "tool forces developed during friction stirwelding," 2003.
- [8] F. X. Lihui Wang, *Smart Devices and Machines for Advanced Manufacturing*. London: Springer, 2008.
- [9] Bosch Rexroth, "Screw assemblies." <https://goo.gl/gYjiUZ>, 2018. [Online; accessed 08-05-2018].
- [10] Skf, "Roller screws." <https://goo.gl/2mf9nt>, 2012. [Online; accessed 10-03-2018].
- [11] Kristin Lewotsky, "Linear Actuators Combine Performance and Economy." <https://goo.gl/bNaDRz>, 2012. [Online; accessed 08-03-2018].
- [12] Machine Design, "Linear AC Motors." <https://goo.gl/dypD8c>, 2002. [Online; accessed 08-03-2018].
- [13] Herve Stampfli , "Linear motor applications: Ironcore versus Ironless Solutions, Whitepaper." <https://goo.gl/TsW4Qd>, 2005. [Online; accessed 11-03-2018].
- [14] Robert Novotnak, Robert Sobek, Stephen A. Botos, "Linear motors: How to beat the heat." <https://goo.gl/6cnSbM>, 2000. [Online; accessed 11-03-2018].
- [15] Steven Engineering, "Linear Motors and Stages." <https://goo.gl/51odhd>, 2000. [Online; accessed 11-03-2018].

- [16] M. R. Everman, "Positioner utilizing engaged toothed gear belts, one static and one dynamic," 2008-06-10. US Application, US20090301237A1.
- [17] Corbon, "Balljoints." <http://www.corebon.com/modular.html>. [Online; accessed 11-03-2018].
- [18] INA Schaeffler, "Components for parallel kinematics." <https://goo.gl/exd8e6>. [Online; accessed 11-05-2018].
- [19] Myostat Motion Control, "Spherical Rolling Joints." <https://goo.gl/n3Bkbp>. [Online; accessed 14-03-2018].
- [20] Jiangzhen Guo, Dan Wang, Rui Fan, Wuyi Chent, "Design and workspace analysis of a 3-degree-of-freedom parallel swivel head with large tilting capacity," *Proceedings of the Institution of Mechanical Engineers Part B Journal of Engineering Manufacture* 231(10), 2015.
- [21] Matej Karasek, Michael Valasek, "Mechatronic Spherical Joints for Increased Mobility," *Conference: Computational mechanics 2009At: Hrad Nectiny, Czech Republic*, 2009.
- [22] INA Schaeffler, Frank Dürschmied, "Assemblies for Parallel Kinematics." <https://goo.gl/DePDoa>. [Online; accessed 11-05-2018].
- [23] J. Merlet, *Parallel Robots*. Dordrecht, The Netherlands: Springer, 2006.
- [24] Rainer Gloess, "Cardan Joints With Axis Offset In Singularity Free Hexapod Structures For Nanometer Resolution," 2009.
- [25] S.Blair, W.O.Winer, "Tribological characteristics of needle bearings," *Tribology Series Volume 14, 1989, Pages 269-276*, 1989.
- [26] Skf, "AMPEP self-lubricating plain bearings." <https://goo.gl/kNJNvs>. [Online; accessed 11-05-2018].
- [27] Igus, "iglidur JVFM, clearance-free prestressed bearing with flange." <https://goo.gl/hYZeWw>. [Online; accessed 11-05-2018].
- [28] Bosch Rexroth, "Ball Rail Systems." <https://goo.gl/tVqjja>. [Online; accessed 14-05-2018].
- [29] Bosch Rexroth, "Roller Rail Systems." <https://goo.gl/msFiKo>. [Online; accessed 14-05-2018].
- [30] Igus, "drylin T - Linear guide systems." https://www.igus.com/wpck/17352/drylin_t. [Online; accessed 14-05-2018].
- [31] Birmingham Machining Tool Services, "Turcite-B Anti-Friction Slideways." <https://goo.gl/jGqEuj>. [Online; accessed 11-05-2018].
- [32] Matthew Murray, Geir Hovland, Torgny Brogårdh, "Singularity-Free Reconfiguration of the 5-DOF Gantry-Tau Parallel Kinematic Machine," *Proceedings of the Second International Workshop on Fundamental Issues and Future Research Directions for Parallel Mechanisms and Manipulators*, 2008.
- [33] T. A. Jeffrey C. Hudgens, "Planning link-interference-free trajectories for a parallel link manipulator," in *Industrial Electronics, Control, and Instrumentation, 1993. Proceedings of the IECON '93., International Conference on*, IEEE, 1993.

- [34] Geir Hovland, Ilya Tyapin, Torgny Brogårdh, “A Fully Geometric Approach For The Workspace Area Of The Gantry-Tau Parallel Kinematic Manipulator,” 2007.
- [35] C. SOUTIS, “Compression testing of pultruded carbon fibre-epoxy cylindrical rods,” *Journal of Materials Science* 34, 2000.
- [36] László Molnár, Károly Váradi, Gábor Bódai, Péter Zwierczyk, László Oroszváy, “Simplified modeling for needle roller bearings to analyze engineering structures by FEM,” *Periodica Polytechnica Mechanical Engineering*, 54(1), pp. 27-33, 2011.
- [37] INA Schaeffler, “Bearing deflection.” <https://goo.gl/vqNxNo>. [Online; accessed 11-04-2018].
- [38] uk.misumi-ec, “Precision Lock Nuts.” <https://uk.misumi-ec.com/vona2/detail/110300114130/>. [Online; accessed 11-04-2018].
- [39] Dassault Systèmes, “22.1 Understanding bolt loads.” <https://goo.gl/MrggmH>. [Online; accessed 15-04-2018].
- [40] Dassault Systèmes, “35.2.2 General multi-point constraints, MPCs for connections and joints.” <https://goo.gl/VpNR7Q>. [Online; accessed 11-04-2018].
- [41] S. Coromant, “Milling tools.” <https://goo.gl/KPaFQQ>, 2018. [Online; accessed 16-04-2018].
- [42] S. Coromant, “Coromill plura solid carbide end mill for heavy roughing.” <https://goo.gl/Ne54bX>, 2018. [Online; accessed 16-04-2018].
- [43] S. Coromant, “Coromill plura solid carbide end mill for medium roughing.” <https://goo.gl/TZgBy7>, 2018. [Online; accessed 16-04-2018].
- [44] Mark A. Rubeo, Tony L. Schmitz, “Milling Force Modeling: A Comparison of Two Approaches,” *44th Proceedings of the North American Manufacturing Research Institution of SME*, vol. 5, no. 2, p. 90–105, 2016.
- [45] Bosch Rexroth, “Electromechanical cylinders emc.” <https://goo.gl/Z4iZN6>, 2018. [Online; accessed 08-05-2018].
- [46] Bosch Rexroth, “Electromechanical cylinders emc-hd.” <https://goo.gl/Sh1DU5>, 2018. [Online; accessed 08-05-2018].
- [47] Bosch Rexroth, “Synchronous servo motor, msk05x.” <https://goo.gl/wQnRuR>, 2018. [Online; accessed 08-05-2018].
- [48] Sven Gestegård Robertz, Lorenz Halt, Sameer Kelkar, Klas Nilsson, Anders Robertsson, Dominique Schär, Johannes Schiffer, “Precise robot motions using dual motor control,” *Proceedings - IEEE International Conference on Robotics and Automation, Anchorage Convention District, May 3-8, 2010, Anchorage, Alaska, USA*, 2010.
- [49] Stöber, “Servofit, servo gear units.” <https://goo.gl/dtiyVm>, 2018. [Online; accessed 08-05-2018].
- [50] Qibin Wang, Yimin Zhang, “A model for analyzing stiffness and stress in a helical gear pair with tooth profile errors,” *Journal of Vibration and Control* 1–18, 2017, vol. 23, no. 2, 2015.
- [51] Wittenstein, “Alpha linear systems, product catalogue.” <https://www.wittenstein.de/download/alpha-linear-systems-us.pdf>, 2018. [Online; accessed 08-05-2018].

- [52] Stöber, “"ph" series servofit precision planetary gearhead performance specifications.” <https://goo.gl/hpoNf8>, 2018. [Online; accessed 08-05-2018].
- [53] Stöber, Atlanta, “Highforce ztrs/ztr/zr.” <https://goo.gl/BXzWLi>, 2018. [Online; accessed 08-05-2018].
- [54] Stöber, “Drives and automation 2017.” <https://goo.gl/6TvsAZ>, 2017. [Online; accessed 08-05-2018].
- [55] C.Pradere, C.Sauder, “Transverse and longitudinal coefficient of thermal expansion of carbon fibers at high temperatures,” *Carbon*, vol. 46, no. 14, pp. 1874–1884, 2008.
- [56] Rock West Composites, “Rod - pultruded.” <https://goo.gl/HZsaK6>, 2018. [Online; accessed 08-05-2018].
- [57] Rock West Composites, “Pyrofil hr40.” <https://goo.gl/N43QRe>, 2018. [Online; accessed 08-05-2018].
- [58] IBAG, “Medium spindles, ht 100 a/d/s 45.” <https://goo.gl/xUARhH>, 2018. [Online; accessed 08-05-2018].
- [59] Dassault Systèmes, “8.3.1 Geometric nonlinearity.” <https://goo.gl/MF61s7>. [Online; accessed 11-04-2018].
- [60] T. Brogårdh, S. Hanssen, G. Hovland, “Application-Oriented Development of Parallel Kinematic Manipulators with Large Workspace,” 2005.
- [61] David Corbel, Olivier Company, Sébastien Krut, François Pierrot, “Enhancing PKM Accuracy by Separating Actuation and Measurement: A 3DOF Case Study,” *J. Mechanisms Robotics* 2(3), 031008 (Jul 21, 2010) (11 pages), 2010.
- [62] Geir Hovland, Martin Choux, Matthew Murray, Torgny Brogårdh, “Benchmark of the 3-DOF Gantry-Tau Parallel Kinematic Machine,” *2007 IEEE International Conference on Robotics and Automation*, 2007.
- [63] Dressler, Isolde, “Modeling and Control of Stiff Robots for Flexible Manufacturing,” 2012.
- [64] Z. M. Bi, Y. Jin, R. Gibson, P. McTotal, “Kinematics of parallel kinematic machine Exechon,” *Information and Automation, 2009. ICIA '09, Conference 22-24 June 2009*, 2009.
- [65] Youyu Wang, Haitao Liu, Tian Huang, Derek G. Chetwynd, “Stiffness Modeling of the Tricept Robot Using the Overall Jacobian Matrix,” *J. Mechanisms Robotics* 1(2), 021002 (Jan 06, 2009) (8 pages), 2007.
- [66] M.WeckD.Staimer., “Parallel Kinematic Machine Tools – Current State and Future Potentials,” *CIRP Annals, Aachen University of Technology, Aachen, Germany*, vol. 51, no. 2, pp. 671–683, 2002.
- [67] I. M. M. Company, “Octahedral Hexapod Design Promises Enhanced Machine Performance,” 2001.
- [68] enginoor.com, “Stewart Platform Mill.” <https://www.enginoor.com/tag/giddings-and-lewis/>, 2014. [Online; accessed 08-05-2018].
- [69] S. J. Du, “Simulation and Tool Path Optimization for the Hexapod Milling Machine,” p. 2, 2005.

- [70] M. Geldart, P. Webb a, H. Larsson, M. Backstrom, N. Gindy, K. Rask, “A direct comparison of the machining performance of a variax 5 axis parallel kinetic machining centre with conventional 3 and 5 axis machine tools,” *International Journal of Machine Tools & Manufacture, The University of Nottingham*, vol. 43, no. 11, 2003.
- [71] I. Bonev, “Company profile of toyoda machine works, ltd.” <https://www.parallemic.org/WhosWho/Companies/Profile002.html>. [Online; accessed 31-03-2018].
- [72] Okuma, “PM-600.” okuma.com/pm-600, 2014. [Online; accessed 08-05-2018].
- [73] Daniel Kanaan, Philippe Wenger, Damien Chablat, “Kinematic analysis of a serial–parallel machine tool: The VERNE machine,” *Mechanism and Machine Theory, Institut de Recherche en Communications et Cybernétique de Nantes*, vol. 44, no. 2, 2009.
- [74] M TerrierM GiménezJy HascoetJy Hascoet, “VERNE - A five-axis parallel kinematics milling machine,” *Proceedings of the Institution of Mechanical Engineers Part B Journal of Engineering Manufacture*, 2005.

List of Figures

1	Current prototype situated at UiA	2
1.1	Linear motor configurations, rod style (L), Flat (M), U-channel (R)	8
1.2	Rack and pinion backlash elimination, split pinion (L), torsion spring before gearbox (M), electronic preload (R)	10
1.3	Ball joint (L), Rod end (R)	12
1.4	Cardan joint structure, normal position(L), singular position(R)	13
1.5	INA joint [18], used on current prototype	14
2.1	Gantry-Tau kinematic structure(L), Tool platform kinematic structure (R)	17
2.2	Valid workspace, with 3-axis motion (L), with 5-axis motion (R)	21
2.3	Rotation of carriage mounted joints, with 5-axis motion	23
2.4	Rotation of tool platform mounted joints, with 5-axis motion	23
2.5	Joint rotation with 3-axis motion, carriage mounted joints	24
2.6	Joint rotation with 3-axis motion, tool platform mounted joints	24
3.1	Flange plain bearing dimension	27
3.2	Composite plain bearing FEM model setup (L), deformation radial load 1000N (R) .	27
3.3	Spherical plain bearing dimension (L), axial load simulation setup (R)	28
3.4	Spherical plain bearing deformation, radial load 1000N (L), axial load 1000N (R) . .	28
3.5	Composite spherical plain bearing deformation, axial load, tie connection $\mu = 0.1$ (L), interference fit $\mu = 0$	29
3.6	Radial stiffness of NKI series bearings(L), axial stiffness of K811 series bearings (R)	30
3.7	Ball joint at 0 deg. W/ flange plain bearing (L), W/ spherical plain bearing (R) . .	31
3.8	Ball joint at 45 deg. W/ flange plain bearing (L), W/ spherical plain bearing (R) . .	31
3.9	Ball joint design, exploded view	32
3.10	Ball joint design, cut view with rotation axes	33
3.11	Ball joint link adapter (L), optional set screw (R)	33
3.12	Ball joint threaded cap	33
3.13	Cardan joint, exploded view	34
3.14	Cardan joint, split view	35
3.15	Cardan joint link adapter	35
4.1	Ball joint quarter symmetry, simulation setup (L), simulation result (R)	36
4.2	Link adapter simulation, FEM setup (L), Deformation w/ 1000N load (R)	37
4.3	Ball joint simulation setup, body and bearing(L), bracket and bolt connection (R) .	38
4.4	Stiffness of ball joint with rotation, body and bearing (L), mounting bracket (R) . .	38
4.5	Total ball joint stiffness with rotation of axis-2	39
4.6	Joint cap simulation, FEM setup (L), thread deformation (R)	39
4.7	Application proposal of PTFE liner (yellow) on ball joint	40
4.8	Deformation of simplified ball joint, W/o liner (L), W/ 0.3mm liner (M), W/ 0.5mm liner (R)	40

4.9	Cardan joint, simulation setup	41
4.10	Deformation of simplified Cardan joint assembly, Load angle (0,0) (L), Load angle (50,0) (M), Load angle (0,50) (R)	41
4.11	Deformation of Cardan joint yoke, with tie connection(L), $\mu = 0.2$ (M), $\mu = 0.6$ (R) .	42
5.1	Complete assembly of proposed design	43
5.2	Max cutting force of spindle versus tool diameter (L), Cutting force components (R)	45
5.3	Main components of the linear actuator	49
5.4	Dual drive rack and pinion solution	53
5.5	Gantry carriage	58
5.6	Passive link assembly, rod length	59
5.7	Tool platform load cases	60
5.8	Proposed tool platform design	61
5.9	Spindle form factor illustration	62
5.10	Current solution to the tool platform, w/o extended pins for joint A and B	62
6.1	Cartesian stiffness, $r_x = 0^\circ$, $r_z = 0^\circ$	65
6.2	Setup of tool platform FEM model	66
6.3	Gantry carriage simulation setup	67
6.4	Deformation contribution of Tool frame, carriages and links	68
6.5	5-axis robot stiffness, $r_x = 0$ $r_z = 25$	69

List of Tables

2.1	Tool platform kinematic parameters [mm]	18
2.2	Robot kinematic parameters [mm]	18
2.3	Reachable coordinates and workspace area	21
2.4	Recommended joint offset angles	23
2.5	Required joint mobility with 3-axis and 5-axis motion with $r_x = \pm 25$ and $r_z = \pm 25$	24
3.1	Specific stiffness of carbon fibre, steel and aluminium	26
3.2	Composite flange plain bearing stiffness [26]	27
3.3	Spherical plain bearing dimensions [26]	28
4.1	Cardan joint stiffness	42
5.1	Recommended parameters and requirement for slot milling with HSS end mill in aluminium and steel	44
5.2	Machine requirements	46
5.3	Actuator force and velocity requirement	49
5.4	Approximated stiffness of ball and roller screw actuators, [$N/\mu m$] [9]	52
5.5	Bosch Rexroth EMC-63 with MSK050C-0450, [45] [47]	52
5.6	Properties of rack and pinion drive system sizes [49] [53]	57
5.7	Motor and gear combinations, [53]	57
5.8	ZTR212S PH421F0040 with EZ404U [53] [54]	57
6.1	Workspace stiffness, current and new design	65
6.2	Stiffness of tool platform, relative to TCP [$N/\mu m$]	66
6.3	Stiffness of old tool platform, relative to TCP [$N/\mu m$]	67
6.4	Stiffness of carriage, relative to TCP [$N/\mu m$]	67
6.5	Robot stiffness w/ link, tool platform and carriage [$N/\mu m$]	68
6.6	5-axis robot stiffness, min,max, workspace centre [$N/\mu m$]	69

Appendices

A Inverse Robot Jacobian

Derivation of the analytic inverse robot jacobian (rY is treated as an independent variable)

```
> restart :
with(LinearAlgebra) :
with(CodeGeneration) :
```

The rotation matrix is:

```
> Rx := matrix(3, 3, [[1, 0, 0], [0, cos(rX), -sin(rX)], [0, sin(rX), cos(rX)]]):
Rz := matrix(3, 3, [[cos(rZ), -sin(rZ), 0], [sin(rZ), cos(rZ), 0], [0, 0, 1]]):
Ry := matrix(3, 3, [[cos(rY), 0, sin(rY)], [0, 1, 0], [-sin(rY), 0, cos(rY)]]):
RR := evalm(Rx.Rz.Ry) :
```

Then the offset of the tool holder connection points in the global frame is:

```
> a := evalm(RR.matrix(3, 1, [A_x, A_y, A_z])) :
Ax := a[1, 1] : Ay := a[2, 1] : Az := a[3, 1] :
b := evalm(RR.matrix(3, 1, [B_x, B_y, B_z])) :
Bx := b[1, 1] : By := b[2, 1] : Bz := b[3, 1] :
c := evalm(RR.matrix(3, 1, [C_x, C_y, C_z])) :
Cx := c[1, 1] : Cy := c[2, 1] : Cz := c[3, 1] :
d := evalm(RR.matrix(3, 1, [D_x, D_y, D_z])) :
Dx := d[1, 1] : Dy := d[2, 1] : Dz := d[3, 1] :
E := evalm(RR.matrix(3, 1, [E_x, E_y, E_z])) :
Ex := E[1, 1] : Ey := E[2, 1] : Ez := E[3, 1] :
F := evalm(RR.matrix(3, 1, [F_x, F_y, F_z])) :
Fx := F[1, 1] : Fy := F[2, 1] : Fz := F[3, 1] :
```

The equation for the drives, with respect to the TCP position (X,Y,Z,rX,rZ) is: Note: cf=(-1) -> left configuration, cf=(+1) -> right configuration

```
> q1 := (X, Y, Z, rX, rZ) -> (X + F_x) + cf*sqrt(LF^2 - (Y + Fy - F1_y)^2 - (Z + Fz - F1_z)^2) :
q2 := (X, Y, Z, rX, rZ) -> (X + A_x) + cf*sqrt(LA^2 - (Y + Ay - A1_y)^2 - (Z + Az - A1_z)^2) :
q3 := (X, Y, Z, rX, rZ) -> (X + C_x) + cf*sqrt(LC^2 - (Y + Cy - C1_y)^2 - (Z + Cz - C1_z)^2) :
q4 := (X, Y, Z, rX, rZ) -> sqrt(((X + A_x) + cf*sqrt(LA^2 - (Y + Ay - A1_y)^2 - (Z + Az - A1_z)^2) - (X + Bx))^2 + (B1_y - (Y + By))^2 + (B1_z - (Z + Bz))^2) :
q5 := (X, Y, Z, rX, rZ) -> sqrt(((X + C_x) + cf*sqrt(LC^2 - (Y + Cy - C1_y)^2 - (Z + Cz - C1_z)^2) - (X + Dx))^2 + (D1_y - (Y + Dy))^2 + (D1_z - (Z + Dz))^2) :
```

The inverse robot jacobian is then:

```
> Jq := Matrix(5, 5, [ ]) :
Jq[1, 1] := diff(q1(X, Y, Z, rX, rZ), X) : Jq[1, 2] := diff(q1(X, Y, Z, rX, rZ), Y) : Jq[1, 3] := diff(q1(X, Y, Z, rX, rZ), Z) : Jq[1, 4] := diff(q1(X, Y, Z, rX, rZ), rX) : Jq[1, 5] := diff(q1(X, Y, Z, rX, rZ), rZ) :
Jq[2, 1] := diff(q2(X, Y, Z, rX, rZ), X) : Jq[2, 2] := diff(q2(X, Y, Z, rX, rZ), Y) : Jq[2, 3] := diff(q2(X, Y, Z, rX, rZ), Z) : Jq[2, 4] := diff(q2(X, Y, Z, rX, rZ), rX) : Jq[2, 5] := diff(q2(X, Y, Z, rX, rZ), rZ) :
Jq[3, 1] := diff(q3(X, Y, Z, rX, rZ), X) : Jq[3, 2] := diff(q3(X, Y, Z, rX, rZ), Y) : Jq[3, 3] := diff(q3(X, Y, Z, rX, rZ), Z) : Jq[3, 4] := diff(q3(X, Y, Z, rX, rZ), rX) : Jq[3, 5] := diff(q3(X, Y, Z, rX, rZ), rZ) :
```

$$\begin{aligned}
 Jq[4, 1] &:= \text{diff}(q4(X, Y, Z, rX, rZ), X) : Jq[4, 2] := \text{diff}(q4(X, Y, Z, rX, rZ), Y) : Jq[4, 3] \\
 &:= \text{diff}(q4(X, Y, Z, rX, rZ), Z) : Jq[4, 4] := \text{diff}(q4(X, Y, Z, rX, rZ), rX) : Jq[4, 5] \\
 &:= \text{diff}(q4(X, Y, Z, rX, rZ), rZ) : \\
 Jq[5, 1] &:= \text{diff}(q5(X, Y, Z, rX, rZ), X) : Jq[5, 2] := \text{diff}(q5(X, Y, Z, rX, rZ), Y) : Jq[5, 3] \\
 &:= \text{diff}(q5(X, Y, Z, rX, rZ), Z) : Jq[5, 4] := \text{diff}(q5(X, Y, Z, rX, rZ), rX) : Jq[5, 5] \\
 &:= \text{diff}(q5(X, Y, Z, rX, rZ), rZ) :
 \end{aligned}$$

Output matrix to matlab format

\Rightarrow Matlab(Jq, output = "InvJacobian.m") :

B PKM Machining Centres

PKM machining centres are not as common as Cartesian stacked axis machining centres. However, over the years, some PKM and hybrid PKM machining centres have been developed, and some have been commercialised. These were studied to get a better understanding of the performances that a PKM structure can bring to the field.

Tricept and Tricenter

The most commercially successfully parallel based machining robot is the Tricept, where according to *PKMtricept SL's* website, over 300 units have been sold and installed worldwide. *PKMtricept SL's* was born after the disappearance of *Smtricepy AB* (former *Neos Robotics AB*) and has since bought all rights to the Tricept structure. It consists of three actuated and one passive kinematic chain and is therefore only a native 3 d.o.f PKM. Bending and torsion will therefore occur in the arms, with the three arm Ticept (*Exechon* see [64]), or in the centre support tube, with the structure four arm structure, see [65]. A 2 d.o.f SKM based wrist is then required to obtain 5 d.o.f, which makes the structure a Hybrid PKM. A 2 d.o.f wrist gives the robot the possibility of high tool rotations but reduces its stiffness, compared to a pure PKM.

The Tricept TR805 of former *NEOS ROBOTICS AB* has a cylindrical workspace of $\varnothing 2500 \times 800$ with a repeatability of $20 \mu m$ and are capable of linear speeds up to $90 m/min$ and accelerations up to $10 m/s^2$ [66].

Tricenter of *Dechel Maho* is the machining centre variant of the Tricept structure. According to [66] it has a workspace of $630 \times 630 \times 600 mm$, a rapid traverse rate of $120/90/90 m/min$ in x, y and z and can rotate the head at 30 rpm (3.14 rad/s). It uses ball screws for its linear axes and has a repeatability of $< 10 \mu m$.

Hexaglide

The Hexaglide has the same structure as Hexapod, except that the links are passive and connected to six independent parallel gantries. This robot is then a 6 d.o.f robot, where the x-axis is extendable. The Hexaglide of *ETH Zürich* has a workspace of 600×500 in the y-z plane and are capable of accelerations up to $35 m/s^2$ [66].

VOH-1000

The Octahedral Hexapod (VOH-1000) was a project by Ingersoll Milling Machine Company which started around 1987. It was based on the Stewart platform design, which is also referred to as a Hexapod. As of December 2001, three units have been sold, which was sold to NIST, Aachen University, and Lockheed-Martin's research facility. These sales were intended for further research and development [67]. According to [66], it has a feed rate of $40m/min$ ($0.67m/s$), acceleration capability of $0.5m/s^2$ and a repeatability of $10\mu m$ [66].

HOH-600

Another design of Ingersoll is the HOH-600 which is tilted 90 degrees compared to the VOH-1000, such that the tool lies horizontally. According to [66], it has a workspace of $600x600x800mm$ and repeatability of $6\mu m$. It is capable of a tool rotation of $\pm 30^\circ/\pm 15^\circ$ and can reach a linear velocity of $40m/min$ $0.67m/s$ and accelerations up to $3.5m/s^2$.

Variax

The Variax of Giddings and Lewis is a Stewart platform based design, similarly to the Octahedral Hexapod, but with crossed links, see [68]. This is actuated by ball screws, which gives the machine a feed rate of $66m/min$ ($1.1m/s$), acceleration capability of $10m/s^2$ and a repeatability of $11\mu m$ [69]. It has a theoretical workspace stiffness of $175N/\mu m$ [70] and has a workspace of $700x700x750mm$. However, as it is seen in [68] this workspace is small compared to the footprint of the robot.

HexaM

The HexaM of Toyda Machine Works Ltd. is a 6 d.o.f robot sold as a 5-axis milling machine, see [71]. It is the only PKM based machining centre of Toyda Machine Works. According to [66], it has a workspace of $500x500x350mm$, tool rotation of $\pm 40^\circ/\pm 20^\circ$, linear speed of $100m/min$ ($1.7m/s$), rotational speed of $150rad/min$ ($2.5rad/s$), acceleration capability of $15m/s^2$, and has an accuracy of $12 - 29\mu m/300mm$.

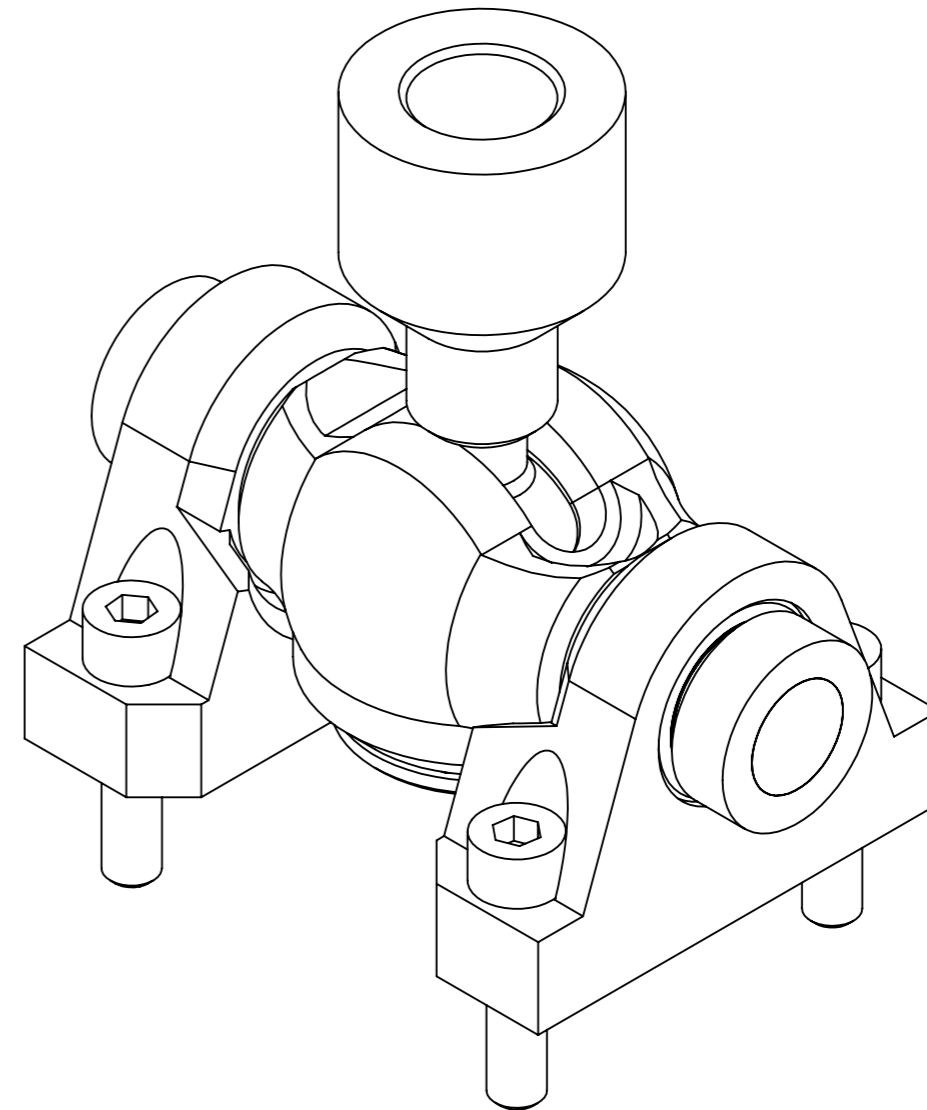
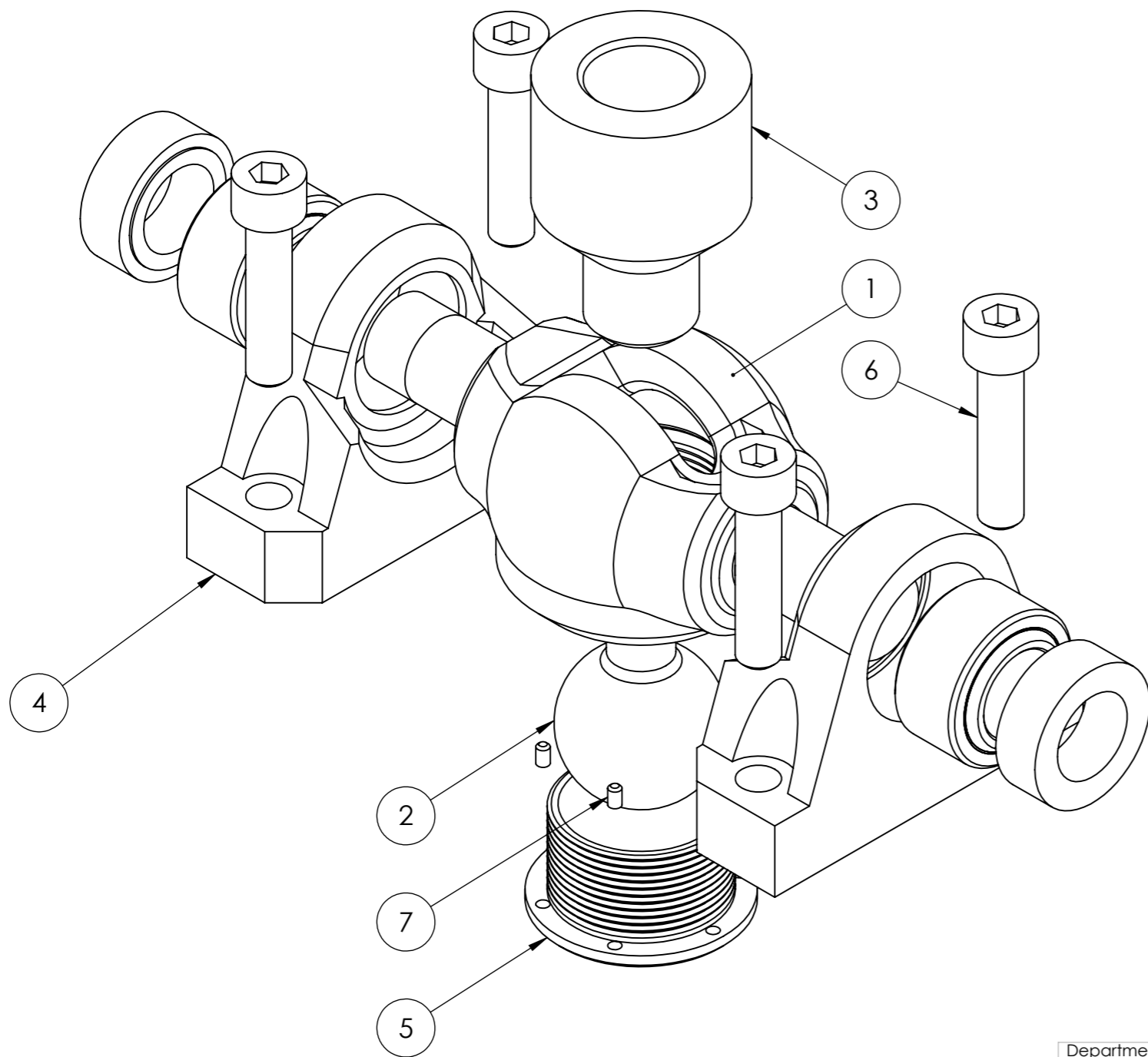
Cosmo Centre

Cosmo Centre PM-600 of Okuma is a machining centre intended to produce aluminium dies, see [72]. It has a cylindrical workspace of $\varnothing 800x400mm$ and is capable of 30 degrees tool rotation, but the workspace is then reduced to $\varnothing 380x340mm$ [72]. It is capable of a transverse rate of $100m/min$ ($1.7m/s$) in x and y and $80m/min$ ($1.3m/s$) in z and while cutting it has a feed rate of $40m/min$ $0.67m/s$.

Verne machine The VERNE machine is a 3 d.o.f PKM with a 2 d.o.f table [73]. It is a gantry-based delta configuration, which is known as the Triglide structure. The machine was built by Fatronik for IRCCyN [74].

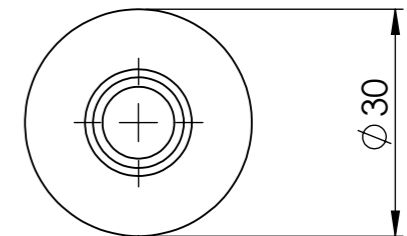
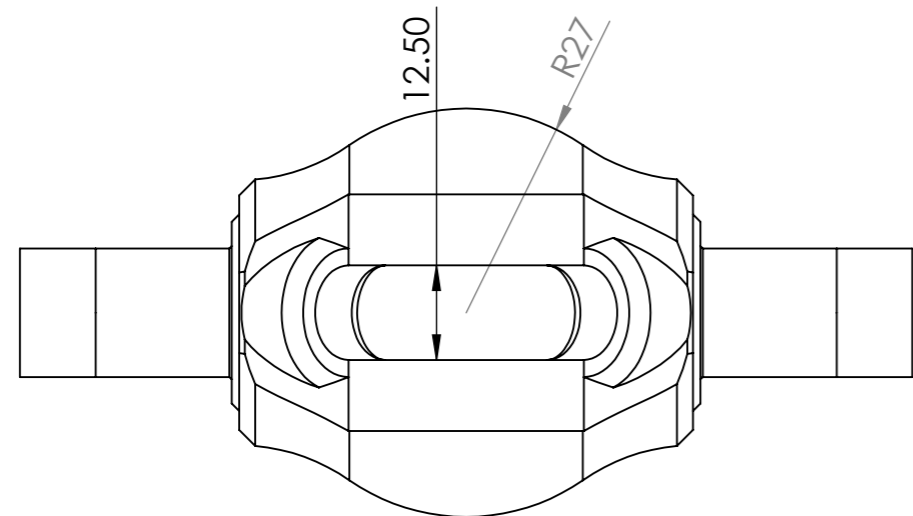
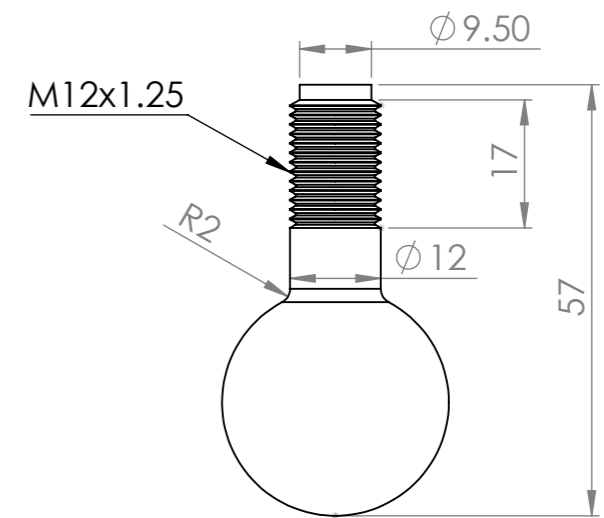
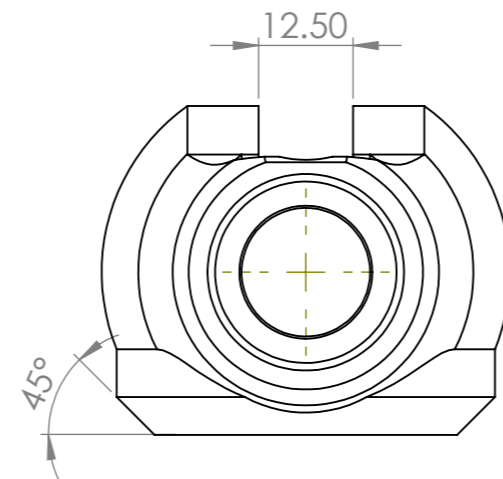
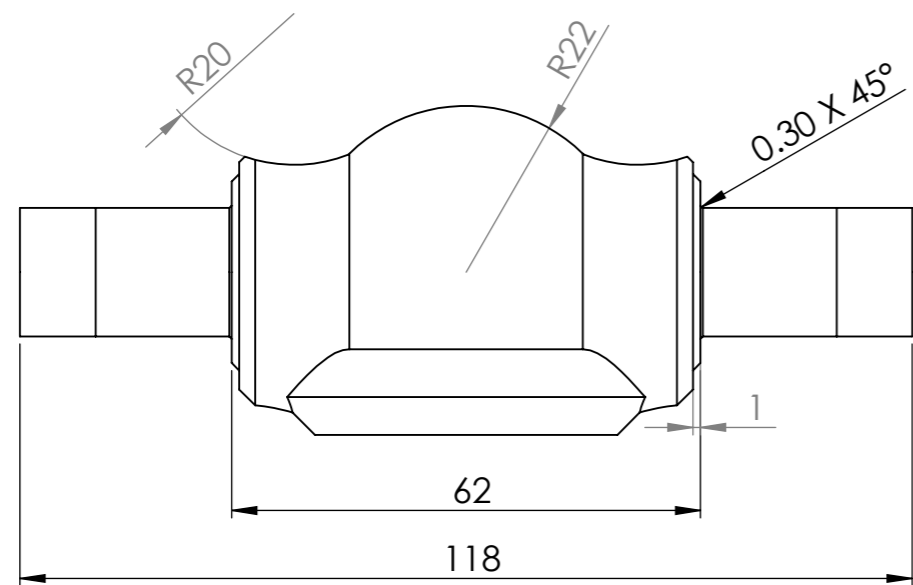
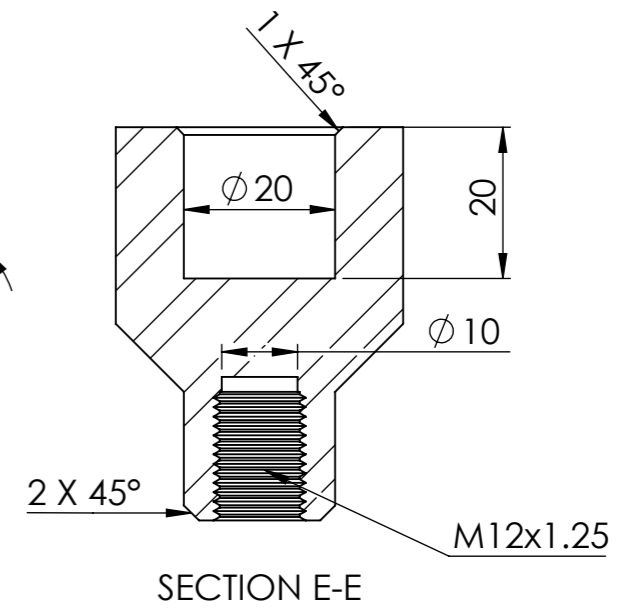
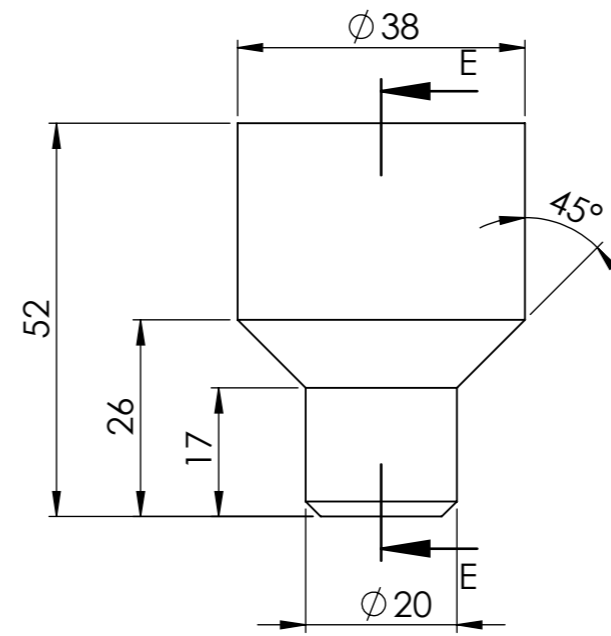
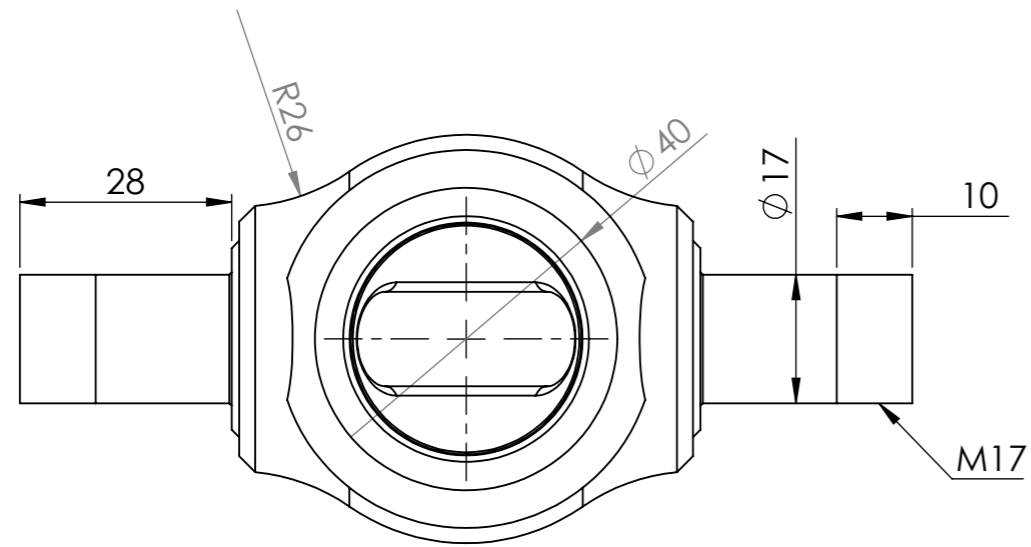
Ulyses Another PKM milling machine of Fatronik is the Ulyses, which is a 3 d.o.f milling machine designed for the production of dies and moulds. It has a workspace of $630x500x500$ mm, maximum transverse rate of $2m/s$ and maximum acceleration of $20m/s^2$.

C Ball Joint Dimensions

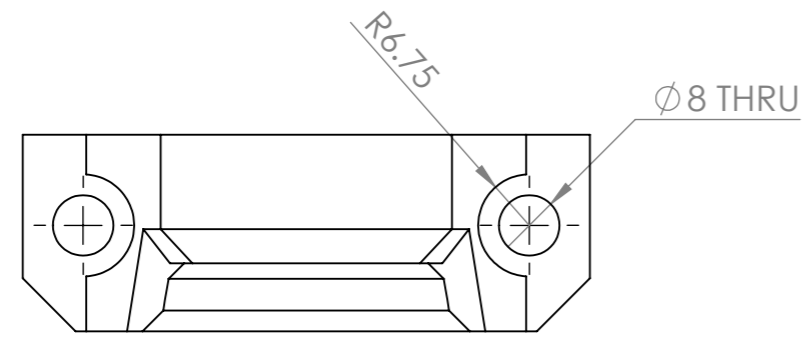
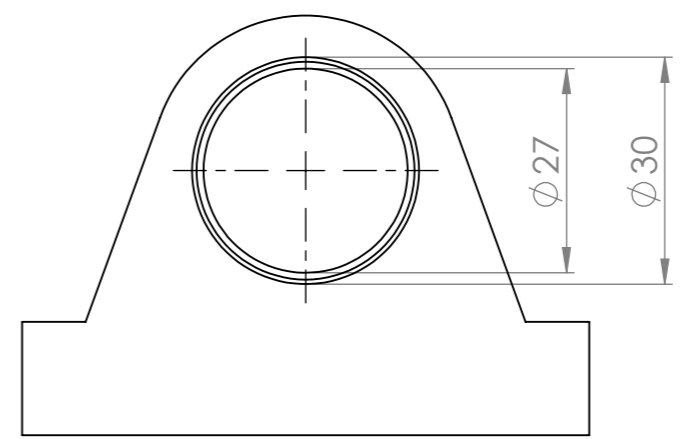
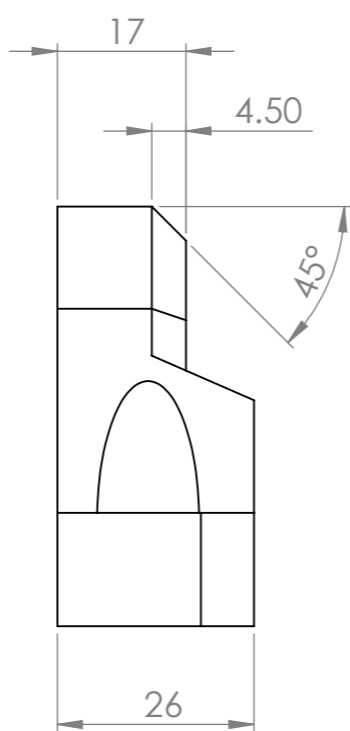
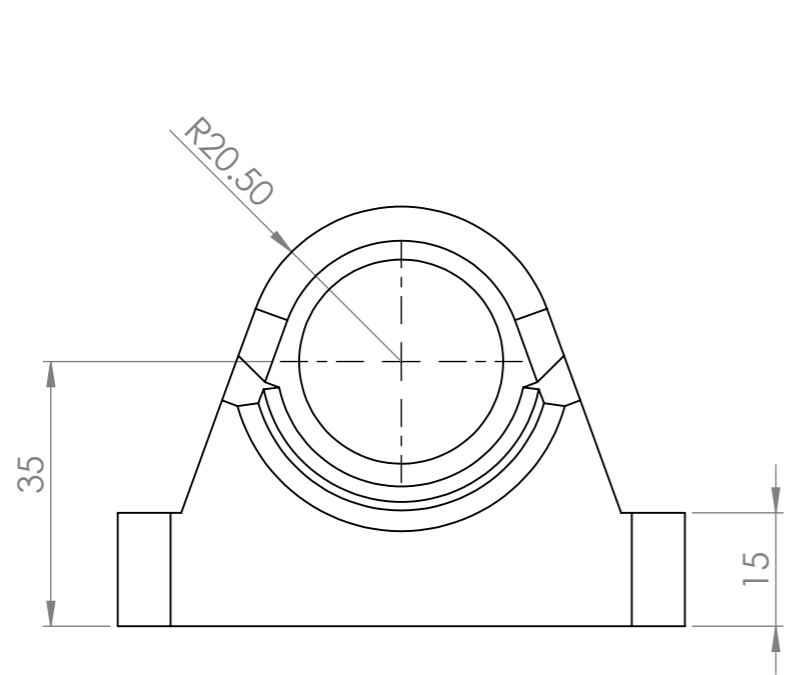
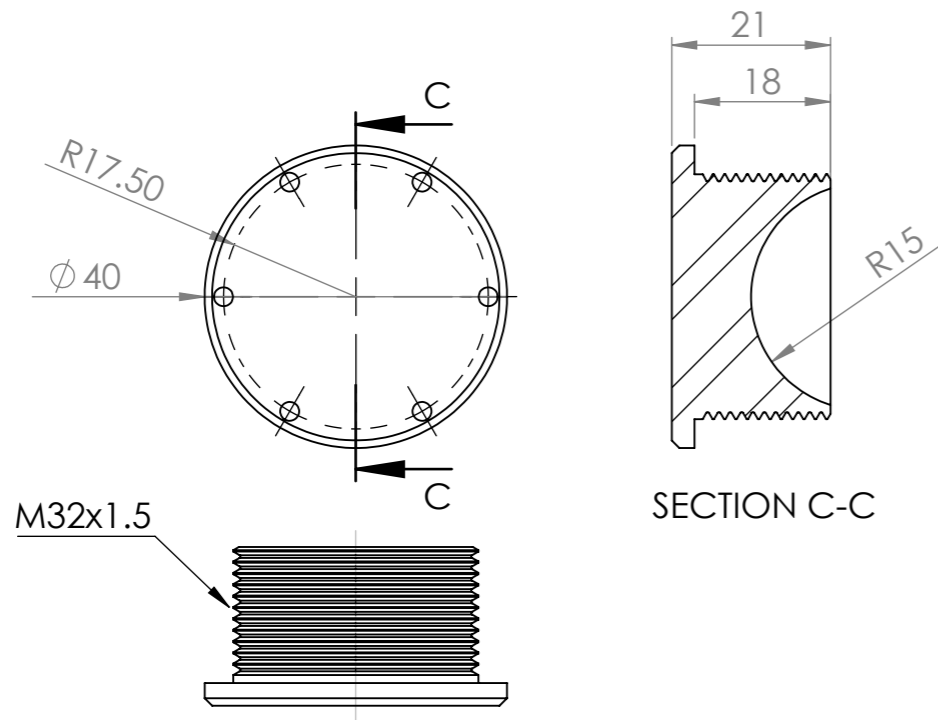


ITEM NO.	PART NUMBER	Material	Mass	QTY.
1	Joint Body	SS 416	591g	1
2	Ball	SS 416	132g	1
3	Link Adapter	SS 416	255g	1
4	Joint Bracket	SS 416	358g	2
5	Cap	SS 416	107g	1
6	M8x35-DIN912		21g	4
7	M2.5x4 - DIN913 Set screw		0.13g	6
8	Spherical Plain Bearing		62g	2
9	Bearing Lock Nut - M17		30g	2

Department Department Of Engineering - University Of Agder		Scale 1:1	
Author Jan Fredrik Røsjordet	Title Ball joint assembly	Date 25.05.2018	Rev. 1
		Lang EN	Sheet format A3
	Tolerance ISO 2768(m) - if not otherwise specified		Sheet 1/3
			Unit SI(mm)

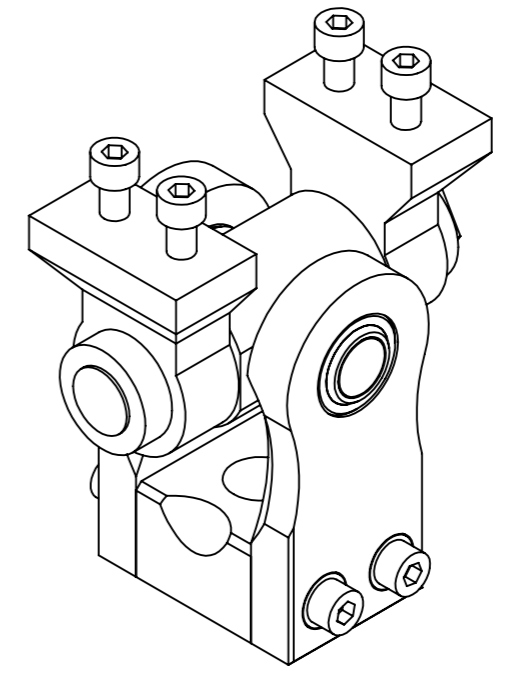
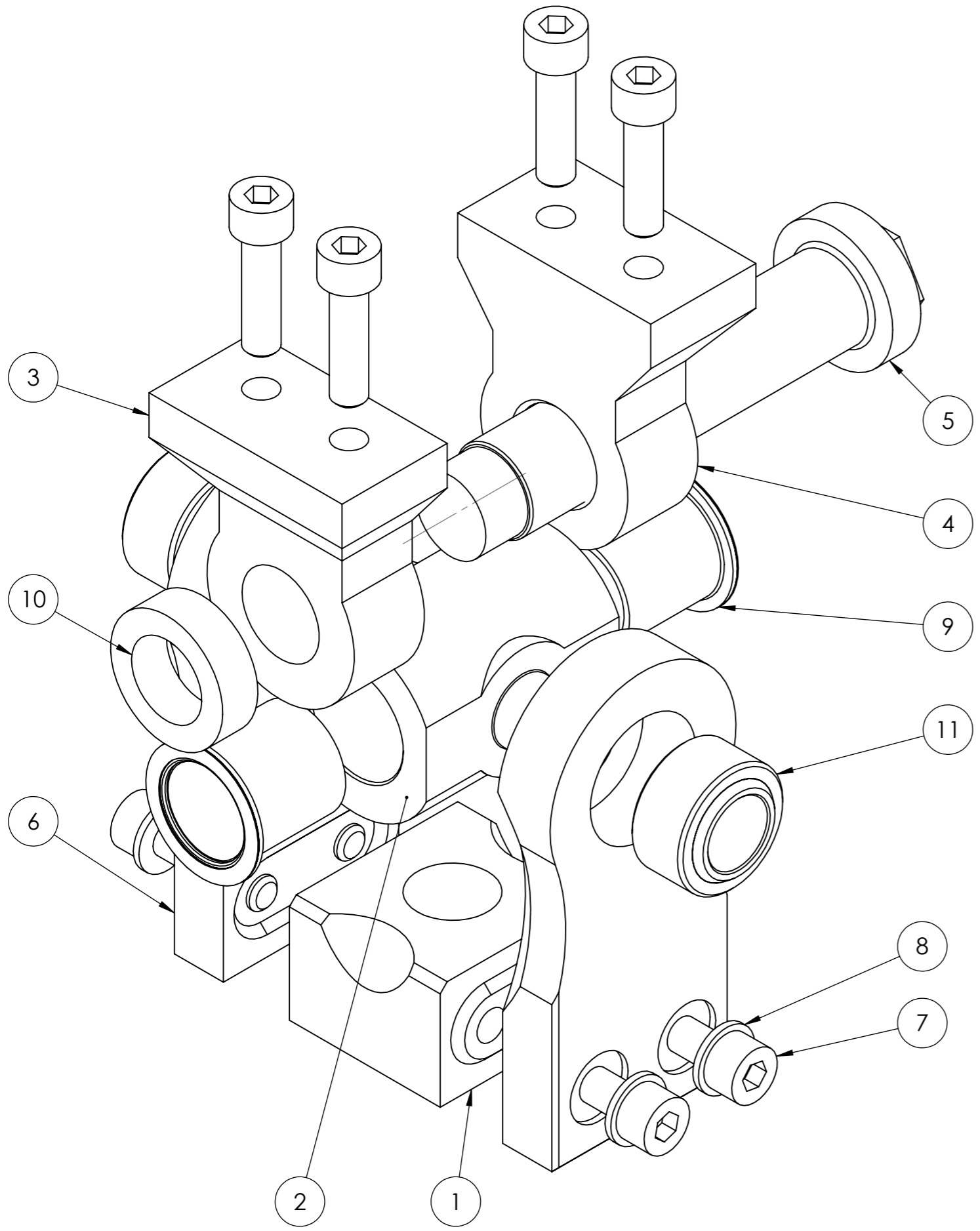


Department Department Of Engineering - University Of Agder		Date 25.05.2018		Scale 1:1
Author Jan Fredrik Røsjordet	Title Joint Body, ball and link adapter	Lang EN	Sheet format A3	Rev. 1
Tolerance ISO 2768(m) - if not otherwise specified				Unit SI(mm)



Department Department Of Engineering - University Of Agder		Date 25.05.2018		Scale 1:1
Author Jan Fredrik Røsjordet	Title Joint Bracket and Cap		Rev. 1	
	Lang EN	Sheet format A3	Sheet 3/3	
Tolerance ISO 2768(m) - if not otherwise specified				Unit SI(mm)

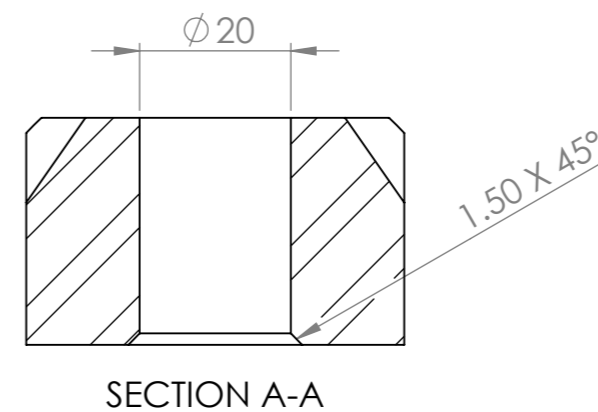
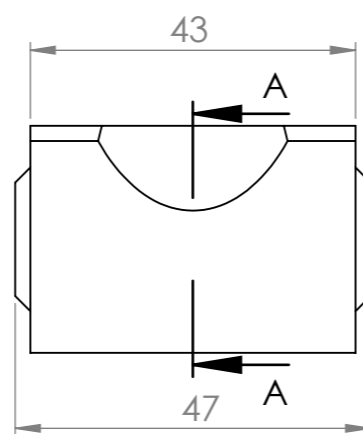
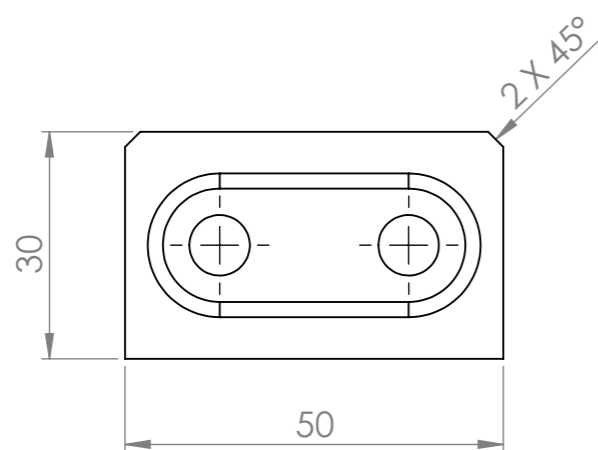
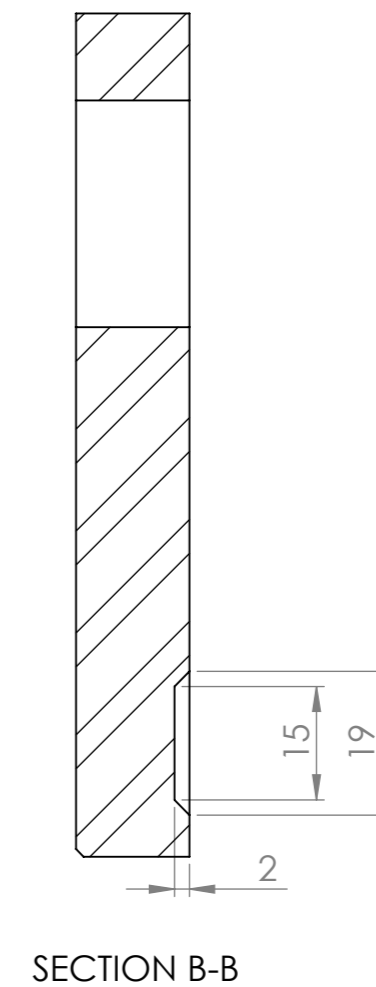
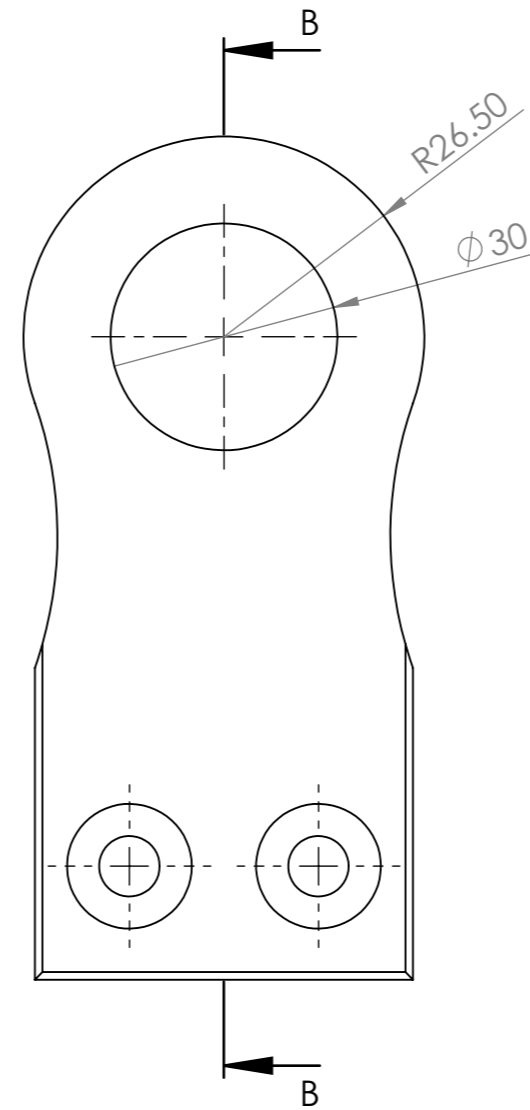
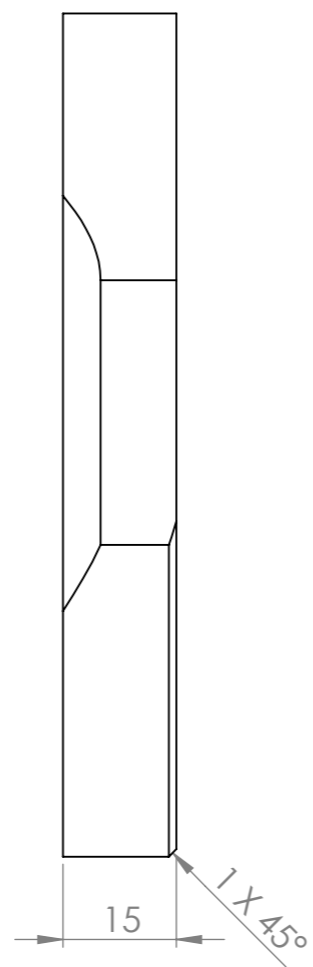
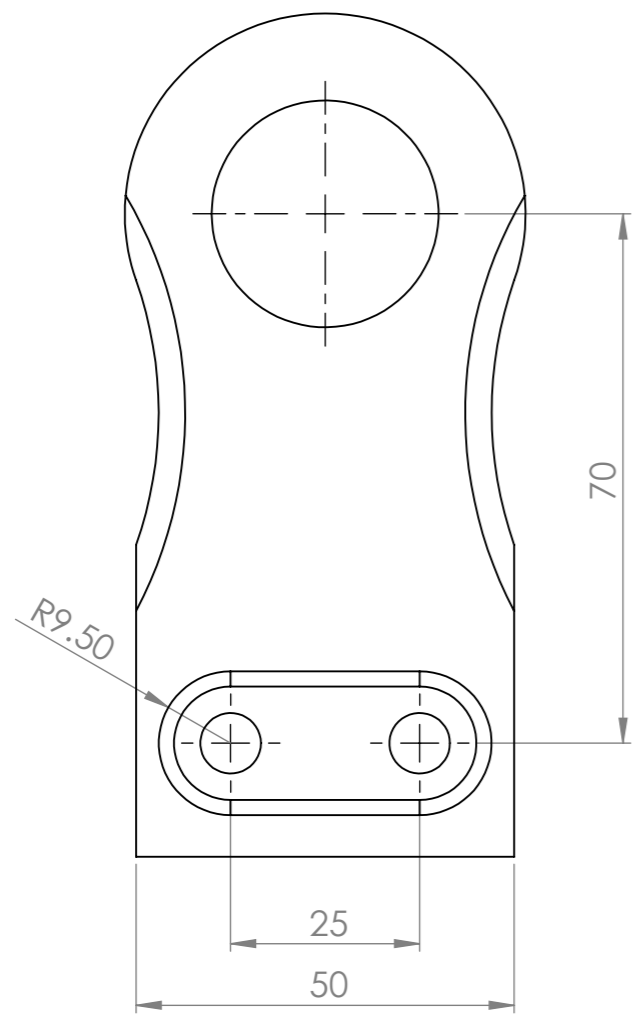
D Cardan Joint Dimensions



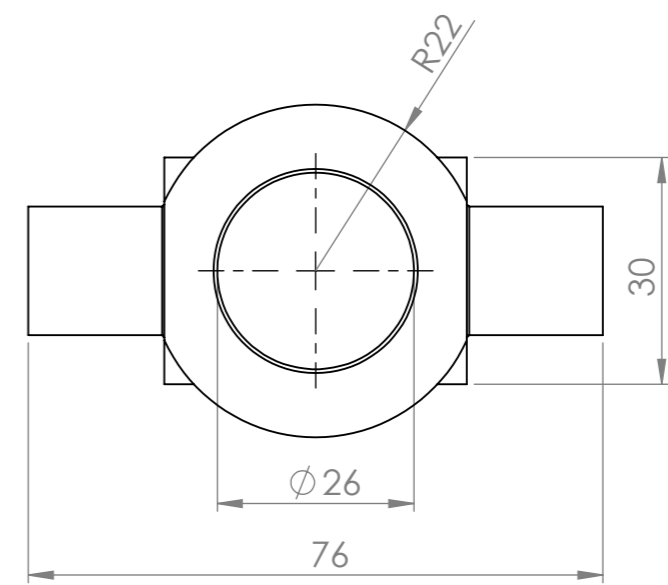
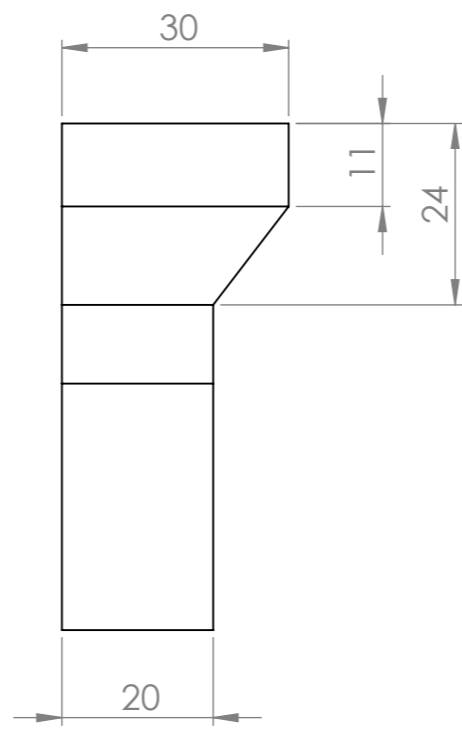
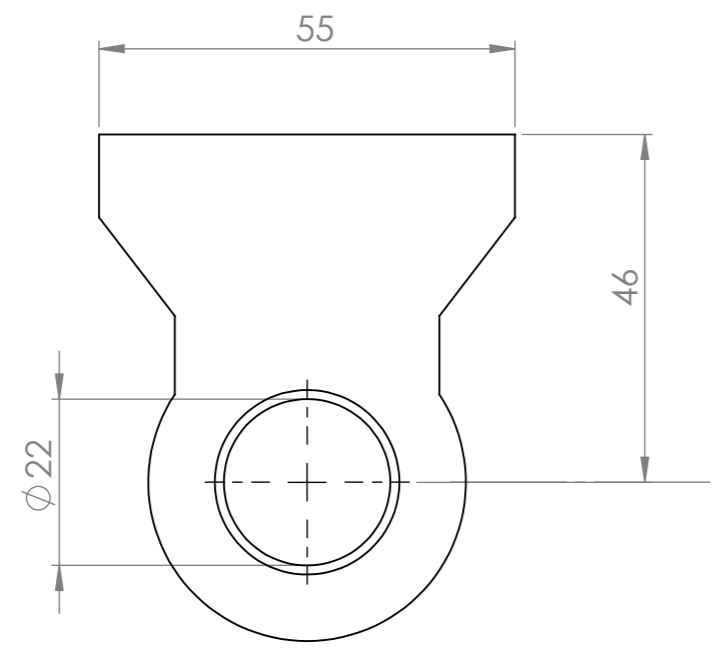
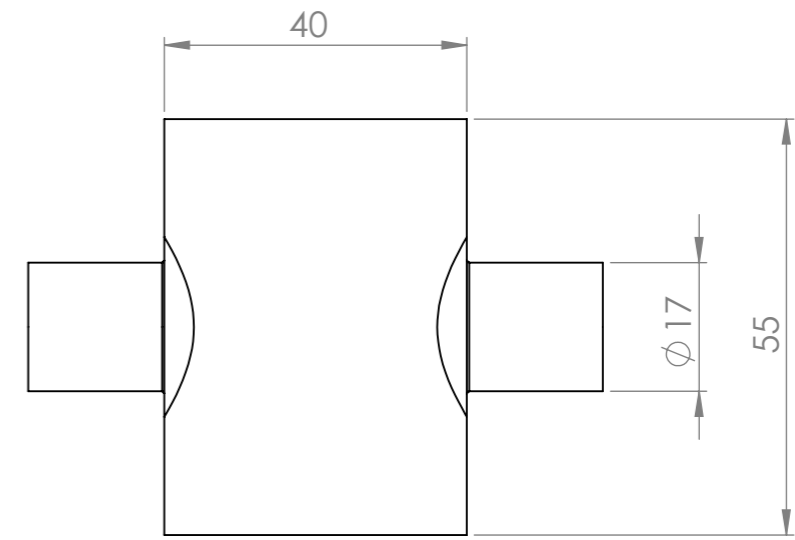
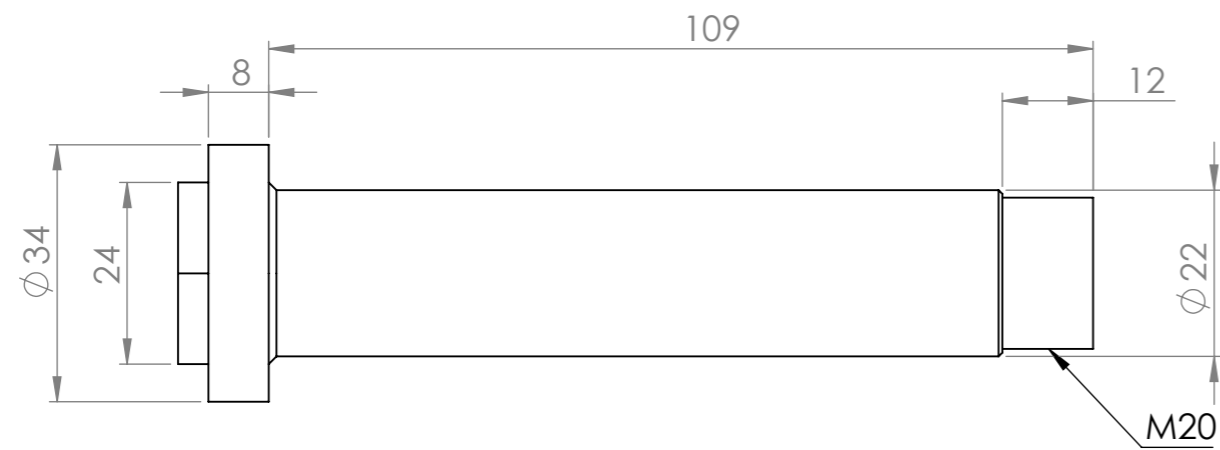
Scale 1:2

ITEM NO.	Description	Material	Mass	QTY.
1	Link Adapter	SS 416	410g	1
2	Hub	SS 416	471g	1
3	Mounting Bracket - L	SS 416	419g	1
4	Mounting Bracket - R	SS 416	419g	1
5	Shaft	SS 416	389g	1
6	Yoke Plate	SS 416	498g	2
7	M8x30-DIN912		20g	8
8	M8-Washer		1.9g	4
9	Flange Bearing (22x26x28)		35g	2
10	Shaft Lock Nut		38g	1
11	Spherical Bearing		62g	2

Department Department Of Engineering - University Of Agder		Scale 1:1	
Author Jan Fredrik Røsjordet	Title Cardan Joint Assembly	Date 25.05.2018	Rev. 1
		Lang EN	Sheet format A3
	Tolerance ISO 2768(m) - if not otherwise specified		Sheet 1/3
			Unit SI(mm)

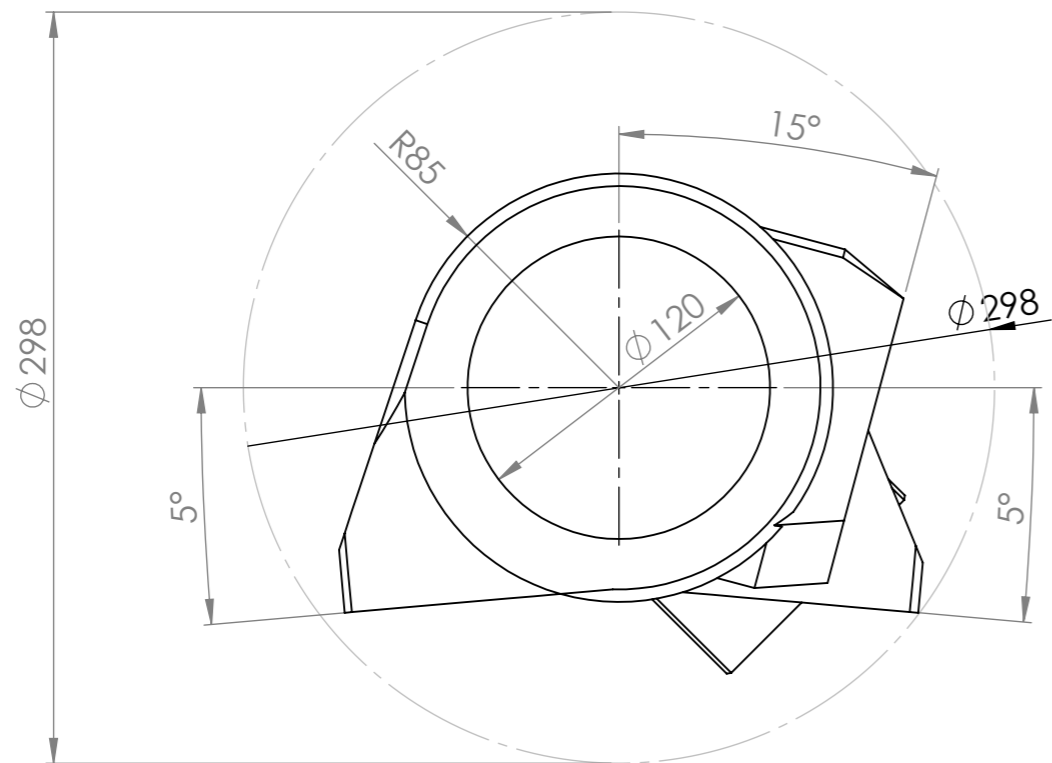
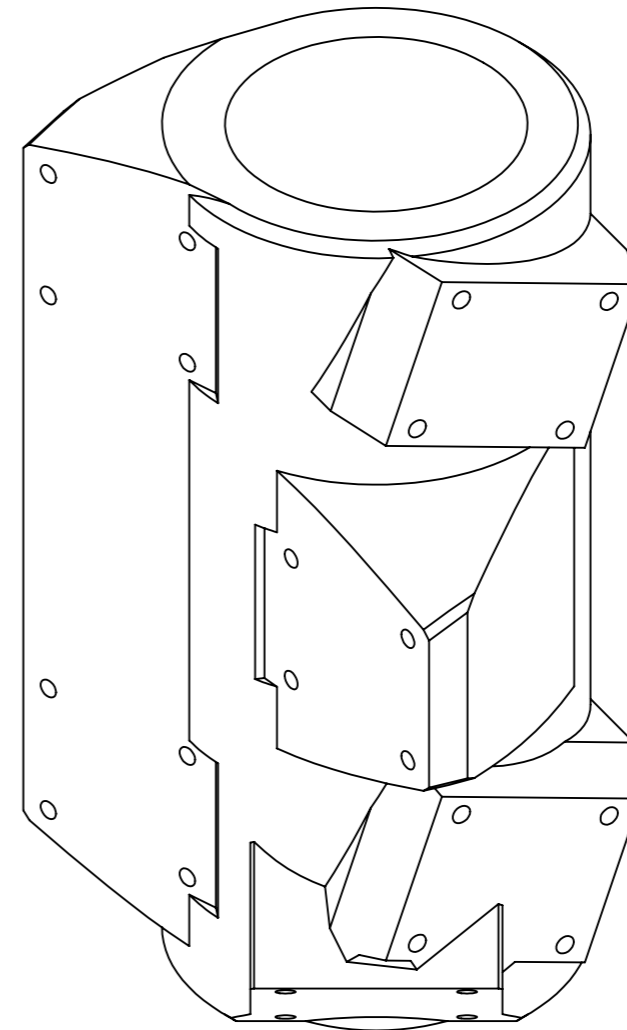
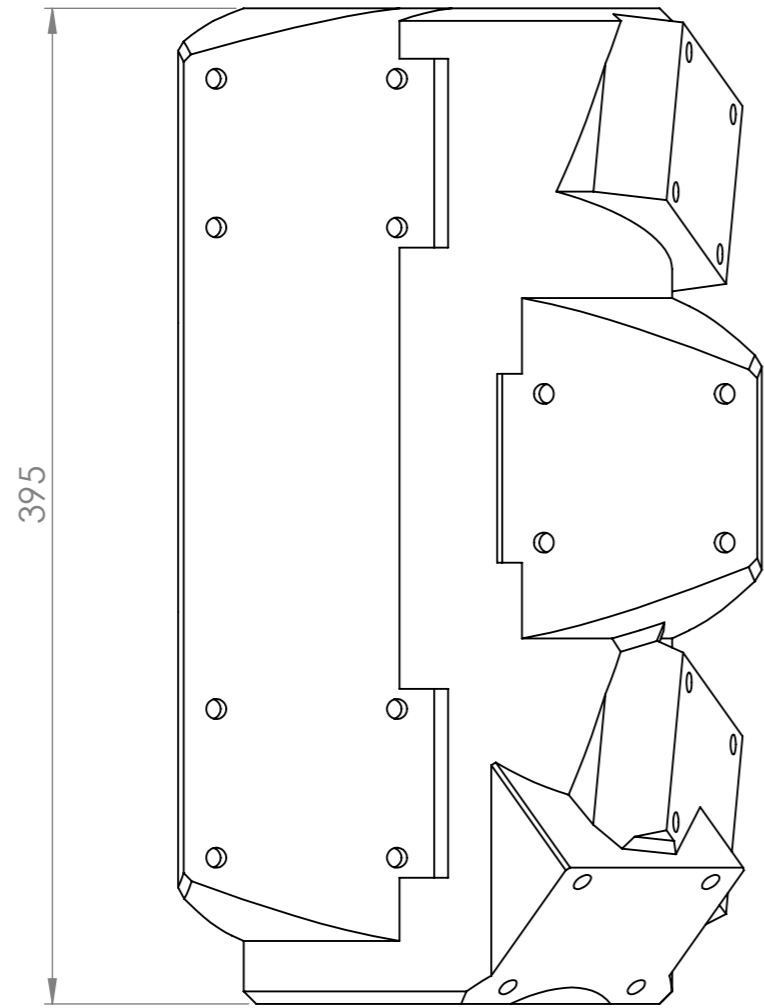


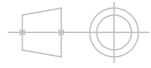
Department Department Of Engineering - University Of Agder				Scale 1:1
Author Jan Fredrik Røsjordet	Title Yoke and Link Adapter		Date 25.05.2018	Rev. 1
			Lang EN	Sheet format A3
	Tolerance ISO 2768(m) - if not otherwise specified			Sheet 2/3
				Unit SI(mm)



Department Department Of Engineering - University Of Agder				Scale 1:1
Author Jan Fredrik Røsjordet	Title Bracket, Shaft and Hub		Date 25.05.2018	Rev. 1
			Lang EN	Sheet format A3
Tolerance ISO 2768(m) - if not otherwise specified			Unit SI(mm)	

E Tool Platform Dimensions



Department Department Of Engineering - University Of Agder				Scale 1:3
Author Jan Fredrik Røsjordet	Title Tool platform		Date 25.05.2018	Rev. 1
			Lang EN	Sheet format A3
Tolerance ISO 2768(m) - if not otherwise specified			Unit SI(mm)	